SELF-HEALING STRATEGIES FOR LITHIUM-ION BATTERY ANODES

BY

SEN KANG

DISSERTATION

Submitted in partial fulfillment of the requirements
for the degree of Doctor of Philosophy in Materials Science and Engineering
in the Graduate College of the
University of Illinois at Urbana-Champaign, 2015

Urbana, Illinois

Doctoral Committee:

Professor Nancy R. Sottos, Chair and Director of Research
Professor Scott R. White
Professor Paul V. Braun
Professor Kristopher A. Kilian

ABSTRACT

Thermal-mechanical failure of microelectronic devices often involves in the loss of conductivity of the metal traces and vias, which shortens the lifetime and requires replacement of the entire unit. High-capacity Si composite electrodes in lithium-ion batteries also suffer from the damage of electrical interfaces (particle/binder interfaces) during battery operation, leading to rapid capacity loss. In this dissertation, autonomous restoration of electrical conductivity upon damage is demonstrated in composite battery anodes and a simple electrical circuit via two different approaches.

The first approach for conductivity restoration relies on the release of microencapsulated conductive particles to the fracture plane to reconstruct the damaged conductive pathways. In the second approach, dynamic ionic bonds are incorporated at the interface of polymer binder and Si nanoparticles in a composite battery electrode.

Robust microcapsules are prepared with carbon black suspensions high in solids loading (up to 0.2 g/mL) for electrical conductivity restoration. Octadecyl groups are covalently functionalized on oxidized carbon black surfaces by two different synthetic routes. Functionalization significantly increases particle hydrophobicity, and improves dispersability and suspension stability in hydrophobic solvents such as *o*-dichlorobenzene (*o*-DCB), enabling encapsulation by *in situ* emulsion polymerization. Upon rupture, microcapsules containing functionalized carbon black (FCB) suspensions exhibit significant particle release relative to microcapsules filled with unfunctionalized carbon black. Two types of core thickeners, epoxy resin or poly 3-hexylthiophene (P3HT), are used to enhance particle release from microcapsules.

Microcapsules containing FCB suspensions enable *ex-situ* conductivity restoration of damaged Si electrodes and an electric circuit. Rupturing of the microcapsules on the line crack of Si electrodes lead to the release of conductive FCB particles to the crack region and eventually full recovery (100 % restoration efficiency) of electrode conductivity. Similarly, partial conductivity restoration is achieved for a damaged electric circuit upon FCB release from microcapsules.

A protective polydopamine (PDA) coating is applied to the microcapsule surfaces to enhance the capsule stability in battery electrolytes and other harsh environments. The polymerization of dopamine monomers is initiated by the addition of an oxidant (i.e. ammonium persulfate) in an aqueous solution of neutral pH. The resulting PDA coating is a dense and uniform layer (ca. 50 nm thick). The PDA protective coating significantly increases the capsule stability at elevated temperature (180 ^{o}C) as well as in a variety of organic solvents and acidic/basic solutions that otherwise lead to deflation and loss of core content of uncoated microcapsules. Most importantly, the PDA coated microcapsules show significantly reduced core loss in battery electrolyte over 60 days as compared to uncoated microcapsules.

Intrinsic conductivity restoration relies on the reversible dissociation and formation of dynamic chemical bonds. Dynamic ionic bonds are incorporated at the interface of Si nanoparticles and polymer binders inside Si composite anodes. The presence of ionic bonds is confirmed by X-ray photoelectron and Raman spectroscopy. The dynamic ionic bonds effectively mitigate the large volume change of Si anodes during lithium intercalation. Si composite anodes with dynamic ionic bonding exhibit excellent cycling stability with a cycle life of 400 cycles and 80 % capacity retention at a current density of 2.1 mA/g.

ACKNOWLEDGMENTS

First of all, I would like to sincerely thank my research advisor, Prof. Nancy Sottos, for her guidance, time, and efforts in supporting my graduate study throughout the past six years. She has mentored me to be an independent scientist and taught me the value of enthusiasm, persistency, responsibility, and conscientiousness. All these elements I received from her are truly guiding me on my continuous pursuit of success in my life and career. I am also grateful to my co-advisor, Prof. Scott White, who has inspired and motivated me throughout my journey in graduate school. The big vision, courage, curiosity, and humor that he imparted to me will undoubtedly benefit my future. I would also like to thank Prof. Paul Braun and Prof. Kristopher Kilian for serving on my committee and for providing me valuable suggestions during my graduate studies.

I also want to thank the battery team of Autonomous Materials Systems (AMS) group, Dr. Ben Blaiszik, Dr. Susan Odom, Dr. Oya Okman, Dr. Marta Baginska, Elizabeth Jones, Stephen Pety, Taewook Lim, and Josh Kaitz. We went through a lot of hard times together. We built up our battery lab, learnt about battery technologies, exchanged research ideas, and supported each other's work. I would also like to thank everyone in Sottos/White research group and AMS group, especially Dr. Amanda Jones and Ke Yang. I appreciate the support from all of you.

I would not be where I am now without the understanding and love from my family. My husband, Chunjie Zhang, shared with me all the joys and tears in my graduate school life. Thank you for being my company and soul mate in the journey during the past eleven years. My parents always support my decisions and encourage me to take new challenges in my life. I want to express my sincere gratitude to them for all their love and sacrifices since I started college.

Finally I would like to acknowledge the funding from the Center for Electrochemical Energy Science, an Energy Frontier Research Center funded by the U.S. Department of Energy. I also want to thank the staff at Material Research Laboratories and Beckman Institute at the University of Illinois for their assistance with the instruments, especially Dr. Rick Haasch, Dr. Tao Shang, and Scott Robinson.

TABLE OF CONTENTS

CHAPTER 1: INTRODUCTION 1
1.1 Self-Healing Polymeric Materials 1
1.2 Autonomous Restoration of Electrical Conductivity 5
1.3 Silicon Composite Anodes in Lithium-Ion Batteries 8
1.4 Overview of Thesis Research 14
1.5 References 15
CHAPTER 2: ENCAPSULATION OF CARBON BLACK SUSPENSIONS 20
2.1 Introduction 20
2.2 Experimental 21
2.2.1 Materials 21
2.2.2 Functionalization and Characterization of Carbon Black Particles 21
2.2.3 Synthesis of P3HT 23
2.2.4 Preparation and Characterization of Carbon Black Suspension Filled Microcapsules 23
2.3 Results and Discussion 25
2.3.1 Dispersion and Suspension of Carbon Black 25
2.3.2 Encapsulation of Carbon Black 30
2.3.3 Release of Carbon Black upon Capsule Rupture 36
2.4 Conclusions 38
2.5 References 39
CHAPTER 3: RESTORATION OF ELECTRICAL CONDUCTIVITY AFTER MECHANICAL DAMAGE 41
3.1 Introduction 41
3.2 Experimental 42
3.2.1 Materials 42
3.2.2 Conductivity Restoration of Fractured Si Anodes 42
3.2.3 Conductivity Restoration of Fractured Electric Circuit 43
3.3 Results and Discussion 44
3.3.1 Si anode Conductivity Restoration 44
3.3.2 Conductivity Restoration of Electric Circuit 48
3.4 Conclusions 50
3.5 References 51

CHAPTER 4: MICROCAPSULE STABILITY IN BATTERY ENVIRONMENT 52
4.1 Introduction 52
4.2 Experimental 53
4.2.1 Materials 53
4.2.2 Preparation of Microcapsules 54
4.2.3 PDA Coating of Microcapsules 54
4.2.4 Characterization of Microcapsules 55
4.3 Results and Discussion 56
4.3.1 PDA Coating on Microcapsules 56
4.3.2 Thermal Stability of Microcapsules 60
4.3.3 Solvent Stability of Microcapsules 61
4.4 Conclusions 64
4.5 References 66
CHAPTER 5: Si COMPOSITE Li-ION BATTERY ANODES WITH DYNAMIC IONIC BONDING 68
5.1 Introduction 68
5.2 Experimental 70
5.2.1 Materials 70
5.2.2 Surface Functionalization of Si Particles and Quantification of Amine Functionalities 70
5.2.3 Preparation of Si Anodes and Structural Characterization of Ionic Bonds 71
5.2.4 Electrochemical Characterization of Si Anodes 72
5.2.5 Characterization of Si Anodes 72
5.3 Results and Discussion 72
5.3.1 Surface Characterization of Si Nanoparticles and Composite Anodes 72
5.3.2 Cycling Performance of Si Composite Anodes 76
5.3.3 Structural Change of Si Composite Anodes 82
5.4 Conclusions 85
5.5 References 86
CHAPTER 6: SUMMARY AND FUTURE WORK 88
6.1 Summary 88
6.2 Future Work 90
6.2.1 In-situ Self-healing Battery Electrodes using FCB Microcapsules 90

6.2.2 Self-healing Battery Electrodes Based on Dynamic Chemical Bonding 91
6.3 References 98

CHAPTER 1

INTRODUCTION

1.1 Self-Healing Polymeric Materials

In nature, biological systems have the ability to heal wounds via sophisticated and autonomic processes. The biological wound healing has inspired and driven the recent advancements in self-healing polymeric materials with the capability of restoring their properties upon damage without external intervention, increasing the reliability and prolonging the lifetime of the materials. In polymeric materials, the self-healing function is realized by three different approaches: capsule based, vascular, and intrinsic methods, as illustrated in **Figure 1.1**.[1, 2]

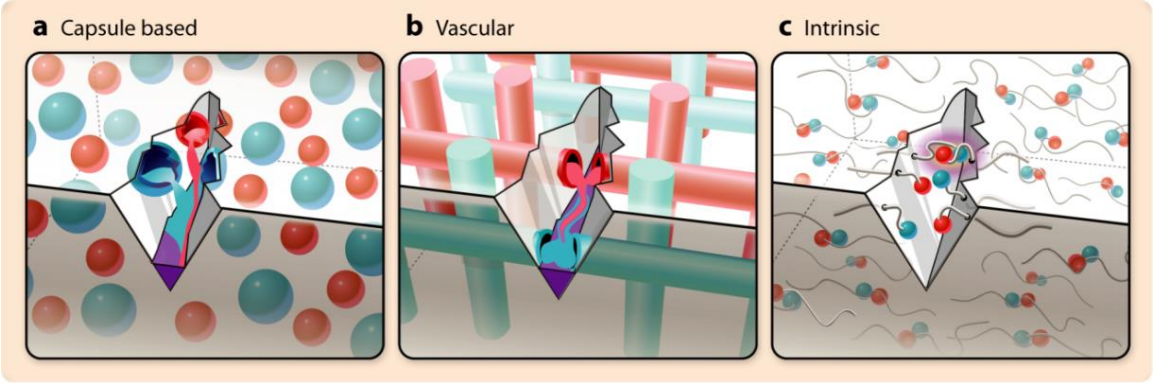


Figure 1.1. Approaches for self-healing of polymeric materials including (a) capsule-based, (b) vascular, and (c) intrinsic healing methods.

In capsule-based self-healing materials, liquid healing agents are sequestered in discrete capsules distributed throughout a polymer matrix. When damage occurs in the matrix, the healing agent is released from the ruptured capsules to the damage region facilitated by capillary force and subsequently undergoes spontaneous polymerization to rebond the interface. A variety of healing chemistries have been investigated. The first example is the ring opening metathesis polymerization (ROMP) of endo-dicyclopentadiene (DCPD) via Grubbs' catalyst.[3, 4] The liquid

DCPD is encapsulated in poly (urea-formaldehyde) shell wall and the Grubbs' catalyst particles are uniformly dispersed in the polymer matrix. Upon cracking, Grubbs' catalyst catalyzes the polymerization of released DCPD from capsules. Alternate diene monomers and catalyst (i.e. tungsten hexachloride, WCl_6) have also been applied in self-healing.[5, 6] Another type of healing chemistry is the polymerization of poly (dimethyl siloxane) (PDMS) oligomers in the presence of catalysts and initiators.[7-9] The liquid oligomers and liquid catalysts are encapsulated separately and embedded into the polymer matrix. Upon rupture, the two components react to form PDMS in the fracture plane. This chemistry is suitable for the healing of elastomeric materials. Solvent mediated polymerization of latent functionalities in the matrix is the third type of healing chemistry.[10-12] In this approach, microcapsules containing both solvent and epoxide are incorporated into under-cured epoxy matrix. Upon rupture, released solvent swells the crack plane and liberates the residual amine functionality into the matrix, which then reacts with the released epoxide to form cross-linked epoxy film. The fourth example is the polymerization of epoxides with epoxy hardeners.[13-16] The healing relies completely on the polymerization of the two encapsulated components instead of latent amine functionality in the epoxy matrix, allowing the self-healing in fully cured epoxy system.

Instead of discrete compartmentalization of healing agent in capsules, the vascular healing approach relies on continuous microvascular network embedded in a polymer matrix with the healing agents stored inside the network. Damage of the matrix ruptures the micro-channels and releases the healing agents, which subsequently undergo polymerization.[17-22] Different from the singular healing event in capsule-based healing approach due to the depletion of capsule core, the vascular system can achieve multiple healing cycles by continuous delivery of healing agents to the crack region from the channel network and external reservoir of healing agents.

In contrast to the capsule and vascular approaches where the liquid healing agents are compartmentalized inside the polymer matrix, the intrinsic healing approach utilizes dynamic chemical bonds that are incorporated inside the polymer matrix at molecular level. The reversible dissociation and reformation of the dynamic bonds impart the self-healing capabilities. Dynamic bonds can be covalent or non-covalent in nature. The reversibility of dynamic bonding typically requires external stimuli (such as temperature, catalyst, and light) or high chain mobility of the polymer, depending on the specific environment.[23]

One typical dynamic covalent bond exists in a Diels-Alder (DA) adduct which undergoes reversible reaction at elevated temperatures as illustrated in **Figure 1.2**a. Wudl and coworkers took advantage of the dynamic nature of this reaction and prepared polymer resin containing DA adducts with mechanical properties comparable to epoxy.[24] The fracture load of a thermally healed specimen (at 120 ^{o}C for 2 h) was 41 % of that of the undamaged specimen due to the reformation of DA adducts across the fracture surface. In later research, the adduct of fulvene (diene) and cyanoolefin (alkene) yielded materials with room temperature healing ability.[25] Thermally reversible alkoxyamine (C-ON bond, **Figure 1.2**b) is another type of dynamic covalent bond. Epoxy containing alkoxyamine was developed to show the restoration of impact strength with multiple healing cycles in argon at 90 ^{o}C. [26] Cheng et al. recently reported self-healing polyurea and poly(urethane-urea) containing hindered urea bonds (urea with bulky substituents attached to the nitrogen bonds) with reversibility at low temperatures (**Figure 1.2**c). [27]

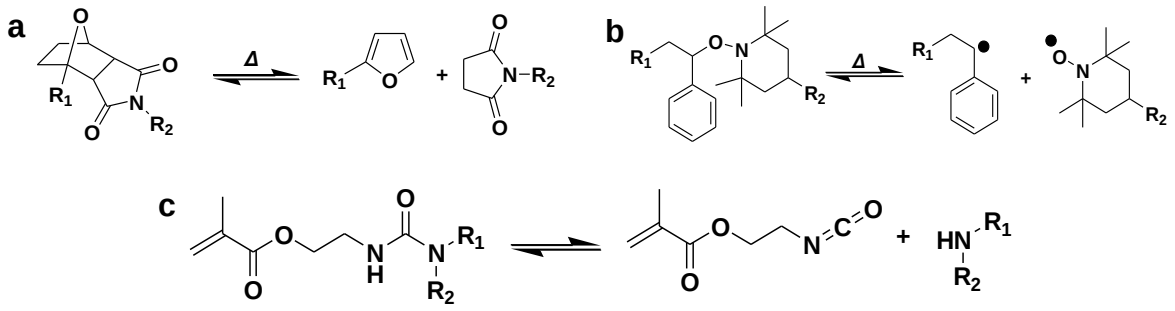


Figure 1.2. Thermally triggered reversible reaction of (a) DA adducts and (b) alkoxyamine. (c) Equilibrium between isocyanate, bulky amine and the corresponding urea.

A broader range of non-covalent dynamic bonds, such as hydrogen bond, π-π stacking, metal-liquid coordination, ionic bond, and other types of specific interactions, also impart self-healing capabilities in polymers.[28-33] Leibler and colleagues reported a self-healing synthetic rubber built upon small molecules with hydrogen bonding functionalities.[28, 29] The hydrogen bonds associated the small molecules to form chains and crosslinks (**Figure 1.3**a). When the broken ends of the rubber were brought into contact, hydrogen bonds were reformed at the crack plane, enabling the restoration of mechanical properties at room temperature. Burattini et al. fabricated a polymer blend film comprised of chain-folding polyimide and pyrene end-capped polyurethane.[30, 31] The aromatic π-π stacking between the electron deficient imide and electron rich pyrene was thermally reversible (**Figure 1.3**b), allowing the healing of a damaged film (with a 75 μm wide cut) at an elevated temperature (80 ^{o}C).

Ionic bonding has also been investigated for self-healing polymers. Andreeva et al. developed polyelectrolyte multilayers comprised of polystyrene sulfonate (polyanion) and polyethyleneimine (polycation) for anticorrosion coatings.[32] The polymer chain mobility in water facilitated the reformation of ionic bond at the scratch region and healed the film. Hydrogels containing polyacrylic acid (polyanion) and ferric ion (cation) were also prepared with self-healing capability.[33]

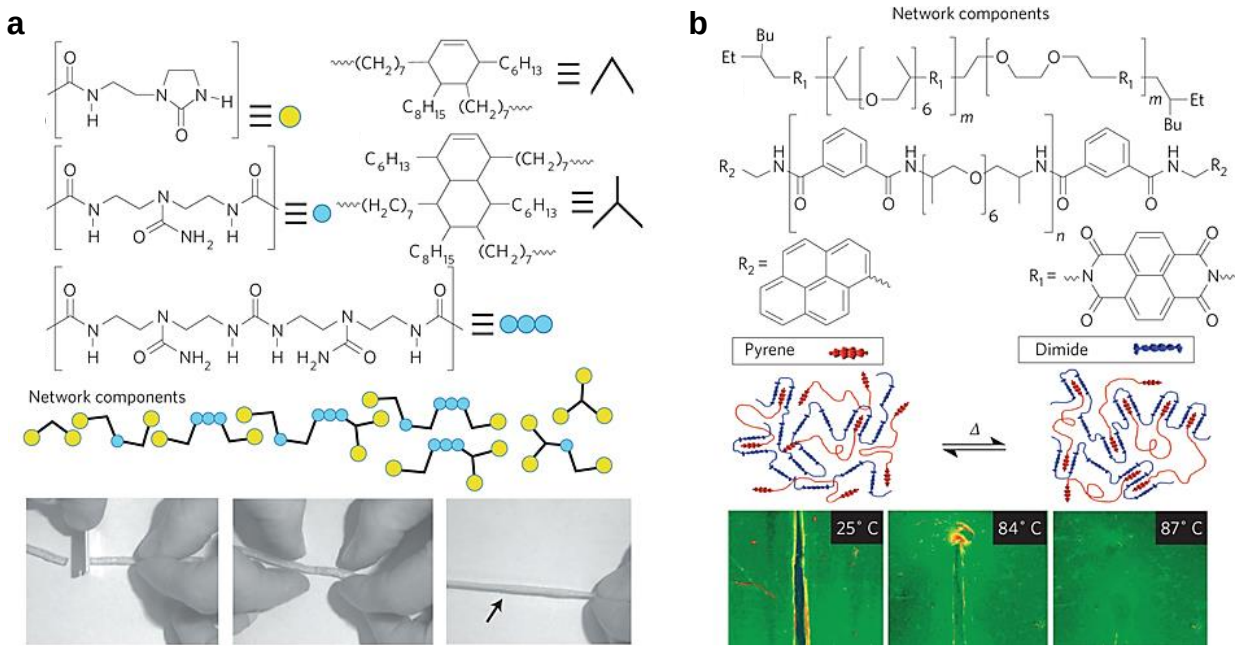


Figure 1.3. (a) Hydrogen bonding network of a self-healing rubber. (b) π-π stacking network of a self-healing polymer film and thermally reversible interactions of diimide and pyrene.[28-31]

1.2 Autonomous Restoration of Electrical Conductivity

The self-healing concept is not limited to the repair of mechanical damage; the restoration of other properties such as the electrical conductivity can also be realized using the three approaches described in **Figure 1.1**.[34, 35]

Damage triggered release of microencapsulated conductive core materials has enabled the autonomous restoration of electrical conductivity in a broken circuit.[36, 37] The encapsulation of several different types of conductive core materials has been reported in literature.[37-44] Three restoration schemes are shown schematically in **Figure 1.4**. In the first scheme, two reactive liquid components are encapsulated and embedded into the matrix. Upon damage of the matrix and rupture of the dual microcapsules, conductive polymer or crystal is formed by the reactive liquids at the fracture plane. Odom et al. reported the formation of conductive transfer salt, TTF-TCNQ (tetrathiafulvalene-tetracyanoquinodimethane), after the release of the encapsulated reactive TTF

and TCNQ solutions. Partial conductivity restoration of a broken gold circuit was observed due to the conductive transfer salt formation. [39] The second scheme relies on the encapsulation and release of liquid metal alloys. Blaiszik et al. prepared conductive Ga-In alloy filled microcapsules and demonstrated full recovery of conductivity in a mechanically damaged circuit within one millisecond after the damage occurred.[36, 44] In the third scheme, conductive particle suspensions are encapsulated. Microcapsules containing carbon nanotube and graphene suspensions have been reported to restore electrical conductivity upon the release of the conductive payload.[37, 38]

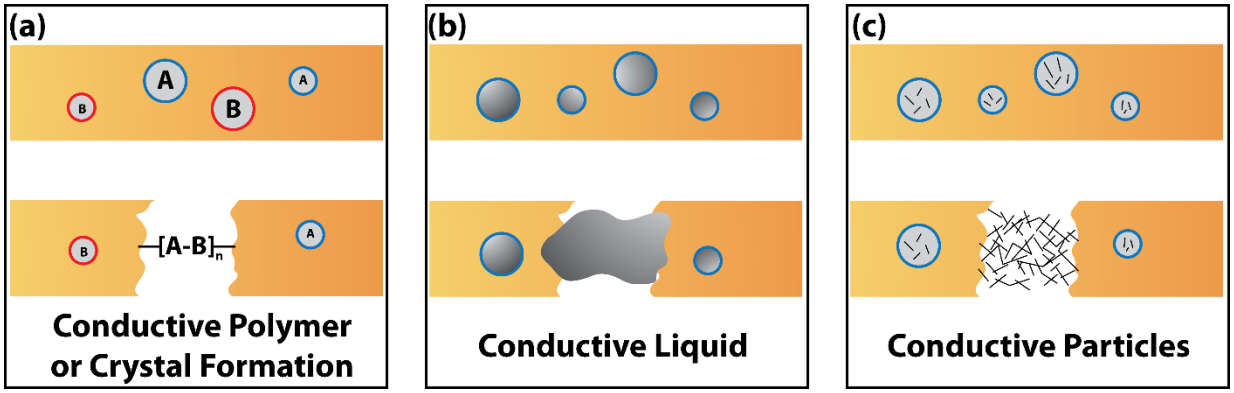


Figure 1.4. Microcapsule based conductivity restoration of damaged electric circuit or electrode. The types of microencapsulated core include (a) two-part reactive liquid components, (b) liquid metal, and (c) conductive particle suspensions.

Microvascular based conductivity restoration was demonstrated by reconfigurable wires consisting of self-healing polymer shell and liquid Ga-In metal core.[45] As shown in **Figure 1.5**, the cut pieces from one straight wire were re-assembled in multiple ways with different shapes and dimensions. The polymer shell self-healed in minutes via hydrogen bonding and the conductivity was restored due to the formation of Ga-In liquid metal pathway among the cut pieces.

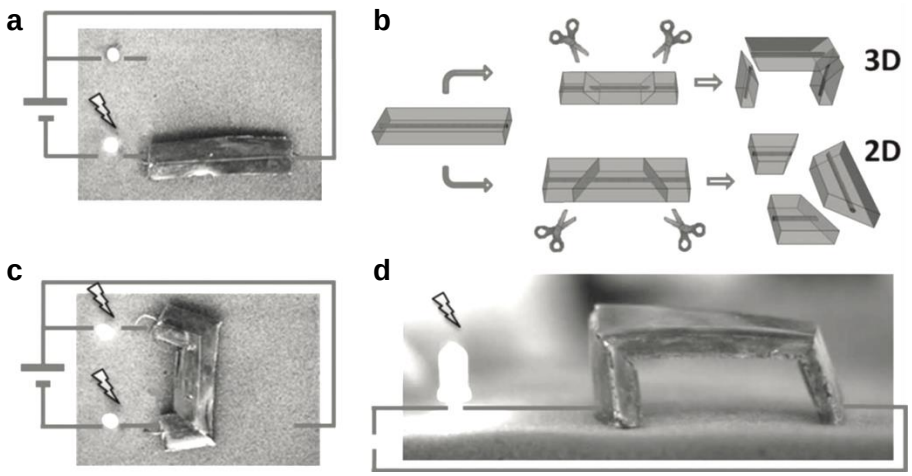


Figure 1.5. (a) An electric circuit connected with straight reconfigurable wire. The top LED was off because it was not electrically connected. (b) Ways of cutting and reassembling the straight wire to create different dimensions and shapes of the wire. (c) The electric circuit with reconfigured 2D wire, the top LEF was on due to the formation of Ga-In electric pathway. (d) Side view of the circuit with reconfigured 3D wire.[45]

Bielawski and co-workers developed a class of conductive organometallic polymers comprising *N*-heterocyclic carbine and transition metals with self-healing properties.[46] The dynamic equilibrium of metal and carbine is shown in **Figure 1.6**. These polymers had electrical conductivities on the order of 10^{-3} S/cm. After a crack (ca. 15 μm in width) was introduced by scoring, the thin polymer film healed after exposure in DMSO vapor at 150 ^{o}C for 2 h.

In addition to intrinsic conductive polymers, composites comprising electrically insulating dynamic polymers and conductive particles can also undergo autonomous conductivity restoration. Li et al. reported a conductive film consisting of polyelectrolyte multilayers (PEM) and surface deposited silver nanowires.[47] The film was able to self-heal a scored crack (ca. 30 μm in width) after exposure to water. The swelling of PEM and reformation of ionic bonds across the fracture surfaces resulted in the healing of the crack and restoration of conductivity. Bao et al. developed a room temperature self-healing conductive composite for electronic skin applications.[48] The low glass transition temperature (lower than room temperature) and the reversible hydrogen bonding

network enabled autonomous healing of the polymer host (**Figure 1.7**). Ni microparticle filler imparted the conductivity (40 S/cm for undamaged composite). The healing event was fast (within 15 s) and efficient (90 % of initial conductance) over multiple healing cycles.

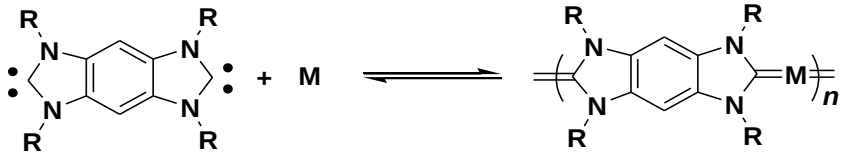


Figure 1.6. The dynamic equilibrium of the monomer species (carbine and metal) and organometallic polymer controlled by external stimuli.

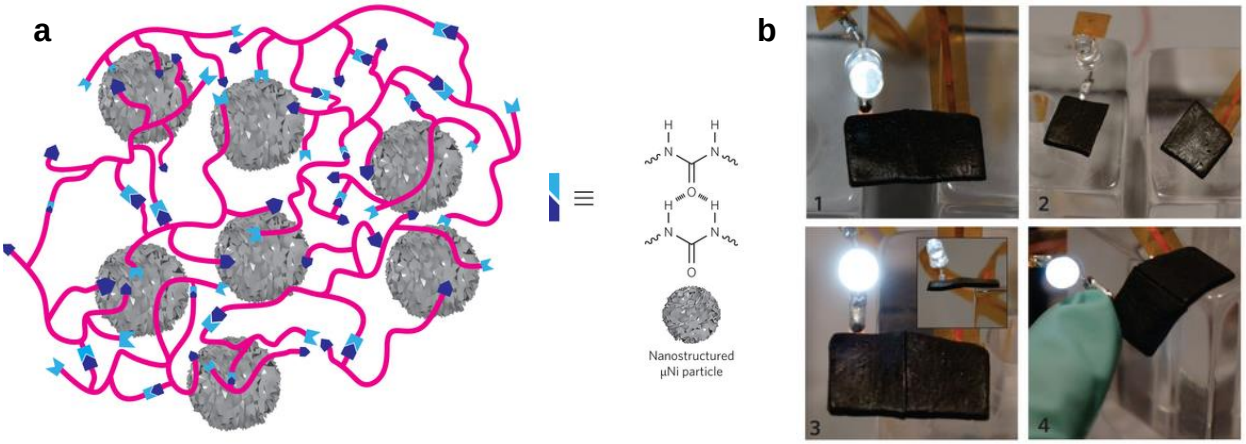


Figure 1.7. (a) Proposed interactions of polymer chains with Ni microparticles. The light and dark blue blocks shows the hydrogen bonding sites in the polymer chains. (b) Healing of the conductive composite with LED in series. 1. Undamaged composite. 2. Completely damaged composite. 3. Healed composite with restored conductivity. 4. Healed composite with restored mechanical integrity demonstrated by bending.[48]

1.3 Silicon Composite Anodes in Lithium-Ion Batteries

Lithium-ion batteries (LIB) have been widely used in portable electronic devices with high energy and power density as well as high operating voltages, and more recently in electric vehicles (EV) and hybrid electric vehicles (HEV). As shown schematically in **Figure 1.8**[49], a typical LIB consists of a positive electrode (cathode, e.g. $LiCoO_2$), a negative electrode (anode, e.g. graphite), and non-aqueous electrolyte which contains lithium salt (e.g. $LiPF_6$) and a mixture of organic

solvents (e.g. ethylene carbonate/dimethyl carbonate). Graphite and other types of carbonaceous materials are widely used as commercial anode materials in LIB with a specific gravemetric capacity of 372 mAh/g. Future EV/HEV applications will require higher specific capacities, motivating the development of new materials for anodes. Silicon is an attractive candidate because of its high gravimetric capacity (4200 mAh/g) and volumetric capacity (9786 mAh/cm^3)[50] , yet commercial application of Si anode materials has been hindered by the rapid capacity failure during cycling. **Figure 1.9** shows a representative voltage-capacity profile of a micro-Si (10 μm particles) composite anode. The first cycle charge capacity was ca. 3300 mAh/g, close to the theoretical capacity of Si. The first discharge capacity, however, decreased to ca. 1200 mAh/g. After 10 cycles, the capacity dropped to less than 500 mAh/g and continued to decrease with increasing cycle numbers.[51] Capacity fade is attributed to the enormous (ca. 400 %) volume increase at the completion of charging (lithiation). During discharge (delithiation), the dramatic decrease in volume results in large tensile force inside Si particles, which in turn leads to cracking or pulverization of the Si. Such damage results in the destruction of conductive network and generates isolated Si particles that are unable to undergo further Li intercalation.[52] The failure mechanism of a nano-sized silicon composite anode is illustrated in **Figure 1.10**. Though pulverization of Si particles is hindered when the particle size is reduced from micrometers to nanometers, capacity fade still occurs. In the pristine anode, Si particles are in good contact with the polymer binder and conductive filler. Due to the repetitive volume changes during cycling, Si particles detach from the surrounding matrix, causing the loss of electrical pathways and decreased capacity. Approaches to maintain or restore the electrical interfaces are therefore highly desirable.

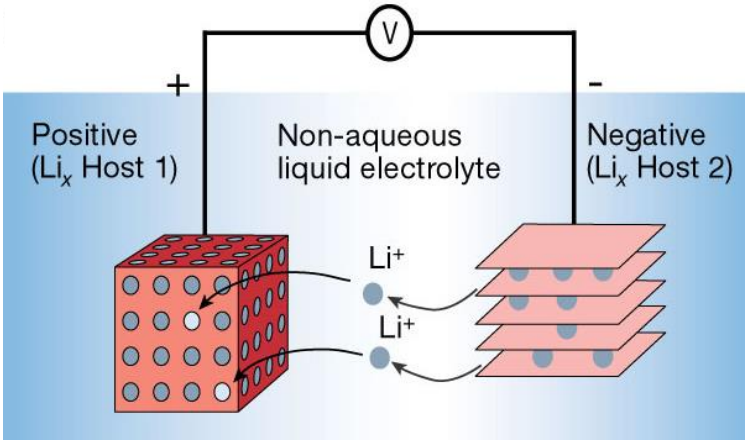


Figure 1.8. Schematic illustration of a LIB. Li ions move from negative to positive electrode during discharging and from positive to negative electrode during charging.

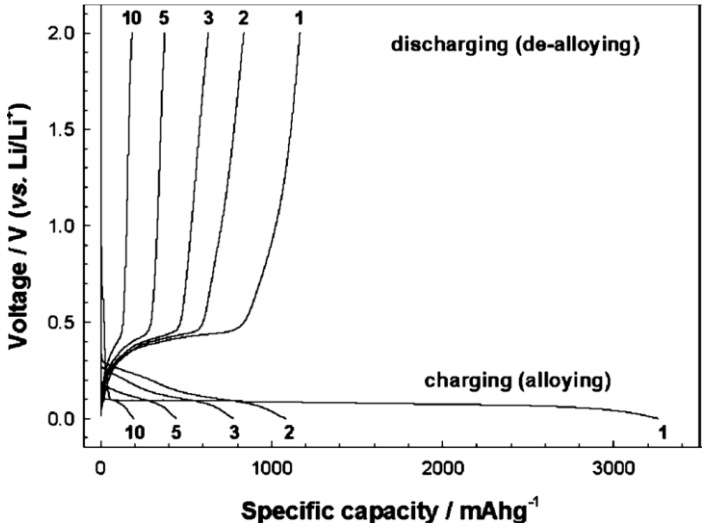


Figure 1.9. Galvanostatic charge-discharge voltage profiles of Si (10 μm) composite anode.

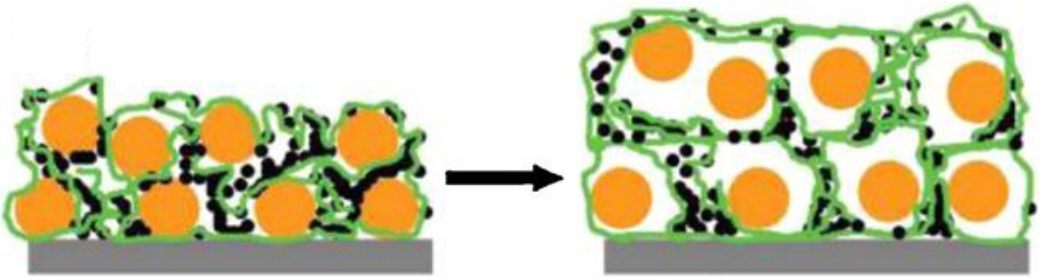


Figure 1.10. Structural change of nano-sized Si composite anode before and after cycling. The yellow particles, black particles, and green curves refer to Si particles, carbon black, and polymer binder, respectively.

Materials based strategies to overcome the large volume change and enhance capacity retention of Si anodes include the use of (1) Si particles dispersed in a rigid matrix, (2) Si thin films, (3) nanostructured Si, and (4) Si composite anodes with polymer binders.[53]

In the first strategy, Si particles are finely dispersed in a host matrix to buffer the volume change and alleviate the pulverization of Si during cycling. The matrix can be inactive (e.g. TiN, Ni) or active (e.g. Mg, C) to Li. Among all matrix materials, carbon is most attractive due to its light weight, good electrical conductivity, and moderate volume change during Li intercalation.[53] Several methods have been developed to fabricate Si/C composite anodes, such as pyrolysis or vapor deposition of carbon precursors, ball milling of Si/carbon mixtures, and chemical reaction of carbon containing gels.[54-57] Different forms of carbon are used to coat Si particles, including amorphous carbon, carbon nanotube, graphite, and graphene.

In the second strategy, Si thin films are proposed for anode materials with high specific capacity (capacity normalized by the total mass of the anode) compared to Si composite anodes which contain inactive components (i.e. polymer binder and conductive particle fillers). In thick Si films, accumulated large stress, weak adhesion to current collector, and long diffusion pathway for Li ions result in severe cracking of the film, delamination from current collector, and low rate capability, respectively.[58] Thinner Si films mitigate the stress and increase Li ion diffusion, enabling good cyclability at high cycling rate.[59] Meanwhile, roughening the current collector by sanding, chemical etching, and electrolytic deposition of Cu effectively increases the adhesion of Si thin film on current collectors.[60, 61] Patterning of Si thin film array is another method to develop crack free anodes with stable capacity.[62, 63] The individual patterned structure with small lateral dimensions (less than 10 μm) is able to reduce the film stress during Li intercalation as compared

to continuous Si film. However, the high cost of Si thin film deposition limits the application as anode materials.

The third strategy to accommodate large volume change of Si is through nanostructure design. Cui et al. reported a Si nanowire array that was directly grown onto stainless steel current collectors. The nanowire structure is able to minimize the mechanical fracture of the wires by providing an efficient pathway for electron transport.[64] The same research group later developed hollow Si nanotubes (coated with carbon) with increased surface area to reduce the Li ion diffusion pathway and increase the rate capability of the anodes.[65] Similarly, three-dimensional porous Si particles with bulk particle size (> 20 μm) and pore size of ca. 40 nm were reported with fast Li ion transport and excellent rate capability. The charge capacity after 100 cycles was greater than 2800 mAh/g at 1C rate.[66] In another example, Cui et al. developed interconnected Si hollow nanospheres with reduced tensile stress during delithiation as compared to solid Si spheres. The interconnected structure also increased Li ion diffusion during cycling.[67]

The final strategy is to develop novel binder systems for Si composite anodes. The polymer binder plays a critical role on the cycling performance of the anode as it provides binding sites to Si particles and serves as artificial solid-electrolyte interfaces (SEI), which protects Si from side reactions with the electrolyte. Conventional polyvinylidene fluoride (PVDF) binder is not suitable for Si anodes. PVDF binds with Si particles via weak van der Waals force. The weak interaction cannot tolerate high stress/strain during lithium intercalation, resulting in debonding of Si from the binder and rapid capacity decrease of the anode.[68] Several bio-derived polymers, such as carboxylmethyl cellulose (CMC), poly (acrylic acid) (PAA), and alginate, all of which contain carboxyl groups in their polymer backbone, are promising binders for good capacity retention of Si anodes.[69-73] The improvement in performance is primarily due to the formation of strong

hydrogen bonds between the polar carboxyl groups on polymer binders and the hydroxyl groups on the native SiO_2 layer on Si surfaces.[70] The dynamic hydrogen bonds undergo a self-healing process via bond dissociation and reformation and create a self-healable interface between the Si particles and polymer binder chains. Polymer binder on Si particles produces an artificial SEI with good ionic (Li ion) conductivity and minimum binder-electrolyte interactions.[69, 73] In a more recent study, catechol functional groups are introduced into alginate and PAA binders to further enhance the adhesion of binder-Si and binder-current collector interfaces.[74] In another study, cross-linked PAA-CMC polymer binder is covalently attached to Si particles via ester bond formation at the interface. The Si anodes show reduced volume (thickness) change as compared to Si/PVdF anode and improved capacity retention.[75] In conclusion, tailoring the interactions between Si surfaces and polymer binder is crucial for developing Si anodes with long cycle lifetime.

1.4 Overview of Thesis Research

In this dissertation, two different self-healing approaches for autonomous restoration of electrical interfaces in LIB electrodes (i.e. Si composite electrodes) are investigated. The first approach achieves *ex situ* restoration of electrical conductivity of damaged Si electrodes via the release of conductive payloads from capsules. As described in Chapter 2, stable capsules containing conductive carbon black suspensions are prepared with high particle loading and significant particle release upon capsule rupture. In Chapter 3, conductance restoration of a fractured electrical circuit and a damaged Si nanoparticle composite electrode is demonstrated. A protective polymer coating method, described in Chapter 4, is developed to enhance the capsule stability in battery environment.

The second approach maintains the electrical pathway during cycling of a Si electrode through the autonomous reformation of dynamic bonds inside the electrode between the binder and active particles. As described in Chapter 5, Si nanoparticles are functionalized to create dynamic ionic bonding with the electrode binder. A significant increase in capacity retention of Si electrode is also achieved.

The results of this research, summarized in Chapter 6, provide general strategies for autonomous conductivity restoration and extend the applications to self-healing battery electrodes. The encapsulation method developed for carbon black can be extended for the encapsulation of other types of particle suspensions with functionalities beyond the scope of conductivity restoration. Moreover, these self-healing approaches inspire the design of a variety of battery electrodes with improved performance.

1.5 References

[1] B. J. Blaiszik, S. L. B. Kramer, S. C. Olugebefola, J. S. Moore, N. R. Sottos, S. R. White, *Annual Review of Materials Research*, **2010**, *40*, 179.

[2] D. Y. Wu, S. Meure, D. Solomon, *Progress in Polymer Science*, **2008**, *33*, 479.

[3] S. R. White, N. R. Sottos, P. H. Geubelle, J. S. Moore, M. R. Kessler, S. R. Sriram, E. N. Brown, S. Viswanathan, *Nature*, **2001**, *409*, 794.

[4] E. N. Brown, N. R. Sottos, S. R. White, *Experimental Mechanics*, **2002**, *42*, 372.

[5] J. M. Kamphaus, J. D. Rule, J. S. Moore, N. R. Sottos, S. R. White, *Journal of The Royal Society Interface*, **2008**, *5*, 95.

[6] X. Liu, J. K. Lee, S. H. Yoon, M. R. Kessler, *Journal of Applied Polymer Science*, **2006**, *101*, 1266.

[7] M. W. Keller, S. R. White, N. R. Sottos, *Advanced Functional Materials*, **2007**, *17*, 2399.

[8] S. H. Cho, S. R. White, P. V. Braun, *Advanced Materials*, **2009**, *21*, 645.

[9] B. A. Beiermann, M. W. Keller, N. R. Sottos, *Smart Materials and Structures*, **2009**, *18*, 085001.

[10] M. M. Caruso, D. A. Delafuente, V. Ho, N. R. Sottos, J. S. Moore, S. R. White, *Macromolecules*, **2007**, *40*, 8830.

[11] M. M. Caruso, B. J. Blaiszik, S. R. White, N. R. Sottos, J. S. Moore, *Advanced Functional Materials*, **2008**, *18*, 1898.

[12] A. R. Jones, B. J. Blaiszik, S. R. White, N. R. Sottos, *Composites Science and Technology*, **2013**, *79*, 1.

[13] H. Jin, C. L. Mangun, D. S. Stradley, J. S. Moore, N. R. Sottos, S. R. White, *Polymer*, **2012**, *53*, 581.

[14] H. Jin, C. L. Mangun, A. S. Griffin, J. S. Moore, N. R. Sottos, S. R. White, *Advanced Materials*, **2014**, *26*, 282.

[15] Y. C. Yuan, M. Z. Rong, M. Q. Zhang, J. Chen, G. C. Yang, X. M. Li, *Macromolecules*, **2008**, *41*, 5197.

[16] S. Neuser, P. W. Chen, A. R. Studart, V. Michaud, *Advanced Engineering Materials*, **2014**, *16*, 581.

[17] K. S. Toohey, N. R. Sottos, J. A. Lewis, J. S. Moore, S. R. White, *Nature Materials*, **2007**, *6*, 581.

[18] K. S. Toohey, C. J. Hansen, J. A. Lewis, S. R. White, N. R. Sottos, *Advanced Functional Materials*, **2009**, *19*, 1399.

[19] C. J. Hansen, W. Wu, K. S. Toohey, N. R. Sottos, S. R. White, J. A. Lewis, *Advanced Materials*, **2009**, *21*, 4143.

[20] J. F. Patrick, K. R. Hart, B. P. Krull, C. E. Diesendruck, J. S. Moore, S. R. White, N. R. Sottos, *Advanced Materials*, **2014**, *26*, 4302.

[21] J. W. C. Pang, I. P. Bond, *Composites Science and Technology*, **2005**, *65*, 1791.

[22] H. R. Williams, R. S. Trask, I. P. Bond, *Composites Science and Technology*, **2008**, *68*, 3171.

[23] R. J. Wojtecki, M. A. Meador, S. J. Rowan, *Nature Materials*, **2011**, *10*, 14.

[24] X. Chen, M. A. Dam, K. Ono, A. Mal, H. Shen, S. R. Nutt, K. Sheran, F. Wudl, *Science*, **2002**, *295*, 1698.

[25] P. Reutenauer, E. Buhler, P. J. Boul, S. J. Candau, J. M. Lehn, *Chemistry – A European Journal*, **2009**, *15*, 1893.

[26] C. Yuan, M. Q. Zhang, M. Z. Rong, *Journal of Materials Chemistry A*, **2014**, *2*, 6558.

[27] H. Ying, Y. Zhang, J. Cheng, *Nature Communications*, **2014**, *5*.

[28] P. Cordier, F. Tournilhac, C. Soulie-Ziakovic, L. Leibler, *Nature*, **2008**, *451*, 977.

[29] D. Montarnal, F. Tournilhac, M. Hidalgo, J. Couturier, L. Leibler, *Journal of the American Chemical Society*, **2009**, *131*, 7966.

[30] S. Burattini, H. M. Colquhoun, J. D. Fox, D. Friedmann, B. W. Greenland, P. J. F. Harris, W. Hayes, M. E. Mackay, S. J. Rowan, *Chemical Communications*, **2009**, 6717.

[31] S. Burattini, B. W. Greenland, D. H. Merino, W. Weng, J. Seppala, H. M. Colquhoun, W. Hayes, M. E. Mackay, I. W. Hamley, S. J. Rowan, *Journal of the American Chemical Society*, **2010**, *132*, 12051.

[32] D. V. Andreeva, D. Fix, H. Mohwald, D. G. Shchukin, *Advanced Materials*, **2008**, *20*, 2789.

[33] Z. Wei, J. He, T. Liang, H. Oh, J. Athas, Z. Tong, C. Wang, Z. Nie, *Polymer Chemistry*, **2013**, *4*, 4601.

[34] S. J. Benight, C. Wang, J. B. H. Tok, Z. Bao, *Progress in Polymer Science*, **2013**, *38*, 1961.

[35] M. Zhu, M. Z. Rong, M. Q. Zhang, *Polymer International*, **2014**, *63*, 1741.

[36] B. J. Blaiszik, S. L. B. Kramer, M. E. Grady, D. A. McIlroy, J. S. Moore, N. R. Sottos, S. R. White, *Advanced Materials*, **2012**, *24*, 398.

[37] S. A. Odom, T. P. Tyler, M. M. Caruso, J. A. Ritchey, M. V. Schulmerich, S. J. Robinson, R. Bhargava, N. R. Sottos, S. R. White, M. C. Hersam, J. S. Moore, *Applied Physics Letters*, **2012**, *101*.

[38] M. M. Caruso, S. R. Schelkopf, A. C. Jackson, A. M. Landry, P. V. Braun, J. S. Moore, *Journal of Materials Chemistry*, **2009**, *19*, 6093.

[39] S. A. Odom, M. M. Caruso, A. D. Finke, A. M. Prokup, J. A. Ritchey, J. H. Leonard, S. R. White, N. R. Sottos, J. S. Moore, *Advanced Functional Materials*, **2010**, *20*, 1721.

[40] S. J. Pastine, D. Okawa, A. Zettl, J. M. J. Fréchet, *Journal of the American Chemical Society*, **2009**, *131*, 13586.

[41] L. Sánchez-Silva, N. Gutiérrez, P. Sánchez, A. Romero, J. L. Valverde, *Chemical Engineering Journal*, **2012**, *181–182*, 813.

[42] L. Sánchez-Silva, N. Gutiérrez, A. Romero, P. Sánchez, J. L. Valverde, *Journal of Analytical and Applied Pyrolysis*, **2012**, *94*, 246.

[43] L. Reiters, *Experimental Mechanics*, **1977**, *17*, 188.

[44] B. J. Blaiszik, A. R. Jones, N. R. Sottos, S. R. White, *Journal of Microencapsulation*, **2014**, *31*, 350.

[45] E. Palleau, S. Reece, S. C. Desai, M. E. Smith, M. D. Dickey, *Advanced Materials*, **2013**, *25*, 1589.

[46] K. A. Williams, A. J. Boydston, C. W. Bielawski, *Journal of The Royal Society Interface*, **2007**, *4*, 359.

[47] Y. Li, S. Chen, M. Wu, J. Sun, *Advanced Materials*, **2012**, *24*, 4578.

[48] B. C. K. Tee, C. Wang, R. Allen, Z. Bao, *Nature Nanotechnology*, **2012**, *7*, 825.

[49] J. M. Tarascon, M. Armand, *Nature*, **2001**, *414*, 359.

[50] H. Wu, Y. Cui, *Nano Today*, **2012**, *7*, 414.

[51] J. H. Ryu, J. W. Kim, Y. E. Sung, S. M. Oh, *Electrochemical and Solid-State Letters*, **2004**, *7*, A306.

[52] S. Bourderau, T. Brousse, D. M. Schleich, *Journal of Power Sources*, **1999**, *81–82*, 233.

[53] U. Kasavajjula, C. Wang, A. J. Appleby, *Journal of Power Sources*, **2007**, *163*, 1003.

[54] S. H. Ng, J. Wang, D. Wexler, K. Konstantinov, Z. P. Guo, H. K. Liu, *Angewandte Chemie International Edition*, **2006**, *45*, 6896.

[55] J. Shu, H. Li, R. Yang, Y. Shi, X. Huang, *Electrochemistry Communications*, **2006**, *8*, 51.

[56] C. S. Wang, G. T. Wu, X. B. Zhang, Z. F. Qi, W. Z. Li, *Journal of The Electrochemical Society*, **1998**, *145*, 2751.

[57] M. Zhou, T. Cai, F. Pu, H. Chen, Z. Wang, H. Zhang, S. Guan, *ACS Applied Materials & Interfaces*, **2013**, *5*, 3449.

[58] J. P. Maranchi, A. F. Hepp, A. G. Evans, N. T. Nuhfer, P. N. Kumta, *Journal of The Electrochemical Society*, **2006**, *153*, A1246.

[59] J. Graetz, C. C. Ahn, R. Yazami, B. Fultz, *Electrochemical and Solid-State Letters*, **2003**, *6*, A194.

[60] K. L. Lee, J. Y. Jung, S. W. Lee, H. S. Moon, J. W. Park, *Journal of Power Sources*, **2004**, *129*, 270.

[61] M. Uehara, J. Suzuki, K. Tamura, K. Sekine, T. Takamura, *Journal of Power Sources*, **2005**, *146*, 441.

[62] X. Xiao, P. Liu, M. W. Verbrugge, H. Haftbaradaran, H. Gao, *Journal of Power Sources*, **2011**, *196*, 1409.

[63] Y. He, X. Yu, Y. Wang, H. Li, X. Huang, *Advanced Materials*, **2011**, *23*, 4938.

[64] C. K. Chan, H. Peng, G. Liu, K. McIlwrath, X. F. Zhang, R. A. Huggins, Y. Cui, *Nature Nanotechnology*, **2008**, *3*, 31.

[65] M. H. Park, M. G. Kim, J. Joo, K. Kim, J. Kim, S. Ahn, Y. Cui, J. Cho, *Nano Letters*, **2009**, *9*, 3844.

[66] H. Kim, B. Han, J. Choo, J. Cho, *Angewandte Chemie*, **2008**, *120*, 10305.

[67] Y. Yao, M. T. McDowell, I. Ryu, H. Wu, N. Liu, L. Hu, W. D. Nix, Y. Cui, *Nano Letters*, **2011**, *11*, 2949.

[68] S. Komaba, N. Yabuuchi, T. Ozeki, Z. J. Han, K. Shimomura, H. Yui, Y. Katayama, T. Miura, *The Journal of Physical Chemistry C*, **2011**, *116*, 1380.

[69] I. Kovalenko, B. Zdyrko, A. Magasinski, B. Hertzberg, Z. Milicev, R. Burtovyy, I. Luzinov, G. Yushin, *Science*, **2011**, *334*, 75.

[70] J. S. Bridel, T. Azaïs, M. Morcrette, J. M. Tarascon, D. Larcher, *Chemistry of Materials*, **2009**, *22*, 1229.

[71] J. Li, R. B. Lewis, J. R. Dahn, *Electrochemical and Solid-State Letters*, **2007**, *10*, A17.

[72] A. Magasinski, B. Zdyrko, I. Kovalenko, B. Hertzberg, R. Burtovyy, C. F. Huebner, T. F. Fuller, I. Luzinov, G. Yushin, *ACS Applied Materials & Interfaces*, **2010**, *2*, 3004.

[73] B. Lestriez, S. Bahri, I. Sandu, L. Roué, D. Guyomard, *Electrochemistry Communications*, **2007**, *9*, 2801.

[74] M. H. Ryou, J. Kim, I. Lee, S. Kim, Y. K. Jeong, S. Hong, J. H. Ryu, T. S. Kim, J. K. Park, H. Lee, J. W. Choi, *Advanced Materials*, **2013**, *25*, 1571.

[75] B. Koo, H. Kim, Y. Cho, K. T. Lee, N. S. Choi, J. Cho, *Angewandte Chemie International Edition*, **2012**, *51*, 8762.

CHAPTER 2

ENCAPSULATION OF CARBON BLACK SUSPENSIONS[†]

2.1 Introduction

The encapsulation of conductive nanoparticles is challenging due to the propensity to form a pickering emulsion that causes coalescence of particles in the capsule shell wall.[1] Also, the densities of the particles are generally higher than the suspension media, leading to settling of the particles over time. Caruso et al. encapsulated pristine carbon nanotubes suspended in both chlorobenzene and ethyl phenylacetate, but the capsules were limited by significant nanotube agglomeration and low particle concentrations (0.5 mg/mL).[2] Stabilized suspensions of carbon nanotubes and graphene were later encapsulated by employing poly 3-hexylthiophene (P3HT) as a core additive, but particle concentrations remained limited to 0.5 mg/mL.[3] Jacobson et al. applied polymer coatings to the surface of titanium dioxide and black pigment particles to match the particle density to the suspension media for stable particle suspensions.[4] Other methods to create stable particle suspensions include the use of surfactants to stabilize particles and hollow particles to lower the density. Nonconductive polymer coatings and surfactant layers both reduce the conductivity of the particle network and are therefore not desirable for creating conductive suspensions.[5]

For conductivity restoration stable particle suspensions must be created to avoid entrapment of particles in the capsule shell wall or settling within the core without reducing particle conductivity after release. In addition, high particle loading and efficient particle release are desirable. Chen et al. prepared stable carbon nanotube solutions in common organic solvents by

[†] The results presented in this chapter are published in: S. Kang, A. R. Jones, J. S. Moore, S. R. White, N. R. Sottos, Microencapsulated Carbon Black Suspensions for Restoration of Electrical Conductivity. *Advanced Functional Materials*, **2014**, 24, 2947-2956.

attaching octadecyl chains to the edge of nanotubes.[6] This chapter describes two surface functionalization methods to attach hydrophobic octadecyl chains on carbon black surfaces with different surface densities. Stable carbon black suspensions are obtained in *o*-dichlorobenzene, enabling encapsulation. The effects of carbon black particle concentrations and core thickeners on capsule stability, and release of core content after capsule crushing are discussed.

2.2 Experimental

2.2.1 Materials

ACB (100 % compressed) was purchased from Alfa Aesar. OCB with the commercial name Regal® 400 was generously provided by Cabot Corporation. Dimethyl formamide (DMF), ethyl acetate, toluene, *o*-dichlorobenzene (*o*-DCB), ethyl phenylacetate (EPA), hexyl acetate (HA), dibutyl phthalate (DBP), 4-(4,6-dimethoxy-1,3,5-triazin-2-yl)-4-methylmorpholinium chloride (DMTMM), octadecylamine (ODA), 3-hexyl thiophene, ferric chloride, chloroform, ammonia, ethylenediaminetetraacetic acid (EDTA), urea, formalin solution (37 w/v%), ammonium chloride, resorcinol, and sodium bicarbonate were used as received from Sigma Aldrich. The commercial polyurethane (PU) prepolymer, Desmodur L 75, was generously provided by Bayer Material Science and used as received. Desmodur L 75 is a prepolymer solution in ethyl acetate with a reported equivalent weight of 315 g and an isocyanate content of 13.3 ± 0.4 wt %. Ethylene-maleic anhydride (EMA) copolymer (Zemac-400) powder (Mw ca. 400 kDa) was obtained from Vertellus and used as a 2.5 wt % aqueous solution. Diglycidyl ether of bisphenol A resin (DGEBA, trade name EPON 828) was used as received from Miller-Stephenson.

2.2.2 Functionalization and Characterization of Carbon Black Particles

Two approaches were used to prepare FCB, as described in **Scheme 2.1**. In Method 1[7], a stock suspension of OCB in DMF (2.5 w/v%, 160 mL) was prepared and sonicated for 12 h prior

to use. The functionalization was carried out by adding DMTMM (0.24 g) and ODA (0.24 g) into the carbon black suspension and reacting for 120 h while stirring. FCB1 was separated by centrifugation and subsequently rinsed with ethyl acetate (5 × 120 mL) to remove residual DMTMM and ODA. In Method 2 [6], OCB (2 g) was stirred in $SOCl_2$ (60 mL) and DMF (4 mL) at 75 ^oC for 24 h. The product was separated by centrifugation and then washed with anhydrous toluene. After complete removal of solvent by vacuum drying, the solid was mixed with ODA (4 g) and heated at 90 ^oC for 96 h. The ODA was removed by rinsing the crude product with ethyl acetate (5 × 60 mL) with 20 min of sonication for each rinsing step.

The average sizes of carbon black agglomerates in different solvents were measured by DLS using a Zetasizer Nano ZS (Malvern Instruments Ltd). Suspensions with 2.5 mg/g particle concentration were sonicated 3 min prior to measurement. In order to quantify the conversion ratio of carboxylic acid groups after functionalization, the -COOH content of the different types of carbon black was measured by titrating with $NaHCO_3$ solution.[8] The finishing point of titration was at the maximum consumption of $NaHCO_3$ for neutralization.

The stability of carbon black suspensions in different solvents was studied by UV-visible spectroscopy (UV-2401 PC, Shimadzu, Japan). Based on the Lambert-Beer law, a linear calibration curve of carbon black concentration as a function of absorbance (@ 800 nm) was created by measuring the absorbance of carbon black suspensions (400 to 900 nm) with five known concentrations. For the stability study, a carbon black suspension was prepared (0.067 g/mL) and allowed to settle without perturbation. An aliquot of the top layer suspension was taken and diluted 1000 times with the corresponding organic solvent at certain time intervals. The absorbance was then measured by UV-visible spectroscopy and the carbon black concentration was determined from the calibration curve.

2.2.3 Synthesis of P3HT

P3HT was prepared by the oxidative coupling polymerization of 3-hexyl thiophene according to the procedure described by Sugimoto.[9] Ferric chloride (7.8 g, 0.048 mol) was stirred in chloroform (95 mL). 3-hexylthiophene (2 g, 0.012 mol) was instantly added into the suspension. After 20 min, the reaction was terminated by the addition of deionized water. The solid product was precipitated from acidic ethanol. Subsequently, the crude product was redissolved in chloroform and the insoluble part was removed by filtering. The clear orange solution was washed by ammonia (3× 60 mL), EDTA solution (3× 60 mL), and water (3× 60 mL) successively. The final product was obtained by precipitation in ethanol, filtering, and drying. GPC (eluent: tetrahydrofuran): M_n: 44251, M_w/M_n: 2.20. ^{1}H NMR (500 MHz, $CDCl_3$, δ): 6.98 (br m, 1 H), 2.80 and 2.56 (br m, 2 H), 1.80-1.10 (br m, 8 H), 0.91 (br m, 3 H). Degree of regioregularity (ratio of head-to-tail configuration): 79 %.

2.2.4 Preparation and Characterization of Carbon Black Suspension Filled Microcapsules

The encapsulation procedure was adapted from an established PU/PUF double shell wall method.[10] The carbon black particles were dispersed in a core solvent mixture (*o*-DCB with appropriate amount of DGEBA or P3HT) with the assistance of sonication (tapered 1/800 tip sonication horn of a 750-Wultrasonic homogenizer, Cole Parmer) for at least 2 min. PU prepolymer (0.033 g/mL) was subsequently added to the encapsulation core. Upon the dissolution of PU prepolymer, the encapsulation core was added into the aqueous media at a specific stirring rate. The capsules contained 0.33 g/mL DGEBA or 0.01 g/mL P3HT in *o*-DCB. The microcapsules were rinsed with water to remove residual EMA surfactant and then filter dried to obtain free-flowing microcapsules.

Microcapsules with diameter less than 10 μm were produced by a homogenization (OMNI GLH-01) method. Homogenization was effective in reducing the emulsion droplets to submicron size as compared to mechanical agitation method. The microcapsules were centrifuged and washed with water three times to remove the residual surfactant, and then freeze dried to obtain a free-flowing powder.

Microcapsule morphology was investigated by SEM (Hitachi 4800). Before imaging, samples were sputter-coated with Au/Pd to eliminate charging effects. For capsule shell wall characterization, fully cured epoxy (DGEBA/12 wt % DETA) samples containing 5 wt % microcapsules were fractured to expose the ruptured microcapsule shell wall. The fractured pieces were then sonicated to remove encapsulated materials and leave only the capsule shell wall for imaging.

Microcapsule size distributions were obtained by analyzing the optical images of microcapsules (imaged by Leica DMR Optical Microscope) prepared at different agitation rates. For microcapsules with diameter less than 10 μm, size distributions were determined from analyzing SEM images. ImageJ software was used to measure microcapsule diameter and obtain statistical data.

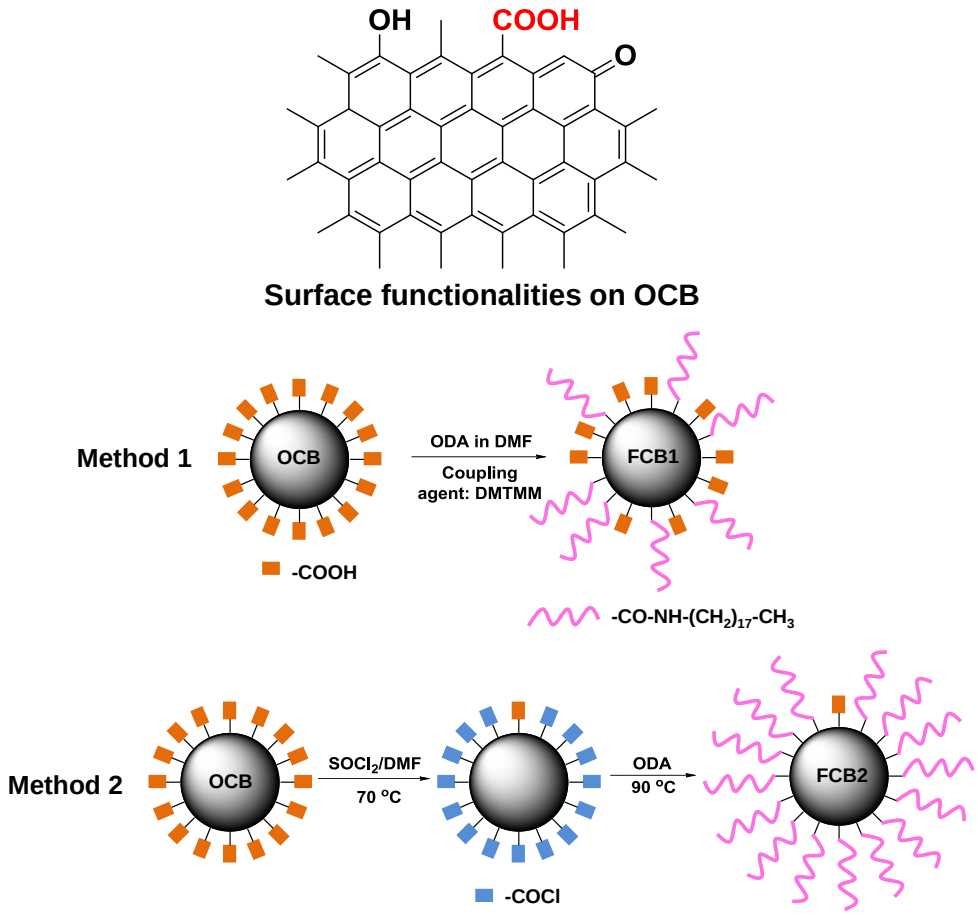
TGA was performed on a Mettler-Toledo TGA851, calibrated by indium, aluminum, and zinc standards with a heating rate of 10 ^{o}C/min from 25 to 600 ^{o}C under nitrogen atmosphere. Isothermal studies of capsules were performed at 60 ^{o}C and 150 ^{o}C for 2 h, respectively. Viscosity of encapsulated core solvents was measured with a TA Instrument AR-G2 rheometer using the double-wall concentric cylinders geometry.

2.3 Results and Discussion

2.3.1 Dispersion and Suspension of Carbon Black

The hydrophobicity of carbon black was tailored through surface functionalization to match that of the core solvent. Oxidized carbon black (OCB) was selected as the starting material because of its enriched surface reactive functional groups (e.g. carboxylic acid, carbonyl, phenolic hydroxyl, and lactone). Enhanced hydrophobicity was achieved through covalent bonding of octadecyl (-$C_{18}H_{37}$) groups on the OCB surface by two different methods (**Scheme 2.1**).

While the target products were the same, the conversion ratio varied depending on the method of functionalization. The amount of unconverted carboxylic acid groups on the carbon black surface was determined by titration. The carboxylic acid content in as-received OCB was 0.103 meq/g, as expected from prior literature.[11] FCB1 contained 0.055 meq/g and FCB2 contained 0.008 meq/g carboxylic acid, yielding a conversion ratio of 47 % and 92 %, respectively. The surface density of octadecyl groups on FCB2 was about twice that of FCB1, yielding an increased hydrophobicity of FCB2 relative to FCB1. The CHN elemental analysis results (**Table 2.1**) also showed increasing nitrogen content from FCB1 to FCB2 resulting from amide bond formation.



Scheme 2.1. Surface functionalization of OCB. Octadecyl groups were covalently attached on the OCB surface by two methods, yielding different conversion ratios.

Table 2.1. CHN elemental analysis of OCB, FCB1 and FCB2.

Sample type	Carbon [wt %]	Hydrogen [wt %]	Nitrogen [wt %]
OCB	94.43 ± 0.04	0.17 ± 0.06	0.43 ± 0.02
FCB1	94.55 ± 0.32	0.45 ± 0.02	0.59 ± 0.00
FCB2	94.43 ± 0.01	1.07 ± 0.05	0.90 ± 0.01

To evaluate the dispersion of FCBs, we measured the particle agglomerate sizes in several weakly polar solvents: *o*-dichlorobenzene (*o*-DCB), ethyl phenylacetate (EPA), hexyl acetate (HA), and dibutyl phthalate (DBP) using dynamic light scattering (DLS) (**Table 2.2**). Data for

unfunctionalized OCB and acetylene carbon black (ACB) are also included in **Table 1** for comparison. Unlike OCB, ACB is a type of conventional carbon black with fewer hydrophilic surface functional groups. Both OCB and ACB have single particle diameters of ca. 40 nm (**Figure 2.1**). In weakly polar solvents, the particle agglomerate sizes for both FCB1 and FCB2 were smaller than that of OCB and ACB, suggesting enhanced dispersions due to increased surface hydrophobicity. Wu et al.[12] have also reported that the bulky surface octadecyl groups minimize electrostatic interaction between carbon black particles and reduce agglomeration. The relatively larger FCB2 agglomerate sizes compared to FCB1 is likely due to the formation of ester bonds by the reactive acyl chloride groups on one carbon black particle with the hydroxyl groups of neighboring particles during the first step of preparing FCB2. The best dispersion was achieved in *o*-DCB, which was selected as the solvent for encapsulation. Two types of core thickeners, Bisphenol A diglycidyl ether (DGEBA, trade name EPON 828) and poly 3-hexylthiophene (P3HT), were also examined by dissolving in *o*-DCB. The addition of the core thickeners did not significantly change the agglomerate sizes.

Table 2.2. Particle size distribution of different types of carbon black in various solvents.

solvent	Z-average particle size, diameter [nm]			
	OCB	ACB	FCB1	FCB2
***o*-DCB**	725 ± 614	285 ± 201	156 ± 84	169 ± 97
HA	961 ± 868	3365 ± 2211	821 ± 522	897 ± 731
EPA	3835 ± 2119	3684 ± 2406	1357 ± 789	1862 ± 1168
DBP	1724 ± 1140	2446 ± 1478	265 ± 169	552 ± 401
***o*-DCB/DGEBA**	500 ± 368	312 ± 229	112 ± 50	265 ±158
***o*-DCB/P3HT**	294 ± 216	961 ± 699	204 ± 103	143 ± 49

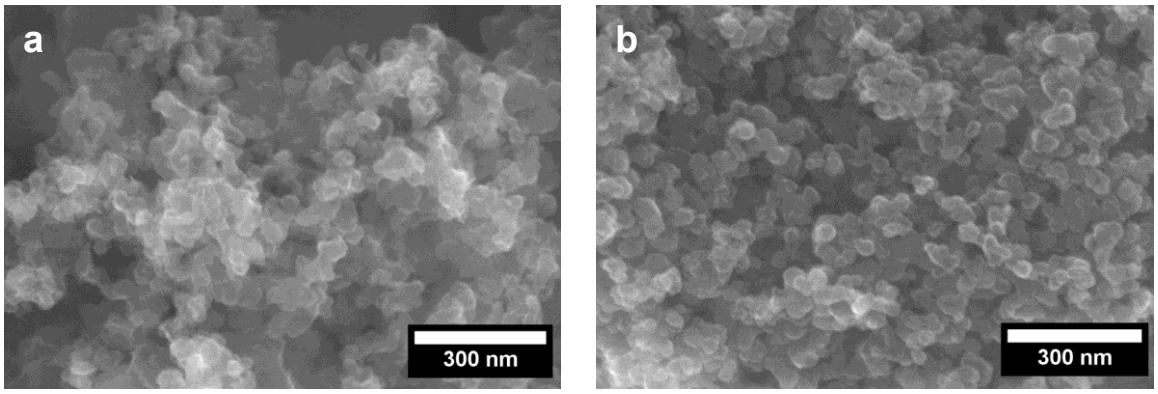


Figure 2.1. SEM images of a) OCB and b) ACB particles.

The long term stability of suspended carbon black particles in the core solvent is of particular importance, since the precipitation of carbon black after encapsulation can lead to reduced carbon black release upon capsule rupture. Re-agglomeration of ACB and OCB in *o*-DCB was observed after 2 h of DLS measurement while both FCB1 and FCB2 retained uniform dispersions (**Figure 2.2**). The particle concentrations of aliquots taken from the top layer of carbon black suspensions in scintillation vials were monitored by UV-visible spectroscopy, as shown in **Figure 2.3**. All types of carbon black precipitated within one day in EPA and HA. A slower precipitation rate was observed in DBP, primarily due to its high viscosity. In contrast, FCBs showed good suspension stability in *o*-DCB, with only a minimal concentration decrease over 20 days. FCB2 exhibited slightly better stability than FCB1 due to the higher octadecyl surface coverage. A significantly lower concentration of OCB and ACB in *o*-DCB was observed.

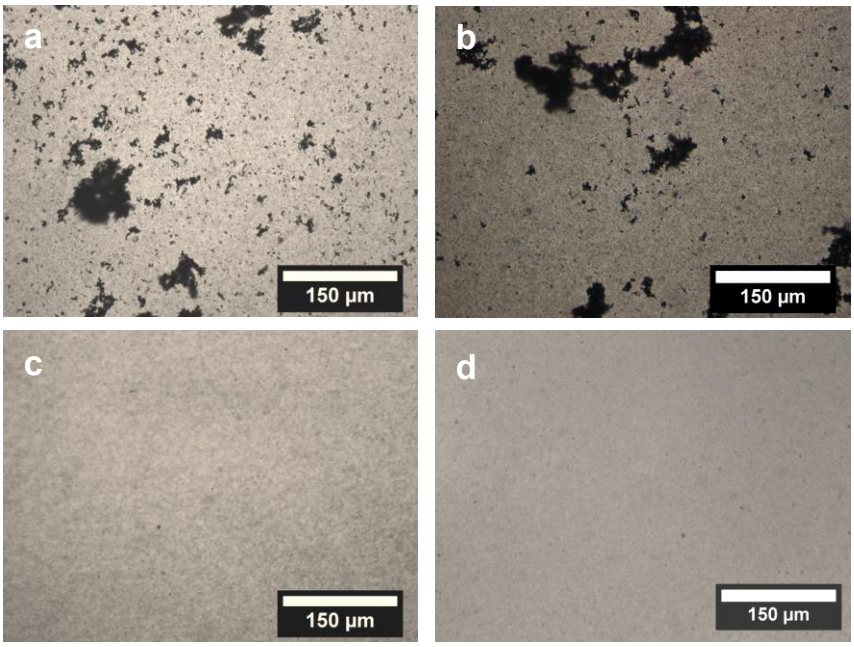


Figure 2.2. Optical images of a) ACB, b) OCB, c) FCB1, and d) FCB2 dispersed in *o*-DCB. Images were taken 2 h after sonication.

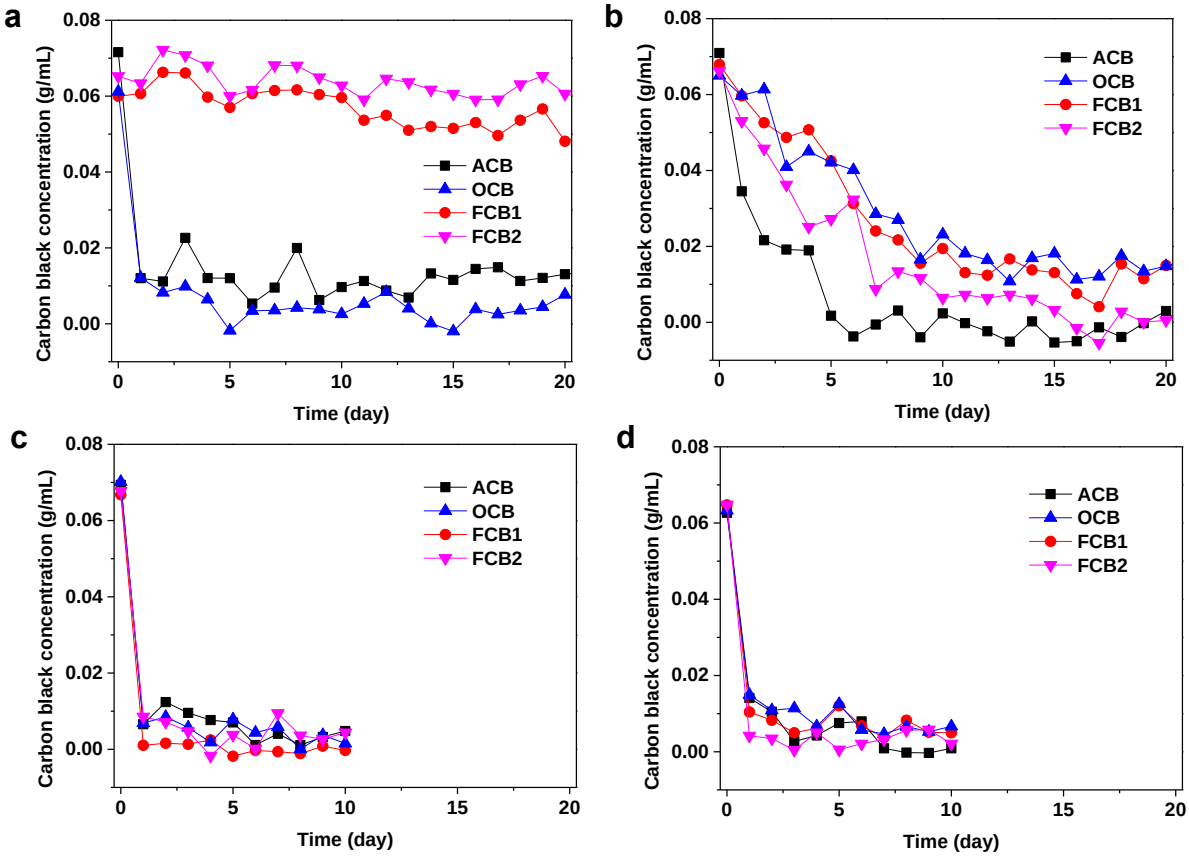


Figure 2.3. Concentration change of carbon black in suspensions (top layer) measured by UV-visible spectroscopy. The suspension solvents are a) *o*-DCB, b) DBP, c) EPA, and d) HA.

2.3.2 Encapsulation of Carbon Black

Varying types and concentrations of carbon black were encapsulated in polyurethane (PU)/poly urea-formaldehyde (PUF) double shell wall microcapsules. Capsules with diameters ranging from 20-240 μm were produced by mechanical agitation (**Figure 2.4**a). Smaller capsules (less than 10 μm in diameter) were achieved by using a homogenizer (**Figure 2.4**b). A summary of all the different encapsulated core materials is provided in **Table 2.3**. The maximal particle loading achieved was 0.2 g/mL (ca. 13 % in volume), which represents a significant improvement compared to recently published values for carbon based particle encapsulations.[2-4, 13-16] Further increase of the FCB loading led to high viscosity and immobility of the core. No residual carbon black was observed in the aqueous phase after encapsulation, indicating nearly complete encapsulation of FCB. In contrast, a maximum loading of only 0.05 g/mL (ca. 3 % in volume) ACB was encapsulated. OCB was not able to be encapsulated due to the migration of the hydrophilic particles from the core to the aqueous phase during encapsulation.

Scanning electron microscopy (SEM) was performed to characterize microcapsule morphology. As shown in **Figure 2.5**a, the microcapsule exterior surface consists of a smooth and continuous PUF layer with embedded PUF nanoparticles.[17] The cross-sectional image of a ruptured capsule (**Figure 2.5**b, embedded in epoxy matrix) shows a ca. 200 nm thick microcapsule shell wall composed of PUF and a rough inner layer composed of PU and embedded carbon black particles entrapped by the PU prepolymer during encapsulation. The smaller microcapsules (**Figure 2.5**c and **2.5**d) with 2 μm average diameter prepared by the homogenization method had a smoother exterior surface and thinner shell wall of ca. 40 nm.

Table 2.3. Summary of different encapsulated core materials.

Microcapsule type	Carbon black concentration [g/mL]	Core thickener concentration [g/mL]
NCB (no carbon black)	0	0
NCB/DGEBA	0	0.33 g/mL DGEBA
NCB/P3HT	0	0.01 g/mL P3HT
ACB	0.05 g/mL ACB	0
FCB1L	0.067 g/mL FCB1	0
FCB1L/DGEBA	0.067 g/mL FCB1	0.33 g/mL DGEBA
FCB1M/DGEBA	0.133 g/mL FCB1	0.33 g/mL DGEBA
FCB1H/DGEBA	0.200 g/mL FCB1	0.33 g/mL DGEBA
FCB1L/P3HT	0.067 g/mL FCB1	0.01 g/mL P3HT
FCB1L/P3HT (2 μm)[a)]	0.067 g/mL FCB1	0.01 g/mL P3HT
FCB1M/P3HT	0.133 g/mL FCB1	0.01 g/mL P3HT
FCB1H/P3HT	0.200 g/mL FCB1	0.01 g/mL P3HT
FCB2L	0.067 g/mL FCB2	0
FCB2L/P3HT	0.067 g/mL FCB2	0.01 g/mL P3HT
FCB2M/P3HT	0.133 g/mL FCB2	0.01 g/mL P3HT
FCB2H/P3HT	0.200 g/mL FCB2	0.01 g/mL P3HT

a) Average microcapsule diameter is 2 μm. All the other types of capsules are ca. 200 μm in diameter.

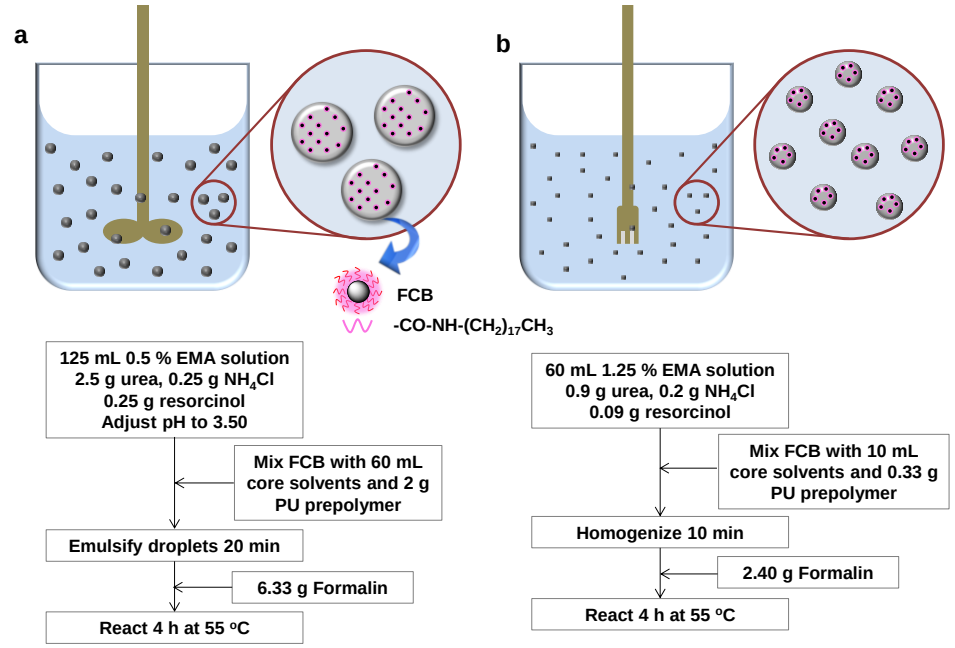


Figure 2.4. Encapsulation methods for preparing PU/PUF double shell wall capsules containing FCB suspensions using a) mechanical agitation and b) homogenization.

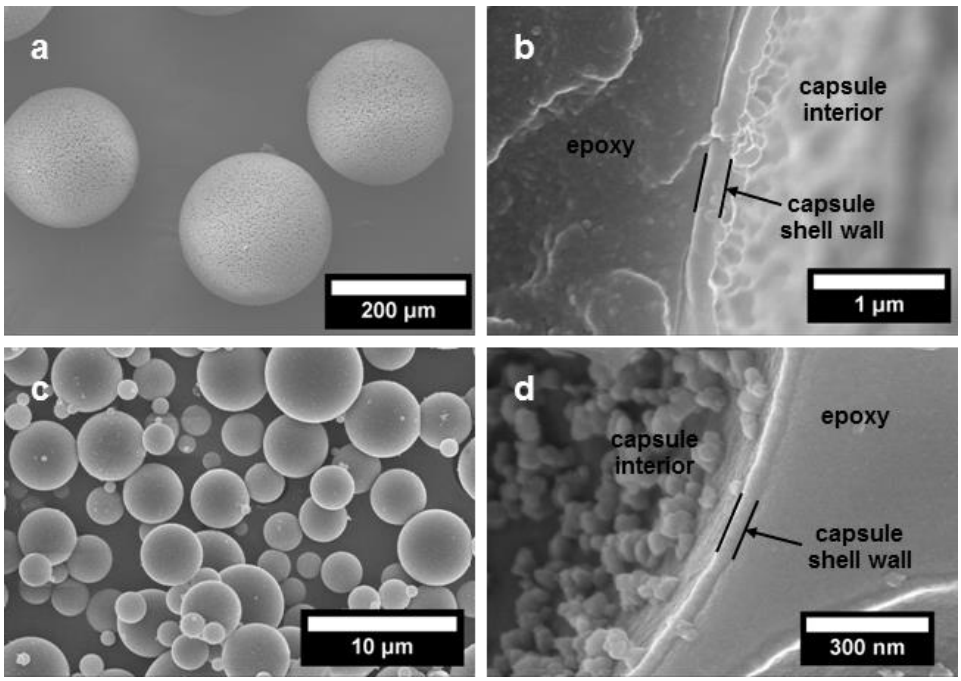


Figure 2.5. SEM images of FCB1H/P3HT microcapsules.
a) Large microcapsules (200 µm average diameter) have a rough exterior surface.
b) Cross section of large microcapsules reveals microcapsule shell wall of ca. 200 nm.
c) Small microcapsules (2 µm average diameter) have a smooth exterior surface.
d) Cross section of small microcapsules reveals microcapsule shell wall of ca. 40 nm.

Microcapsule size decreased with increasing agitation rate following a power law relationship (**Figure 2.6**a).[10] A broader size distribution was observed for all FCB1 filled microcapsules (**Figure 2.6**b and **2.6**c) as compared to solvent-only systems.[18, 19] We hypothesized that the high viscosity of the continuous organic phase caused the coalescence of small emulsion droplets during encapsulation and broadened the size distribution. The microcapsule size increased from 133 μm to 259 μm after tripling the FCB1 loading from 0.067 g/mL to 0.2 g/mL (in the presence of 0.33 g/mL DGEBA, 400 rpm agitation rate) due to the increase of core viscosity.

The addition of core thickeners (DGEBA and P3HT) into the encapsulated core led to an increase of core viscosity, as shown in **Table 2.4**. The mixture viscosity was doubled by increasing the concentration of core thickeners in *o*-DCB. A lower concentration of P3HT than DGEBA was required to reach the same viscosity of the mixture. This difference is primarily due to the extended long chain conformation of P3HT in *o*-DCB, which is absent in DGEBA.

Table 2.4. Viscosity of *o*-DCB/core thickener mixtures.

Mixture	*o*-DCB	0.17 g/mL DGEBA in *o*-DCB	0.33 g/mL DGEBA in *o*-DCB	0.01 g/mL P3HT in *o*-DCB	0.02 g/mL P3HT in *o*-DCB
Viscosity [cP]	1.31	2.20	4.44	2.60	5.04

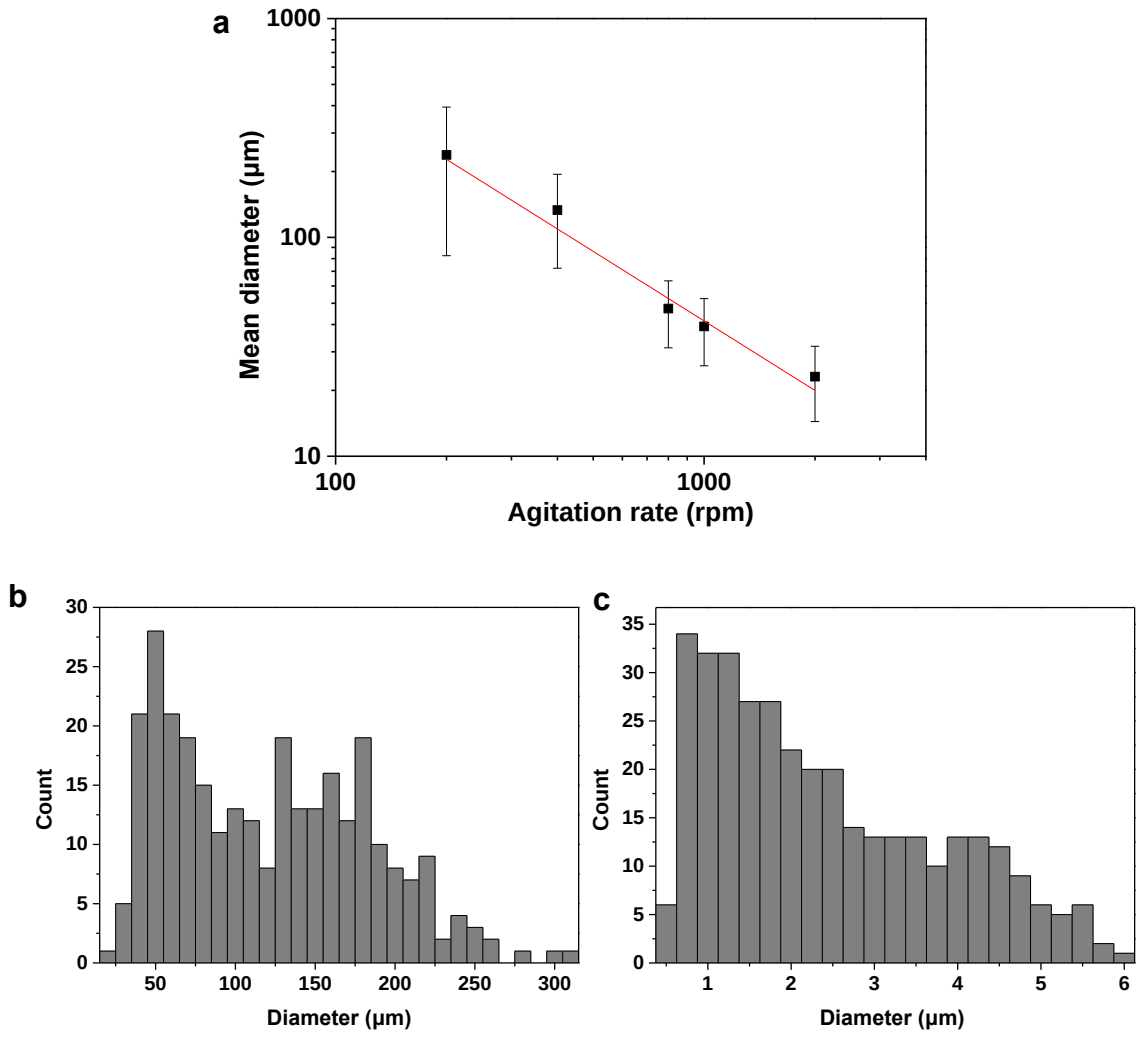


Figure 2.6. Size characterization of FCB1 filled microcapsules. a) Mean diameter of FCB1L/DGEBA microcapsules obtained by optical measurement as a function of agitation rate. Vertical error bars represent one standard deviation. b) Representative microcapsule diameter histogram showing the size distrubtion for capsules made by mechanical agitation at 400 rpm (Average diameter = 133 μm). c) Representative microcapsule diameter histogram showing the size distribution for capsules made by homogenization (Average diameter = 2 μm).

Thermal stability of microcapsules was characterized by thermal gravimetric analysis (TGA). Representative TGA curves of different microcapsules are shown in **Figure 2.7**a. Distinct weight loss was observed for all microcapsules with an onset temperature of 160 ^{o}C attributed to the start of *o*-DCB (bp 180 ^{o}C) evaporation. For the microcapsules containing DGEBA (0.33 g/mL), the mass loss from 265 to 445 ^{o}C was attributed to decomposition of the resin component.

The decomposition of P3HT was not detected due to its low concentration (0.01 g/mL). An isothermal study of microcapsules was conducted at 60 °C or 150 °C for 2 h (**Figure 2.7**b and **2.7**c). The weight loss of all microcapsules was less than 0.7 wt % at 60 °C and less than 2 wt% at 150 °C. Based on thermal stability, the incorporation of FCB and core thickeners did not compromise the capsule shell wall quality.

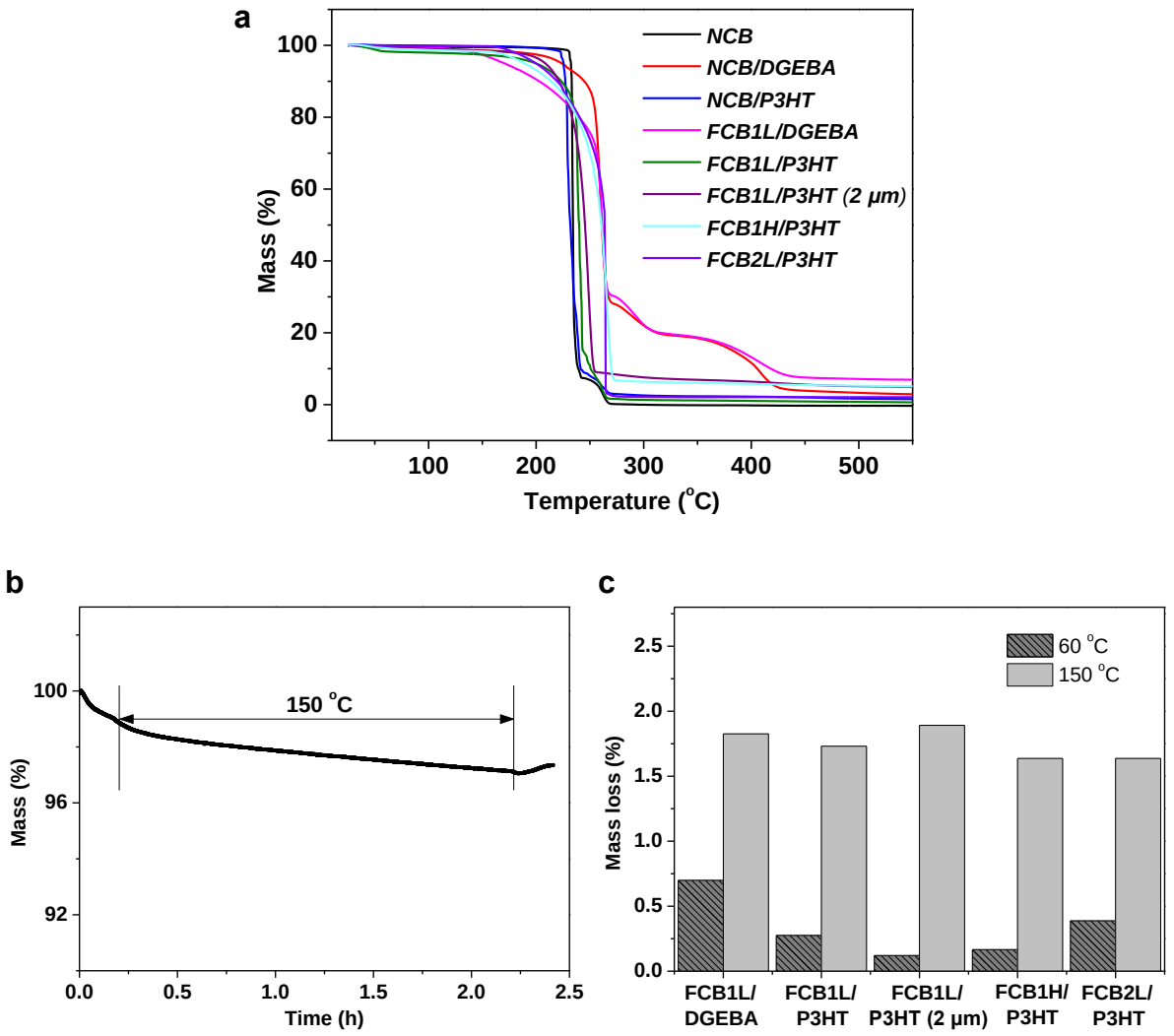


Figure 2.7. Thermal characterization of microcapsules. a) Dynamic TGA curves of prepared microcapsules with varying core contents. Encapsulated core materials are defined in Table 2. b) Representative isothermal curve of FCB1L/P3HT microcapsules at 150 °C. c) Percentage mass loss of microcapsules under isothermal condition (60 °C and 150 °C, 2 h).

2.3.3 Release of Carbon Black upon Capsule Rupture

The release of carbon black particles was examined by optical microscopy and SEM after microcapsules were ruptured by crushing between two glass slides. As shown in **Figure 2.8**a-c, ACB filled microcapsules had no visible particle release. In aliquots of the encapsulation emulsion taken prior to microcapsule shell wall formation, ACB particles preferentially resided on the oil/water interface and showed no movement due to the adsorption of surfactant. As a result, ACB particles were entrapped in the shell wall during encapsulation. In contrast, the FCB1 and FCB2 microcapsules both exhibited particle release, especially FCB2 (**Figure 2.8**d-i). Fast brownian motion of the FCB particles in the oil phase was observed in the emulsion prior to encapsulation, suggesting a minimal effect from surfactant adsorption. Adsorption by PU prepolymer and adhesion to the capsule shell wall inhibited the release of FCB1. The enhanced particle release of FCB2 is due to the higher octadecyl group coverage of FCB2 compared to FCB1.

The addition of core thickeners, DGEBA and P3HT, further promoted the release of FCB particles. In the absence of core thickener, FCB1 capsules showed a small amount of particle release upon rupture (**Figure 2.8**d-f). A clear trend of enhanced FCB1 release by incorporating DGEBA and P3HT into the core was observed in **Figure 2.8**j-l and **2.8**m-o. By dispersing FCB in a more viscous core, adsorption by PU prepolymer was minimized and adhesion to capsule shell wall was reduced. Furthermore, P3HT has the ability to stabilize dispersed FCB suspensions through π-π stacking interactions.[20] The combined viscosity enhancement and aromatic stacking effects make P3HT a superior candidate as a core thickener for stabilizing FCB suspensions.

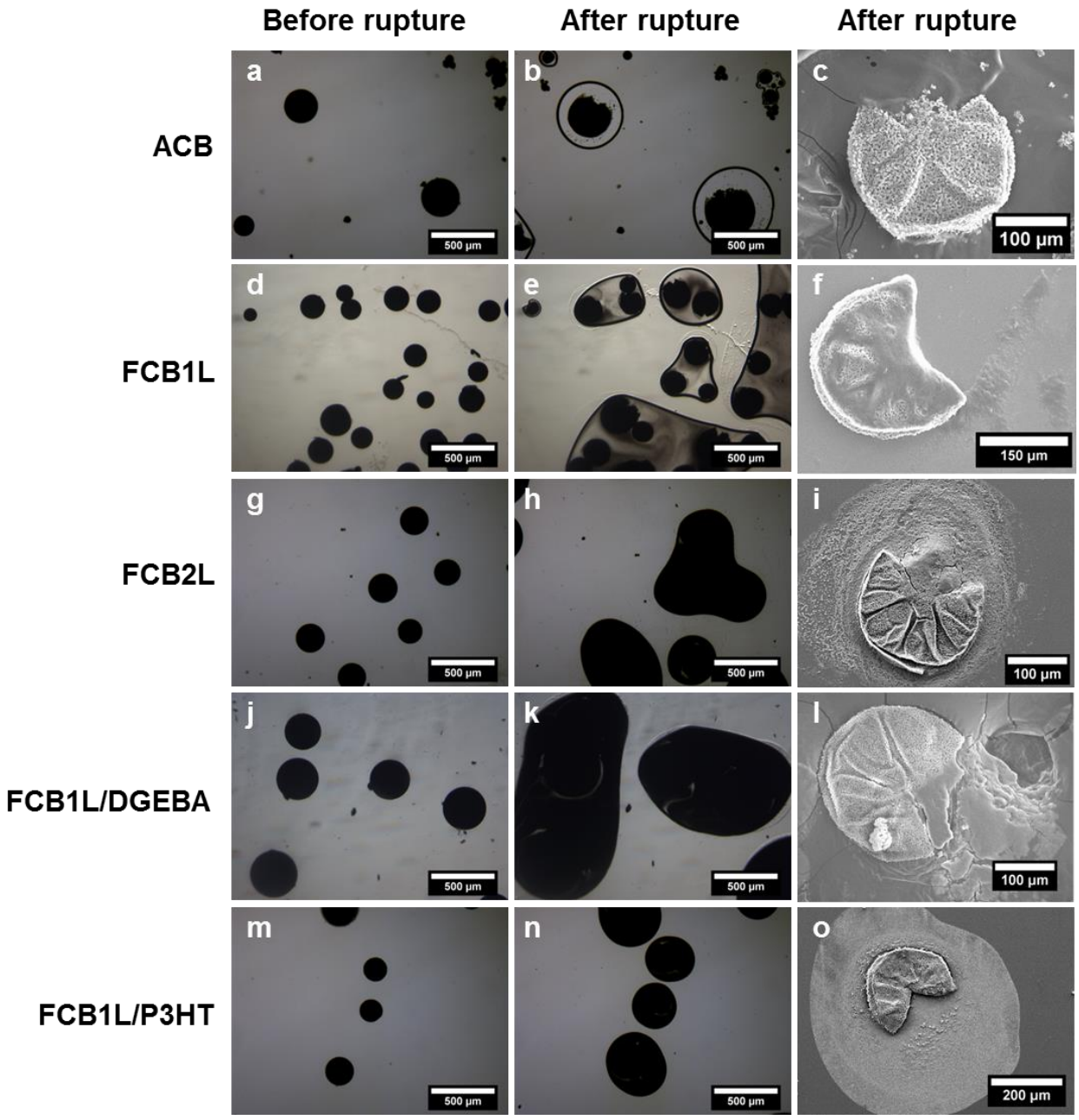


Figure 2.8. Optical and SEM images of pristine and ruptured carbon black microcapsules with different cores. Column 1 and Column 2 contain optical images of microcapsules before and after rupture, respectively. Column 3 contains SEM images of ruptured microcapsules and the released core. a-c) ACB, d-f) FCB1L, g-i) FCB2L, j-l) FCB1L/DGEBA, m-o) FCB1L/P3HT. Capsule core contents are summarized in Table 2.

2.4 Conclusions

Two types of FCB with different hydrophobicity were prepared by controlling the concentration of octadecyl chains on the particle surface. Surface functionalization resulted in improved dispersion properties and suspension stability of carbon black in *o*-DCB due to an increased hydrophobicity from octadecyl groups. Robust microcapsules with high loading of FCB (up to 0.2 g/mL) were achieved. The capsule size was controlled from submicron to a few hundred microns. The capsules also exhibited good stability at elevated temperature (150 ^{o}C). Substantial particle release was observed after crushing of FCB microcapsules. The incorporation of DGEBA or P3HT as core thickener increased the amount of FCB release by increasing the core viscosity and stabilizing the particles.

2.5 References

[1] D. J. Voorn, W. Ming, A. M. van Herk, *Macromolecules*, **2006**, *39*, 2137.

[2] M. M. Caruso, S. R. Schelkopf, A. C. Jackson, A. M. Landry, P. V. Braun, J. S. Moore, *Journal of Materials Chemistry*, **2009**, *19*, 6093.

[3] S. A. Odom, T. P. Tyler, M. M. Caruso, J. A. Ritchey, M. V. Schulmerich, S. J. Robinson, R. Bhargava, N. R. Sottos, S. R. White, M. C. Hersam, J. S. Moore, *Applied Physics Letters*, **2012**, *101*.

[4] B. Comiskey, J. D. Albert, H. Yoshizawa, J. Jacobson, *Nature*, **1998**, *394*, 253.

[5] X. Li, Y. Xiong, L. Zou, M. Wang, Y. Xie, *Microporous and Mesoporous Materials*, **2008**, *112*, 641.

[6] J. Chen, M. A. Hamon, H. Hu, Y. Chen, A. M. Rao, P. C. Eklund, R. C. Haddon, *Science*, **1998**, *282*, 95.

[7] G. Blotny, *Tetrahedron*, **2006**, *62*, 9507.

[8] H. P. Boehm, E. Diehl, W. Heck, R. Sappok, *Angewandte Chemie International Edition in English*, **1964**, *3*, 669.

[9] R. Sugimoto, S. Takeda, G. H. B., K. Yoshino, *Chemistry Express*, **1986**, *1*, 635.

[10] M. M. Caruso, B. J. Blaiszik, H. Jin, S. R. Schelkopf, D. S. Stradley, N. R. Sottos, S. R. White, J. S. Moore, *ACS Applied Materials & Interfaces*, **2010**, *2*, 1195.

[11] J. M. O'Reilly, R. A. Mosher, *Carbon*, **1983**, *21*, 47.

[12] G. Wu, P. Yin, R. Dai, M. Wang, H. Chen, H. Li, D. Liu, *Journal of Materials Research*, **2012**, *27*, 653.

[13] L. Sánchez-Silva, N. Gutiérrez, P. Sánchez, A. Romero, J. L. Valverde, *Chemical Engineering Journal*, **2012**, *181–182*, 813.

[14] L. Sánchez-Silva, N. Gutiérrez, A. Romero, P. Sánchez, J. L. Valverde, *Journal of Analytical and Applied Pyrolysis*, **2012**, *94*, 246.

[15] S. J. Pastine, D. Okawa, A. Zettl, J. M. J. Fréchet, *Journal of the American Chemical Society*, **2009**, *131*, 13586.

[16] L. Reiters, *Experimental Mechanics*, **1977**, *17*, 188.

[17] E. N. Brown, M. R. Kessler, N. R. Sottos, S. R. White, *Journal of Microencapsulation*, **2003**, *20*, 719.

[18] D. A. McIlroy, B. J. Blaiszik, M. M. Caruso, S. R. White, J. S. Moore, N. R. Sottos, *Macromolecules*, **2010**, *43*, 1855.

[19] B. J. Blaiszik, M. M. Caruso, D. A. McIlroy, J. S. Moore, S. R. White, N. R. Sottos, *Polymer*, **2009**, *50*, 990.

[20] J. Zou, L. Liu, H. Chen, S. I. Khondaker, R. D. McCullough, Q. Huo, L. Zhai, *Advanced Materials*, **2008**, *20*, 2055.

CHAPTER 3

RESTORATION OF ELECTRICAL CONDUCTIVITY AFTER MECHANICAL DAMAGE[†]

3.1 Introduction

Maintaining a long lifespan and high reliability in electronic components and devices are highly desirable.[1, 2]. However, damage induced by mechanical and/or thermal cycling of microelectronic devices is inevitable. The resultant loss of conductive pathway requires the replacement of failed pieces, which significantly increases the cost. Autonomous repair of damaged sites via the formation of conductive bridge provides a facile and efficient approach to resolve this critical issue. Our recent study demonstrates this concept by using core-shell microcapsules that release conductive core on demand. Examples of conductive liquid core include carbon nanotube (CNT) suspensions, charge transfer salt solution, and liquid gallium-indium (Ga-In) alloy.[3-6]

As described in Section 1.2, in lithium-ion batteries (LIB), the damage of electrical interfaces in electrodes leads to significant capacity loss, especially in high capacity Si anodes. Battery electrodes are composite materials consisting of active particles such as graphite or Si and a polymer binder. Conductive carbon black nanoparticles are often added to the electrodes to fill the interstitial regions and increase electrical conductivity.[7] With the successful encapsulation of carbon black suspensions as described in Chapter 2, we evaluate the conductivity restoration of damaged Si anodes and electric circuits.

[†] The content of this chapter is partially published in: S. Kang, A. R. Jones, J. S. Moore, S. R. White, N. R. Sottos, Microencapsulated Carbon Black Suspensions for Restoration of Electrical Conductivity. *Advanced Functional Materials*, **2014**, 24, 2947-2956.

3.2 Experimental

3.2.1 Materials

ACB (100 % compressed) was purchased from Alfa Aesar. Titanium (IV) butoxide and sodium carboxymethyl cellulose (CMC, Mw ~700,000) were used as received from Sigma Aldrich. Silicon nanoparticles (100 nm) were obtained from MTI Corporation. EPON 862 and diethylenetriamine (DETA) were from Miller-Stephenson. Microcapsules were prepared using the procedure described in Chapter 2.

3.2.2 Conductivity Restoration of Fractured Si Anodes

Silicon anode specimens for evaluating conductance restoration were fabricated with a controlled crack size by a fiber removal method (**Figure 3.1**). An 8 μm diameter glass fiber was adhered to a glass slide by tape. The glass slide was then dipped in titanium butoxide solution (9 %) in ethanol and dried. The titanium (IV) butoxide served as a blocking layer to prevent the penetration of Si anode slurry into the gap between the glass fiber and the glass slide. The Si anode slurry consisted of 7 wt% Si nanoparticles (100 nm), 2 wt% CMC, and 1 wt% ACB in deionized water. A doctor blade was used to cast a uniform layer of the slurry on glass. After drying at room temperature for 24 h, the fiber was carefully pulled out, creating a 10 μm wide line crack on the Si anode. FCB filled microcapsules were deposited onto the line crack and crushed with a cover slide. The conductance change of the Si anode was measured by a Wheatstone bridge setup described previously by Blaiszik et al.[6] The specimen conductance G was calculated,

$$G = \frac{G_3}{\frac{V_B}{V_G} + \frac{G_1}{G_1 + G_2}} \qquad \text{Eq. 3.1}$$

where V_B is the bridge voltage, V_G is supplied voltage (V_G =5 V), and G_1 , G_2, and G_3 are the conductance of the other resistors (G_1=0.0909 Ω^{-1}, G_2=0.0091 Ω^{-1}, G_3= 10^{-4} Ω^{-1}) in Wheatstone bridge, respectively.

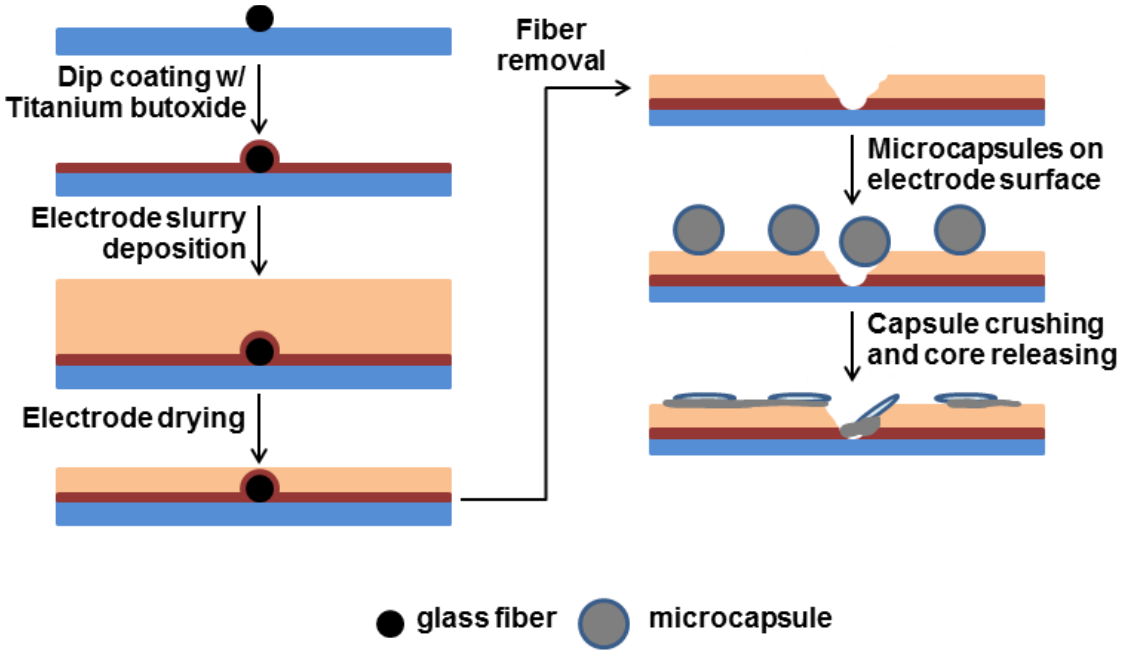


Figure 3.1. Schematic representation of fiber removal method to create a thin line crack.

3.2.3 Conductivity Restoration of Fractured Electric Circuit

A conductive Au line was incorporated into a model multilayer device to evaluate the conductivity restoration after mechanical damage (**Figure 3.2**). An Au/Cr film (Au 100 nm thick, Cr 10 nm thick) was deposited onto a notched glass (notch depth 500 μm) substrate using electron-beam deposition. An epoxy dielectric layer (EPON 862 + DETA) with embedded FCB1 capsules (70 wt%, capsule core: FCB1H/P3HT, refer to **Table 2.3** for details) was deposited on top of the Au/Cr film. The thickness of the epoxy layer was controlled to be ca. 250 μm by adding glass spacing beads with 180-250 μm diameter. A ductile acrylic top layer was used to provide controlled crack opening and repeatable circuit failure in four-point bending tests.

A four-point bend loading frame was used to create the damage on multilayer specimen. As illustrated in **Figure 3.2**, the top and bottom pin spacing was 16 mm and 55 mm, respectively. Load cell (Futek LSB200–45 N max capacity), amplifier (Omega DP25B-S-A), and linear actuator

(Physik Instrumente M-230.25 S) were used for displacing the top fixture with a displacement rate of 1 μm/s, and LabVIEW 2009 for actuator control and load data acquisition.

The conductivity change of the multilayer circuit was monitored using a Wheatstone bridge setup. The performance was evaluated by measuring the normalized bridge voltage, $V_{norm}=(V_B-V_\infty)/(V_o-V_\infty)$, where V_0 is the bridge voltage before damage, V_∞ is the bridge voltage for a fully broken circuit, and V_B is the bridge voltage. The conductivity restoration efficiency η is defined as the normalized voltage, ranging from 0 to 1. The specimen resistance was calculated using equation 3.1 with G_1=0.0909 Ω^{-1}, G_2=0.0091 Ω^{-1}, and G_3= 1.96×10^{-5} Ω^{-1} in Wheatstone bridge.

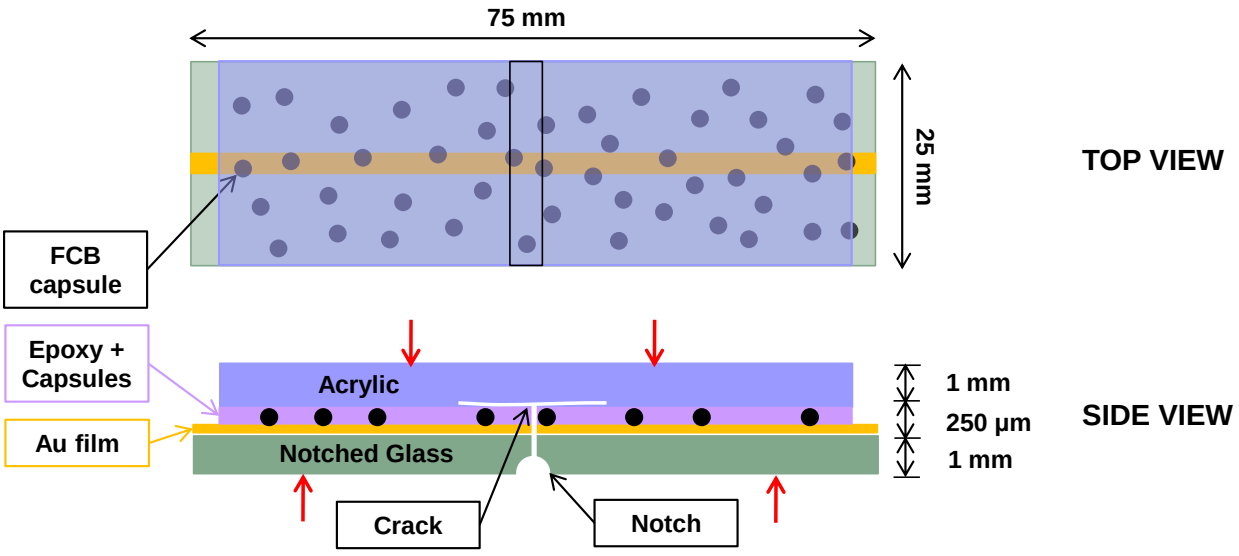


Figure 3.2. Schematic representation of the multilayer specimen. The bending directions are indicated by the red arrows.

3.3 Results and Discussion

3.3.1 Si anode Conductivity Restoration

The restoration of conductance in a battery anode material was evaluated by a fiber removal protocol (described in 3.2.2) in which a line crack (ca. 10 μm width) was created on a nanoparticle Si anode by removing a glass fiber (8 μm diameter) from underneath. Conductance restoration of

the damaged Si anode was evaluated by either depositing the capsule core material (ca. 1 mg) directly onto the crack region or crushing carbon black filled microcapsules (ca. 1 mg) on the line crack. **Figure 3.3** shows the line crack in the anode prior to testing and the release of FCB1 particles on the line crack after capsule crushing.

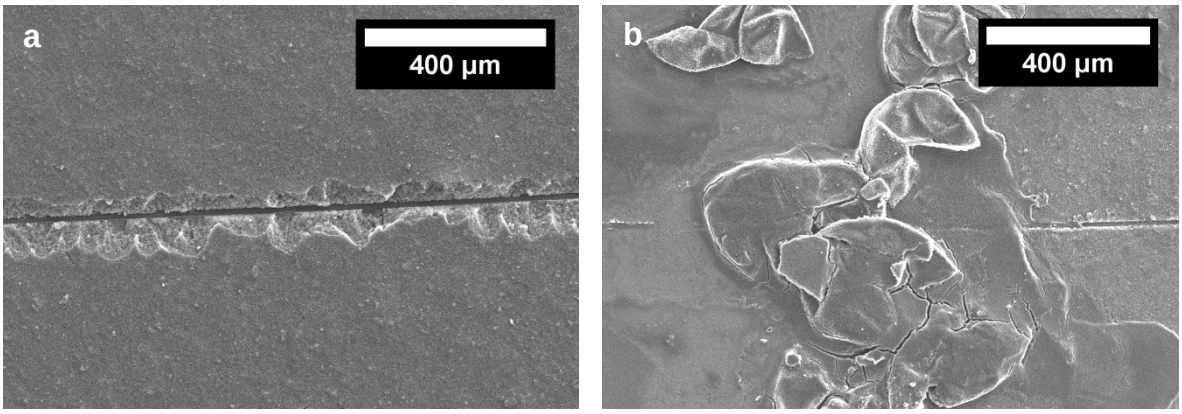


Figure 3.3. SEM images of a) a line crack introduced by fiber removal protocol in a nanoparticle Si anode and b) ruptured FCB1H/DGEBA microcapsules and release of carbon black onto a line crack.

Removal of the fiber resulted in complete loss of conductivity across the anode. Direct deposition of the core material (**Figure 3.4**a) led to a monotonic increase of conductance with time as the solvent evaporated. Full recovery was obtained after ca. 400 sec. When capsules were crushed directly on the line crack, full recovery was reached after about 500 sec. (**Figure 3.4**b).

The conductance restoration efficiency is defined as:

$$\eta_G = \frac{G_h}{G_0} \qquad \text{Eq. 3.2}$$

where G_h is the anode conductance after healing, and G_0 is the initial anode conductance. The initial conductance of the Si anodes varied from $1.4 – 2.0 \times 10^{-5}\ \Omega^{-1}$. Microcapsules with different core materials and different sizes were tested and the conductance restoration results are presented in **Figure 3.5**.

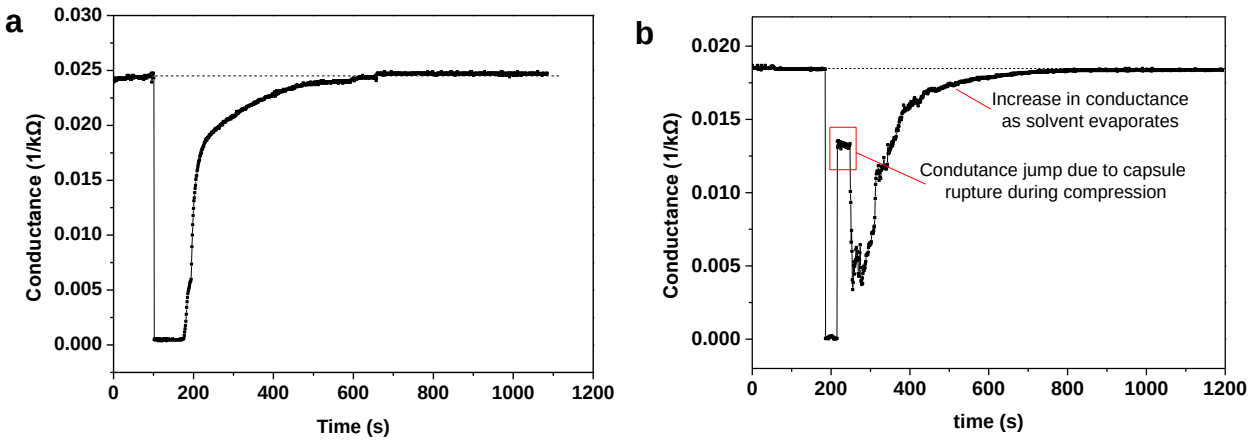


Figure 3.4. Representative conductance restoration vs. time curves. a) Deposition of 1 mg of core material (0.20 g/mL FCB1 and 0.01 g/mL P3HT) onto a line crack. b) Rupture of 1 mg of FCB1H/P3HT microcapsules (avg. diameter 300 μm) onto a line crack.

For the microcapsules containing FCB1 and 0.33 g/mL DGEBA (Figure 3.5a), we obtained a maximum restoration efficiency of 77 ± 12 % using microcapsules 300 μm in diameter with 0.2 g/mL FCB1. The FCB1 loading and capsule size greatly influenced the restoration efficiency. Higher FCB1 loading and larger capsule diameters led to higher conductance restoration efficiency due to increased delivery of carbon black to the damaged region. The direct deposition of core solution on line cracks yielded 100 % conductance restoration for all three FCB1 loadings. In contrast, control experiments with solvent only microcapsules produced no healing due to the absence of conductive particles.

When P3HT was used as core thickener instead of DGEBA in FCB1 microcapsules, the conductance restoration efficiency increased to greater than 85 % for all tests (**Figure 3.5**b). Full conductance recovery was achieved in microcapsules with 0.2 g/mL FCB1 for capsule diameters of 150 μm and above. The improved performance is attributed to the lower concentration of P3HT (0.01 g/mL) compared to DGEBA (0.33 g/mL) in the core solution and the attendant higher concentration of FCB1 particles for capsules with P3HT. The restoration efficiency for P3HT

capsules also showed less dependence on capsule size. The capsules containing commercial P3HT showed similar conductance restoration efficiency for all the given sizes.

The highest level of conductance restoration was achieved with FCB2 microcapsules containing P3HT core thickener (**Figure 3.5**c). Restoration efficiencies in the range of 95 - 100 % were achieved for all capsule diameters. The high octadecyl surface coverage for FCB2 facilitates better release upon capsule rupture, delivering more particles to the site of damage and leading to full recovery of anode conductance.

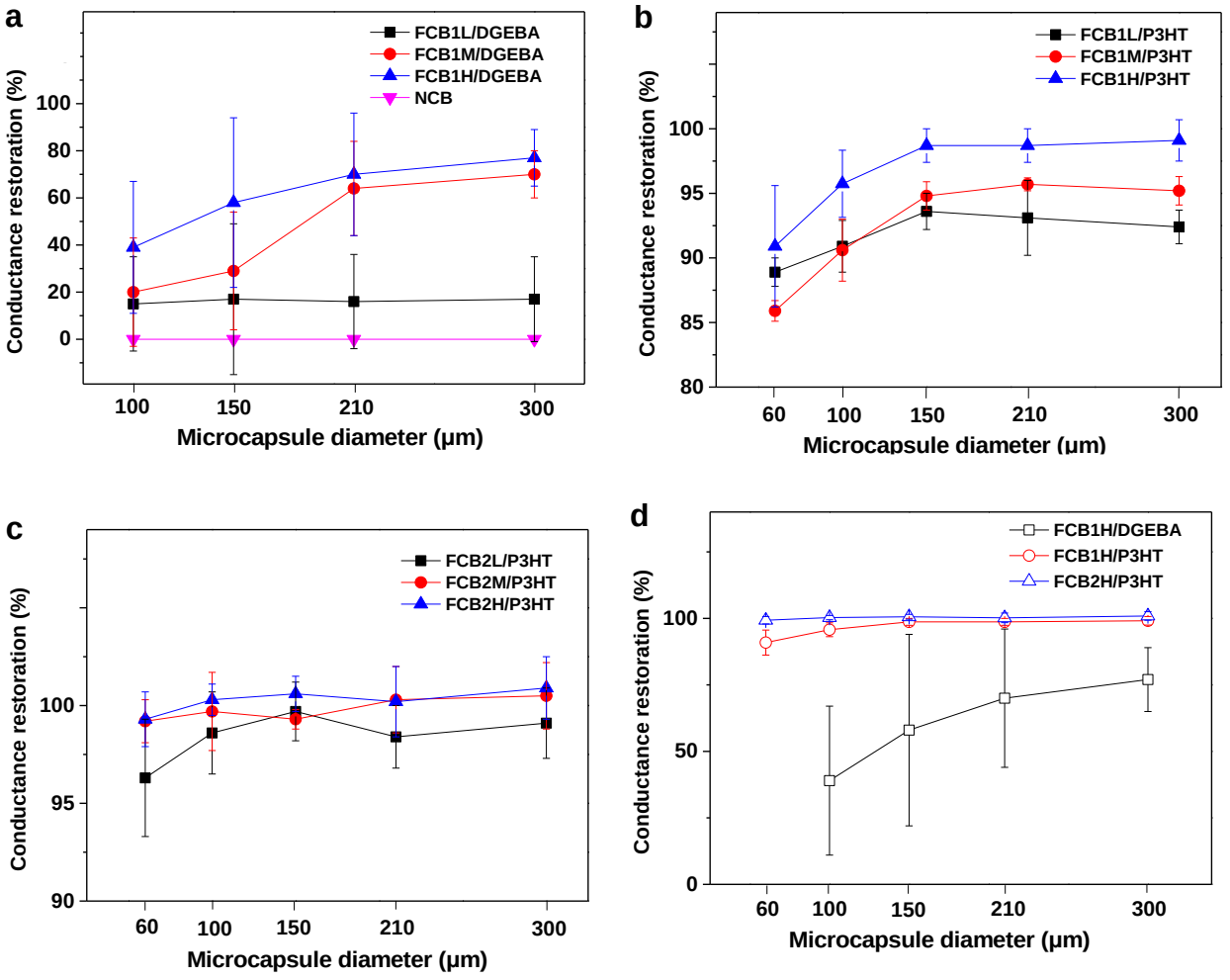


Figure 3.5. Conductance restoration of nanoparticle Si anodes for a) FCB1/DGEBA, b) FCB1/P3HT, and c) FCB2/P3HT filled microcapsules with different microcapsule sizes and carbon black loadings. d) Conductance restoration for microcapsules containing the highest FCB loading.

3.3.2 Conductivity Restoration of Electric Circuit

Four point bending (4PB) test was used to introduce damage to a multilayer specimen containing a conductive Au film. During the fracture of the specimen, the crack initiated at the notch of the glass layer, propagated through the epoxy layer, and deviated at the acrylic layer, resulting in delamination at epoxy/acrylic interface. The fracture also led to complete damage of Au film and rupture of FCB1 microcapsules. The crack opening width was ca. 3 μm, much smaller than the microcapsule sizes (> 125 μm). This small opening enabled the bridging of released FCB1 across the two sides of the gap. **Figure 3.6** contains a cross-sectional SEM image of the fracture surface. The capsules were all ruptured by the fracture event. The released FCB1 particles formed a particulate film on the epoxy layer and part of the glass layer, as indicated in **Figure 3.6**b and **3.6**c. The Au film at the epoxy/glass interface was also covered by FCB1.

The conductance restoration was evaluated by the change of normalized efficiency and conductance over time (**Figure 3.7**). The conductance of Au film prior to fracture was ca. 0.04 Ω^{-1}. Fracture of the specimen resulted in complete loss of conductivity of the Au film. The release of FCB1 particles from capsules led to a monotonic increase of conductance with time as the *o*-DCB solvent evaporated. The time needed for the completion of healing was > 50 h, much longer than the cases shown in the Si anode healing. This long healing time is due to the slow evaporation of *o*-DCB from the closed crack in 4PB specimen. The conductance after healing was ca. 3×10^{-4} Ω^{-1} (3 k Ω). The conductance recovery was low due to the low conductivity of carbon black as compared to gold and large contact resistance among FCB1 nanoparticles.

Table 3.1 summarized the healed conductance values of the Au film for different capsule sizes. Higher conductance was achieved with small diameter (180-125 μm) capsules than with larger capsules (250-180 μm). We hypothesize that decreasing capsule size increases the

probability for the propagating crack to intersect and rupture a capsule.[6] For the same capsule loading, the number of ruptured small capsules across the fracture plane was greater than the number of the large capsules, resulting in increased delivery of FCB1 particles and higher conductance after healing.

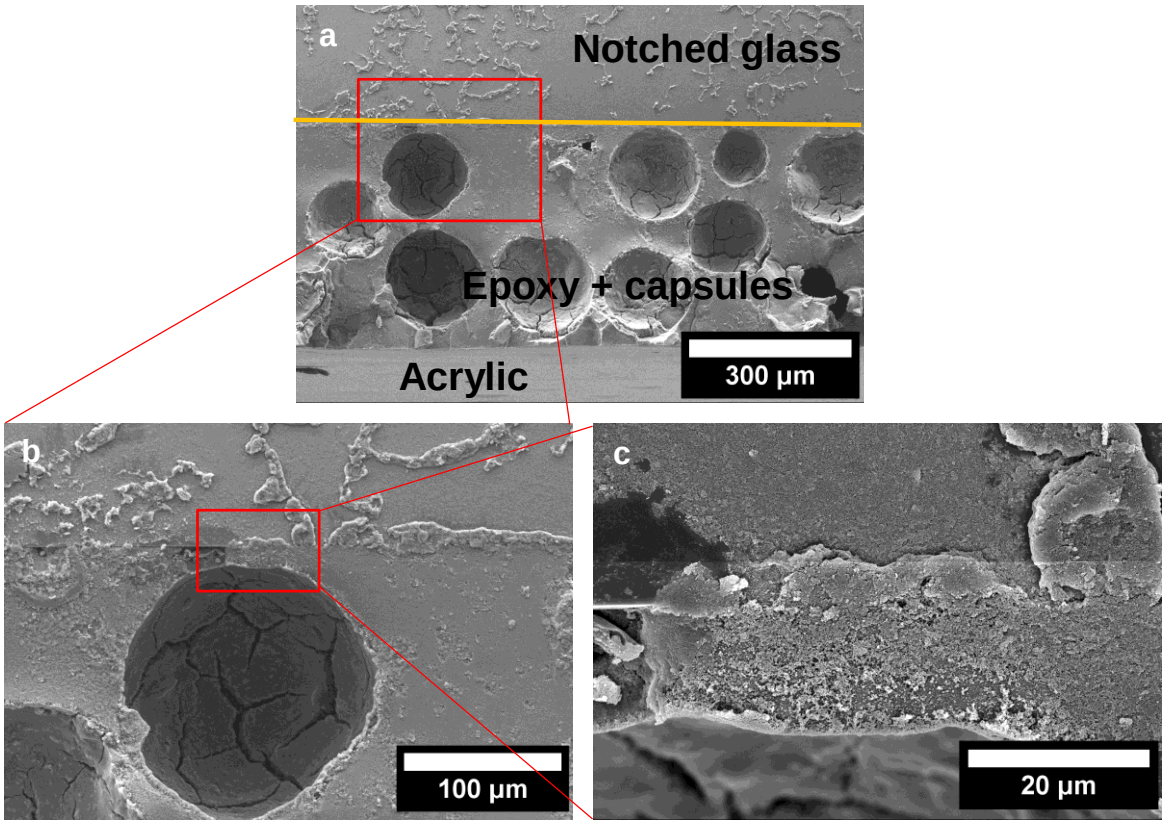


Figure 3.6. Cross-sectional SEM images of the fracture plane showing the release of FCB from microcapsules with different magnifications. The region of Au film in (a) is false colored.

Table 3.1. Conductance of Au film after healing using capsules with different sizes. 18 samples were tested for each size range.

Capsule diameter (μm)	180-250	125-180
Conductance (Ω^{-1})	$(3.18 \pm 1.76) \times 10^{-4}$	$(6.71 \pm 3.88) \times 10^{-4}$

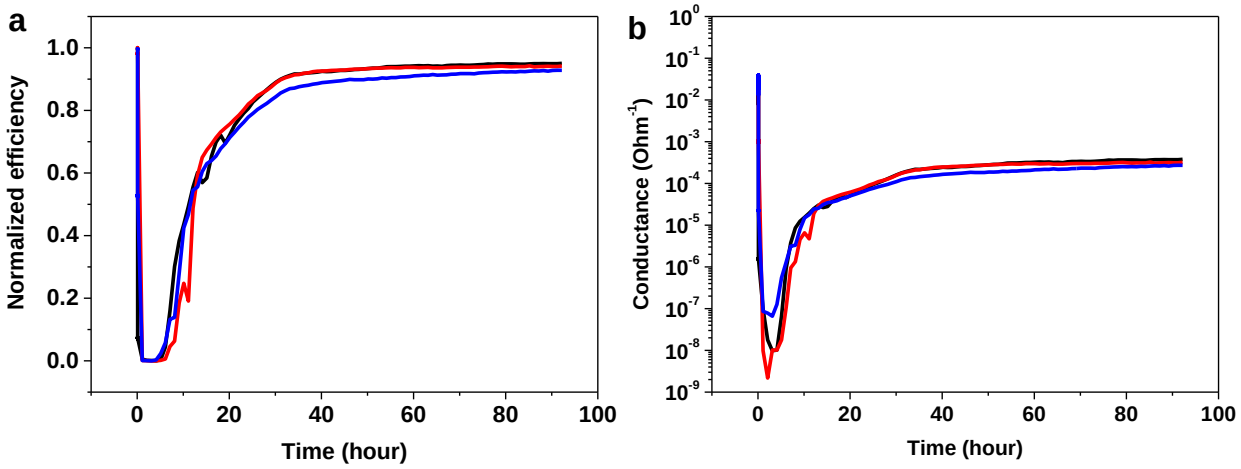


Figure 3.7. Representative conductance restoration as a function of time describing a) normalized efficiency and b) conductance change over time. The three lines with different colors represent the results from three individual Au films tested under the same condition. Capsule diameter in this study was 180-250 μm.

3.4 Conclusions

Ex situ conductivity restoration of damaged Si anodes and electric circuits was demonstrated by the release of FCB from microcapsules. A fiber removal method was developed to introduce ca. 10 μm wide line crack on Si composite anodes, causing the complete loss of conductivity. The rupture of FCB microcapsules and release of FCB particles on the crack region resulted in full recovery of Si anode conductivity within 20 min. A 4PB test protocol was used to create a circuit failure with ca. 3 μm wide crack. The release of FCB particles was observed at the fracture plane with a moderate restoration of circuit conductivity.

3.5 References

[1] P. F. Ribeiro, B. K. Johnson, M. L. Crow, A. Arsoy, Y. Liu, *Proceedings of the IEEE*, **2001**, *89*, 1744.

[2] K. C. Divya, J. Østergaard, *Electric Power Systems Research*, **2009**, *79*, 511.

[3] M. M. Caruso, S. R. Schelkopf, A. C. Jackson, A. M. Landry, P. V. Braun, J. S. Moore, *Journal of Materials Chemistry*, **2009**, *19*, 6093.

[4] S. A. Odom, T. P. Tyler, M. M. Caruso, J. A. Ritchey, M. V. Schulmerich, S. J. Robinson, R. Bhargava, N. R. Sottos, S. R. White, M. C. Hersam, J. S. Moore, *Applied Physics Letters*, **2012**, *101*.

[5] S. A. Odom, M. M. Caruso, A. D. Finke, A. M. Prokup, J. A. Ritchey, J. H. Leonard, S. R. White, N. R. Sottos, J. S. Moore, *Advanced Functional Materials*, **2010**, *20*, 1721.

[6] B. J. Blaiszik, S. L. B. Kramer, M. E. Grady, D. A. McIlroy, J. S. Moore, N. R. Sottos, S. R. White, *Advanced Materials*, **2012**, *24*, 398.

[7] N. Ding, J. Xu, Y. Yao, G. Wegner, I. Lieberwirth, C. Chen, *Journal of Power Sources*, **2009**, *192*, 644.

CHAPTER 4

MICROCAPSULE STABILITY IN BATTERY ENVIRONMENT[‡]

4.1 Introduction

Microcapsules containing functional core contents are used in a wide range of applications including self-healing materials, drug delivery, food additives, and paints.[1-3] Upon exposure to external stimuli, the microcapsule shell wall ruptures or disintegrates and the core content is delivered to fulfill a specific function.[4, 5] For many applications the microcapsule must remain stable for an extended period of time before delivering its payload.[6] Any loss of core prior to stimuli exposure, during storage, manufacturing, or service, will lead to reduced function of encapsulated systems.[7]

Harsh environments, such as elevated temperature or strong solvents, can degrade the microcapsule shell wall and accelerate diffusion of the core through the shell wall due to the chemical gradients. In self-healing polymers, high processing temperatures (> 100 ^{o}C) can cause core diffusion to the host matrix, reducing self-healing capability.[8] Additionally, wet processing in polymeric composite fabrication often involves strong solvents that can degrade the capsule shell wall.[9] As the goal of this thesis research is to use microcapsules to construct self-healing LIB batteries, it is critical that the microcapsules have long term stability in battery environment, which involves both solvents and high temperature.

Several methods have been developed to enhance capsule stability. Li et al. introduced double layered core-shell microcapsules by condensing urea-formaldehyde (UF) resin on as-prepared polyurethane (PU) microcapsule surfaces.[10] Subsequently, Caruso et al. developed an

[‡] Part of the content in this chapter is submitted to *ACS Applied Materials & Interfaces*: S. Kang, M. Baginska, S. R. White, N. R. Sottos, Core-Shell Polymeric Microcapsules with Superior Thermal and Solvent Stability.

improved single-batch process to prepare PU/UF double layered microcapsules.[11] The microcapsules showed moderate core loss at elevated temperature (ca. 10 wt% loss at 180 ^{o}C for 2 h). Jackson et al. reported a technique to coat a 20-40 nm thick silica layer on microcapsule surfaces for improved environmental stability.[12]

In this chapter, we report on the ability of a polydopamine (PDA) coating to protect microcapsules and improve capsule stability in battery environment. Inspired by the adhesive proteins in mussels where the coexistence of catechol and amine groups are crucial for strong adhesion properties, dopamine is a powerful building block that contains both catechol and amine moieties. As a result, the polymeric form of dopamine, PDA, shows strong adhesion on virtually all types of surfaces.[13, 14] Under basic conditions, dopamine immediately undergoes polymerization and deposits on the target surface as PDA.[15] Though the detailed structure of PDA remains elusive, recent investigations have shown that hydrogen bonding and π-π stacking make PDA a dense membrane with remarkable stability.[16]

4.2 Experimental

4.2.1 Materials

Urea, ammonium chloride, resorcinol, formalin solution (37 w/v %), *o*-dichlorobenzene (*o*-DCB), ammonium persulfate, dopamine hydrochloride, sodium phosphate monobasic monohydrate, sodium citrate dihydrate, tris (hydroxymethyl) aminomethane (TRIS), sodium hydroxide were used as received from Sigma Aldrich. The commercial polyurethane (PU) prepolymer, Desmodur L75, was obtained from Bayer Material Science and used as received. Ethylene-maleic anhydride (EMA) copolymer (Zemac-400) powder (Mw ca. 400 kDa) was from Vertellus and used as a 1.25 wt % aqueous solution. Battery electrolyte contains 1 M $LiClO_4$ in ethylene carbonate/dimethyl carbonate (1:3 in volume).

4.2.2 Preparation of Microcapsules

The encapsulation procedure was described in Chapter 2. Urea (0.90 g), ammonium chloride (0.20 g), and resorcinol (0.09 g) were dissolved in 1.25 wt % EMA aqueous solution (60 mL). Capsule core (10 mL) that contains Desmodur L75 (0.33 g) was subsequently added into the aqueous phase. A fine emulsion was formed after 3 min of homogenization (Omni GLH) of the mixture. The emulsion was mechanically stirred at 800 rpm. After adding formalin solution (2.4 g), the emulsion was heated up to 55 ^{o}C and allowed to react for 4 h. Microcapsules were separated by centrifugation and then washed with water 3 times to remove the residual surfactant and unencapsulated shell wall particles. Free flowing microcapsules were obtained by freeze drying.

4.2.3 PDA Coating of Microcapsules

In the first approach, microcapsules (0.2 g) were pre-dispersed in pH 8.4 buffer solution (10 mL). Dopamine hydrochloride (0.04 g) was then added into the solution under agitation. The solution turned brown within 20 min, indicating the polymerization of dopamine. After 1 day, the coated microcapsules were centrifuged, rinsed with water 3 times, and freeze dried to get free flowing powder. The pH 8.4 buffer contained 1 M TRIS in deionized water. HCl was used to adjust the pH to 8.4.

In the second approach, microcapsules (0.20 g) were pre-dispersed in pH 7.0 buffer solution (10 mL). Dopamine (0.04 g) and ammonium persulfate (0.04 g) were then added into the stirring solution. After 1 day, the microcapsules were collected using the same procedure as described above. The pH 7.0 buffer solution contained 1 M sodium phosphate monobasic monohydrate and 1 M sodium citrate dihydrate. NaOH was used to adjust the pH to 7.0.

Similarly, PDA polymer was made by adding dopamine (0.04 g) and ammonium persulfate (0.04 g) into pH 7.0 buffer solution (10 mL) and reacting for 1 day. PDA was centrifuged, rinsed with water 3 times, and dried under vacuum.

4.2.4 Characterization of Microcapsules

Microcapsule morphology was studied using SEM (Hitachi 4800) and TEM (Philips CM200). For SEM characterization, the microcapsules were placed on conductive carbon tape and sputter coated Au/Pd prior to imaging. For the observation of microcapsule shell wall, dried microcapsules were dispersed in epoxy resin (EPON 828 and 12 wt % DETA). After the epoxy resin was fully cured, the sample was microtomed to expose the shell wall of ruptured microcapsules. TEM was used to characterize the microcapsule shell wall.

The microcapsule shell wall components before and after PDA coating were characterized by Fourier Transform Infrared Spectroscopy (Thermo Nicolet NEXUS 670 FTIR). The microcapsules were ground with mortar and pestle to allow the release and evaporation of core liquid. Pellet samples were made with potassium bromide and stored under vacuum prior to testing in order to eliminate moisture.

Thermal analysis of microcapsules was performed on a Mettler-Toledo TGA 851. For the dynamic experiments, the microcapsules were heated from 25 to 600 ^{o}C, with 10 ^{o}C/min heating rate, under nitrogen atmosphere. For the isothermal studies, the microcapsules were heated up from 25 to 180 ^{o}C (10 ^{o}C/min heating rate) and then held at 180 ^{o}C for 3 h. The mass change was recorded throughout the entire experiment.

Solvent stability of microcapsules was studied both optically and quantitatively using ^{1}H-NMR. For optical observation, uncoated and PDA coated microcapsules were added to the desired solvents (5 wt% in water, pH 4 buffer solution, pH 10 buffer solution, acetone, ethyl acetate, and

chloroform). After 3 days, an aliquot was taken and the morphology of microcapsules was observed under an optical microscope (Leica DMR Optical Microscope). In the cases of acetone, ethyl acetate, and chloroform, the images showed the dried microcapsules. In water, pH 4 and pH 10 buffer solutions, the images showed the dispersed microcapsules in aqueous media.

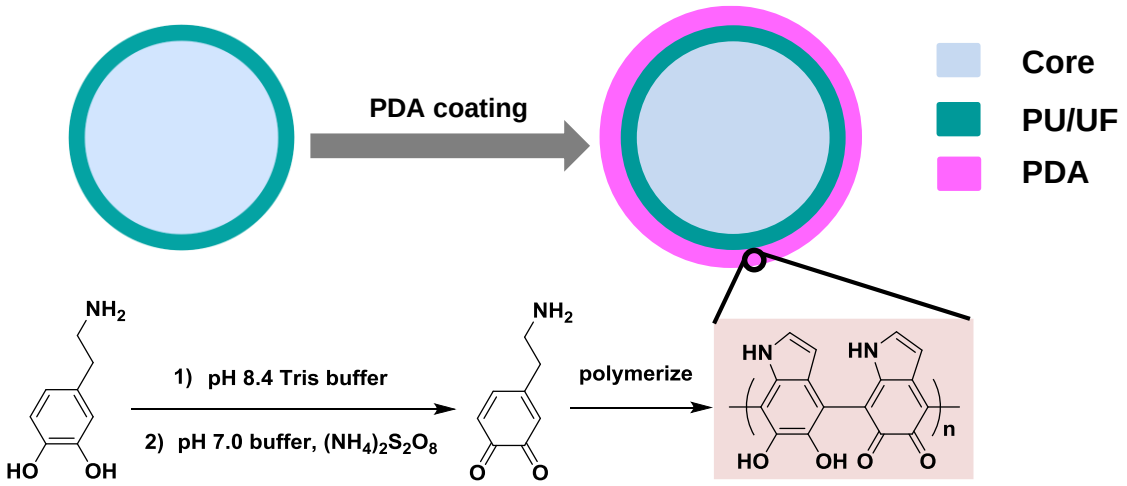
^{1}H-NMR method was used to quantify the percent core release of microcapsules in several solvents (acetone, ethyl acetate, chloroform, and battery electrolyte). Microcapsules (50 mg) were added to the desired solvent (1 g). After 3 days, hexyl acetate (20 mg) was added to the suspension as an internal standard. Subsequently, an aliquot was taken and filtered to remove the microcapsules. The filtered clear liquid was diluted by *d*-chloroform for ^{1}H-NMR measurement. The mass of released *o*-DCB in the solvents was calculated based on the integrated peak ratios of *o*-DCB and hexyl acetate in ^{1}H-NMR spectra. The percent core release was determined by the mass of released *o*-DCB divided by the mass of *o*-DCB in microcapsule core prior to immersion to the solvents. The percent core release of microcapsules in battery electrolyte was measured using the same method.

4.3 Results and Discussion

4.3.1 PDA Coating on Microcapsules

Microcapsules containing *o*-DCB only (no carbon black) and microcapsules containing FCB suspensions were prepared by a combined *in-situ*/interfacial emulsion technique. Two coating conditions with different solution pH values were used to form PDA coatings on microcapsule surfaces (**Scheme 4.1**). PDA is commonly prepared by the polymerization of dopamine hydrochloride in TRIS buffer solution at pH 8.4.[15] The catechol moieties in dopamine are oxidized to quinine and subsequently undergo polymerization to form PDA, accompanied by the color change from transparent to dark brown within 20 min. In the first approach, PDA was

coated on microcapsule surfaces in an aqueous solution at pH 8.4. In the second approach, the PDA coating was formed in a neutral aqueous solution at pH 7.0. Although the polymerization of dopamine does not typically occur in neutral pH, here we added ammonium persulfate to oxidize the catechol to quinine and initiate the polymerization.[17]



Scheme 4.1. Polymerization of dopamine and deposition of PDA on core-shell microcapsule surfaces under two different conditions: 1) pH 8.4 TRIS buffer solution; 2) pH 7.0 buffer solution with the presence of ammonium persulfate.

The deposition of PDA on capsule surfaces is evident from the SEM and TEM images in **Figure 4.1**. In contrast to the smooth surface morphology of uncoated microcapsules (**Figure 4.1**a), PDA coated microcapsules have enhanced surface roughness, indicating the deposition of PDA. The microcapsules prepared in basic solution (pH 8.4) have an irregular shape and poor shell wall integrity. In great contrast, the microcapsules prepared with pH 7.0 buffer solution retained their spherical shape and uniform thickness. The PDA coating was ca. 50 nm thick, similar to the thickness of the inner PU/UF layer. Only the PDA coated microcapsules prepared under neutral condition were subject to further characterization studies.

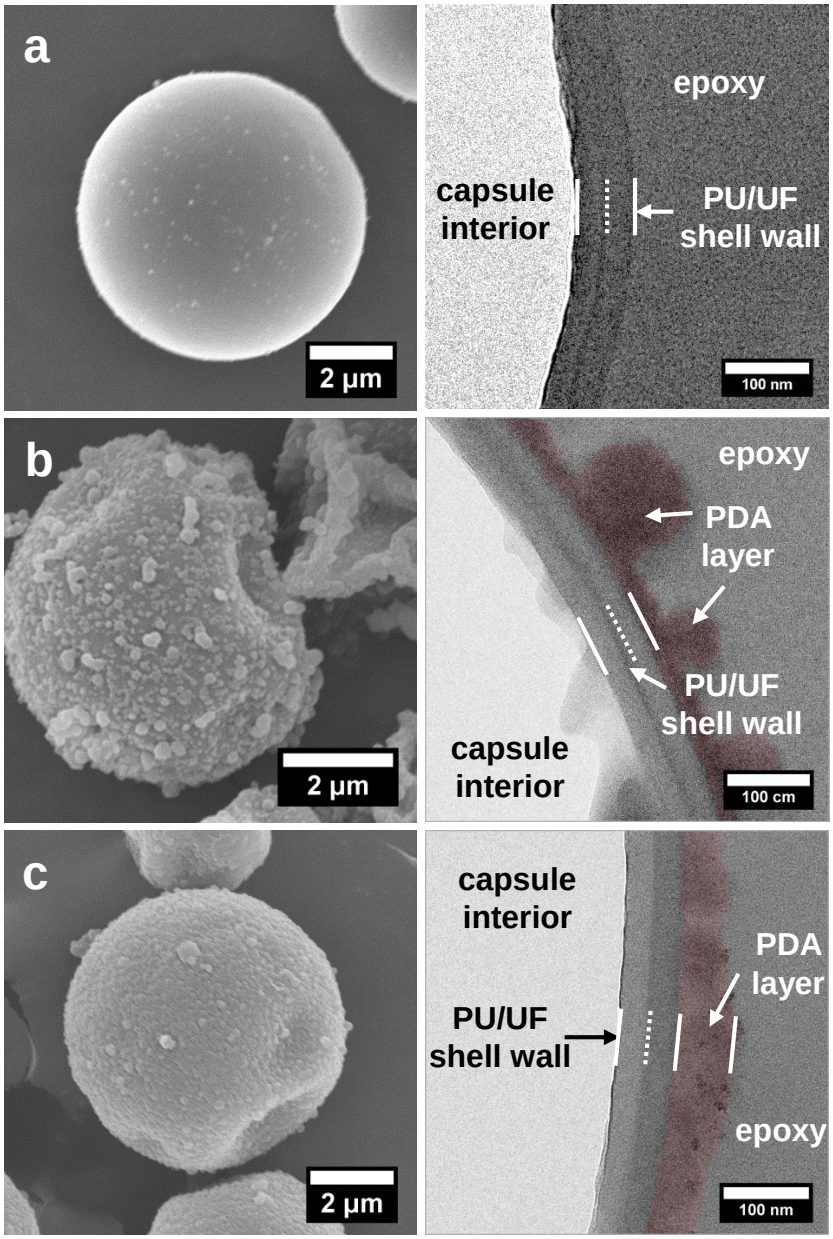


Figure 4.1. Microcapsule morphology and shell wall cross-section for different processing conditions. a) SEM and TEM of cross-section of uncoated PU/UF microcapsule. b) SEM and TEM of cross-section of PDA coated microcapsule prepared in pH 8.4 solution. c) SEM and TEM of cross-section of PDA coated microcapsule prepared in pH 7.0 solution.

The PDA coating on microcapsules was confirmed by FT-IR measurements (**Figure 4.2**). The FI-IR spectrum of the PDA coated microcapsule shell wall showed the characteristic absorbance peaks of both PU/UF and PDA polymers. The absorbance peaks of PU/UF/PDA from

1800 to 1400 cm^{-1} are the superposition of the absorbance peaks of PU/UF at 1723, 1653, 1543 cm^{-1}, and 1231 cm^{-1} (C=O stretching from urethane, C=O stretching from urea, N-H scissoring, and C-O stretching, respectively) and the absorbance peaks of PDA at 1510, 1600 cm^{-1}, and 1274 cm^{-1} (N-H scissoring, C=C stretching from the indole ring, and C-O stretching from phenolic moieties, respectively).[18, 19] The broad peak of PU/UF/PDA from 2700 to 3700 cm^{-1} is an overlap of the peaks from PU/UF (O-H stretching, N-H stretching, aromatic and aliphatic C-H stretching) and PDA (hydrogen bonding, O-H stretching, N-H stretching, aromatic and aliphatic C-H stretching) spectra.

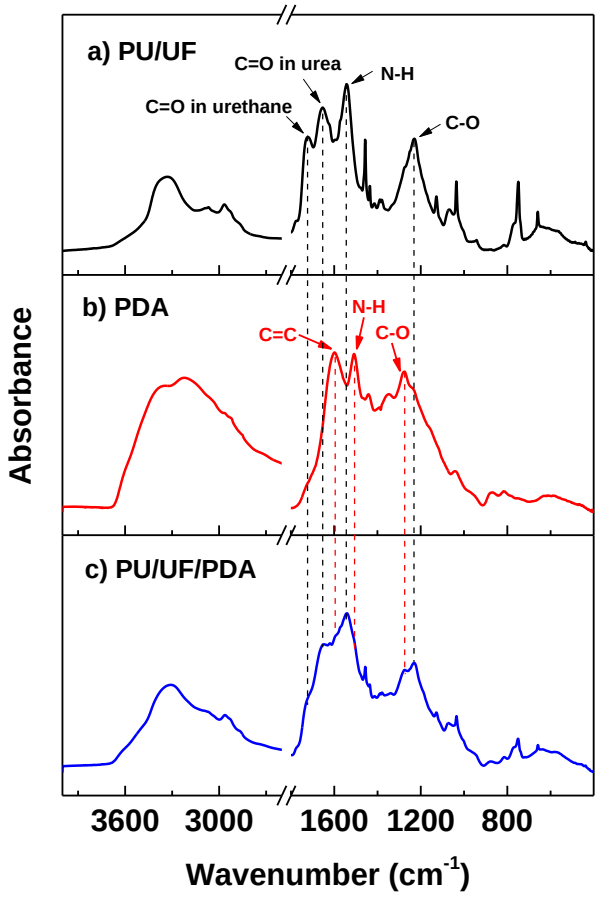


Figure 4.2. Comparison of FTIR spectra of shell wall materials. a) PU/UF from ground uncoated microcapsules, b) PDA synthesized in pH 7.0 buffer solution, and c) PU/UF/PDA from ground PDA coated microcapsules. The absorbance peaks in c) PU/UF/PDA are indicated by the vertical black and red dotted lines corresponding to the absorbance peaks in a) PU/UF and b) PDA.

4.3.2 Thermal Stability of Microcapsules

The thermal stability of microcapsules was evaluated by thermal gravimetric analysis (TGA) under dynamic and isothermal conditions. In the dynamic experiment (**Figure 4.3**a), weight loss of uncoated microcapsules initiated at 225 °C due to the rupture of the shell wall and evaporation of *o*-DCB core. For PDA coated microcapsules, the onset weight loss temperature increased by ca. 20 °C to 245 °C. Above 200 °C, *o*-DCB (b.p. 180 °C) is volatile. We hypothesized that the PDA shell wall was able to hold a higher vapor pressure of *o*-DCB than the PU/UF shell wall, postponing the microcapsule rupture temperature by 20 °C. At 600 °C, we observed ca. 10 wt% residue mass for PDA coated microcapsules in contrast to the complete decomposition of uncoated PU/UF capsules. The residue mass was from PDA coating as plain PDA polymer remained ca. 60 wt% at 600 °C (**Figure 4.4**a). Thermal stability was further studied by isothermal TGA of microcapsules at 180 °C for 3 h (**Figure 4.3**b). The weight loss for uncoated microcapsules was 94.4 wt% at 180 °C, leaving only the microcapsule shell wall. The PDA coated microcapsules only lost 3.7 % in weight, showing good core retention ability at high temperature.

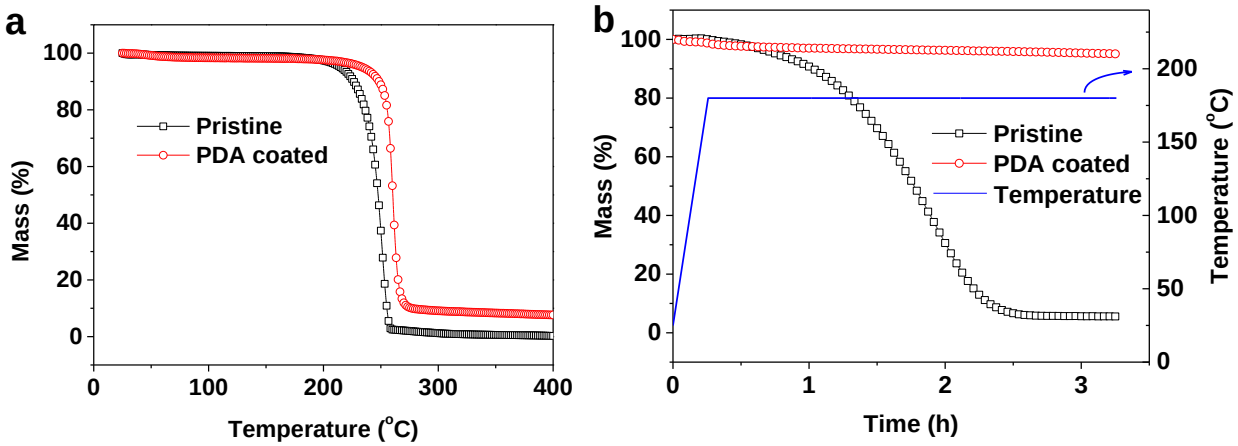


Figure 4.3. Thermal stability of uncoated and PDA coated microcapsules. TGA at (a) dynamic condition (25-600 °C, 10 °C/min, mass loss shown till 400 °C on the plot) and (b) isothermal condition (180 °C, 3 hours), the blue line shows the temperature profile.

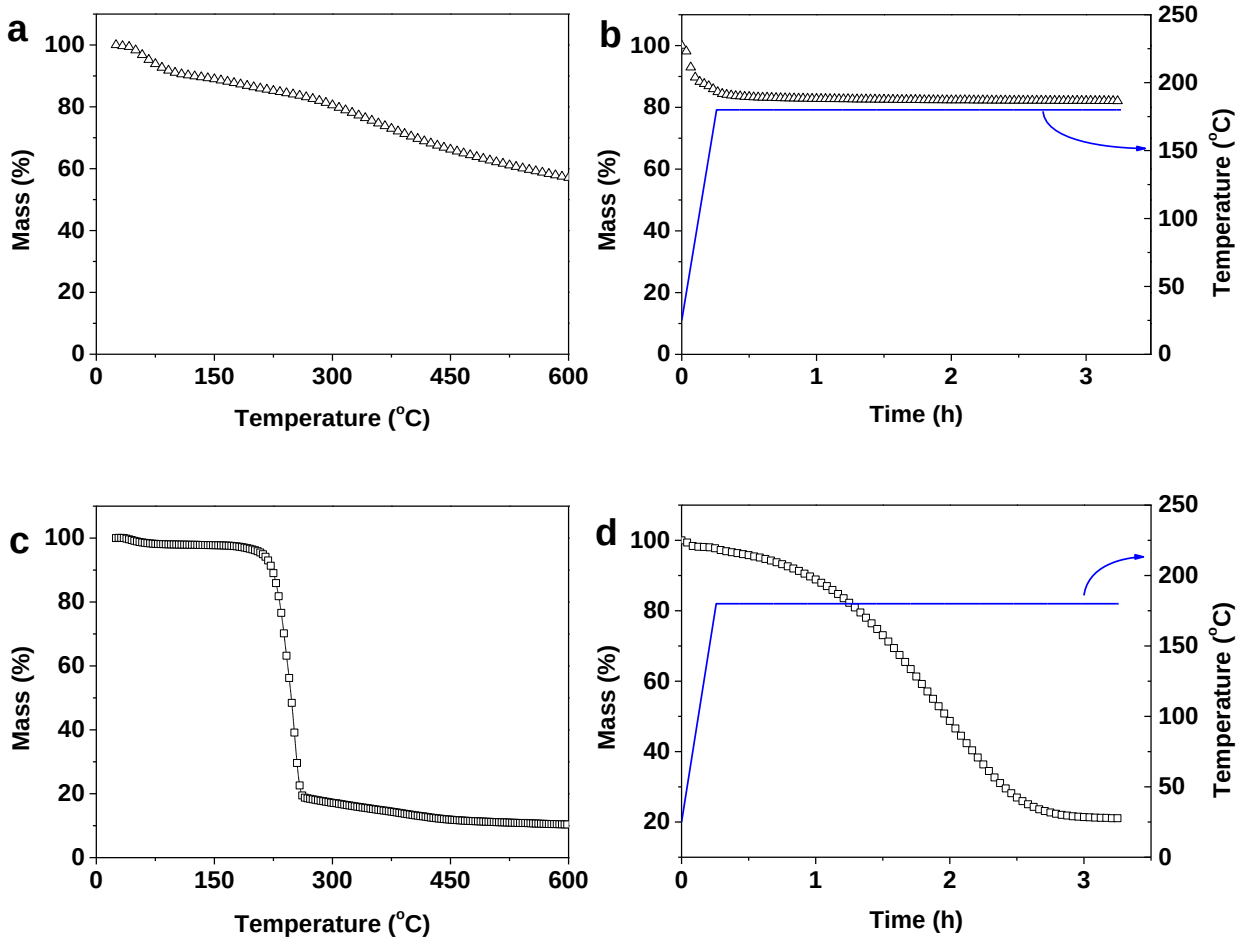


Figure 4.4. TGA of PDA polymer synthesized in pH 7.0 buffer solution at (a) dynamic condition (25-600 °C, 10 °C/min) and (b) isothermal condition (180 °C, 3 h). TGA of PDA coated capsules coated in pH 8.4 buffer solution at (c) dynamic condition (25-600 °C, 10 °C/min) and (d) isothermal condition (180 °C, 3 h).

4.3.3 Solvent Stability of Microcapsules

To evaluate the stability in solvents, we soaked the microcapsules in different organic solvents and aqueous solutions with different pHs at room temperature. Optical images of the microcapsules after 3 days of immersion were taken (**Figure 4.5**). In aqueous systems, both uncoated and PDA coated microcapsules showed good survival in acidic (pH 4.0) and neutral solution (pH 7.0). However, uncoated microcapsules deflated in pH 10 solution while PDA coated microcapsules still retained the majority of the core. In organic solvents (acetone, ethyl acetate,

and chloroform), uncoated microcapsules were not able to maintain the core and significant deflation and agglomeration were observed (**Figure 4.5**d-f). In contrast, the PDA coated microcapsules remained dispersed and spherical, suggesting good solvent stability.

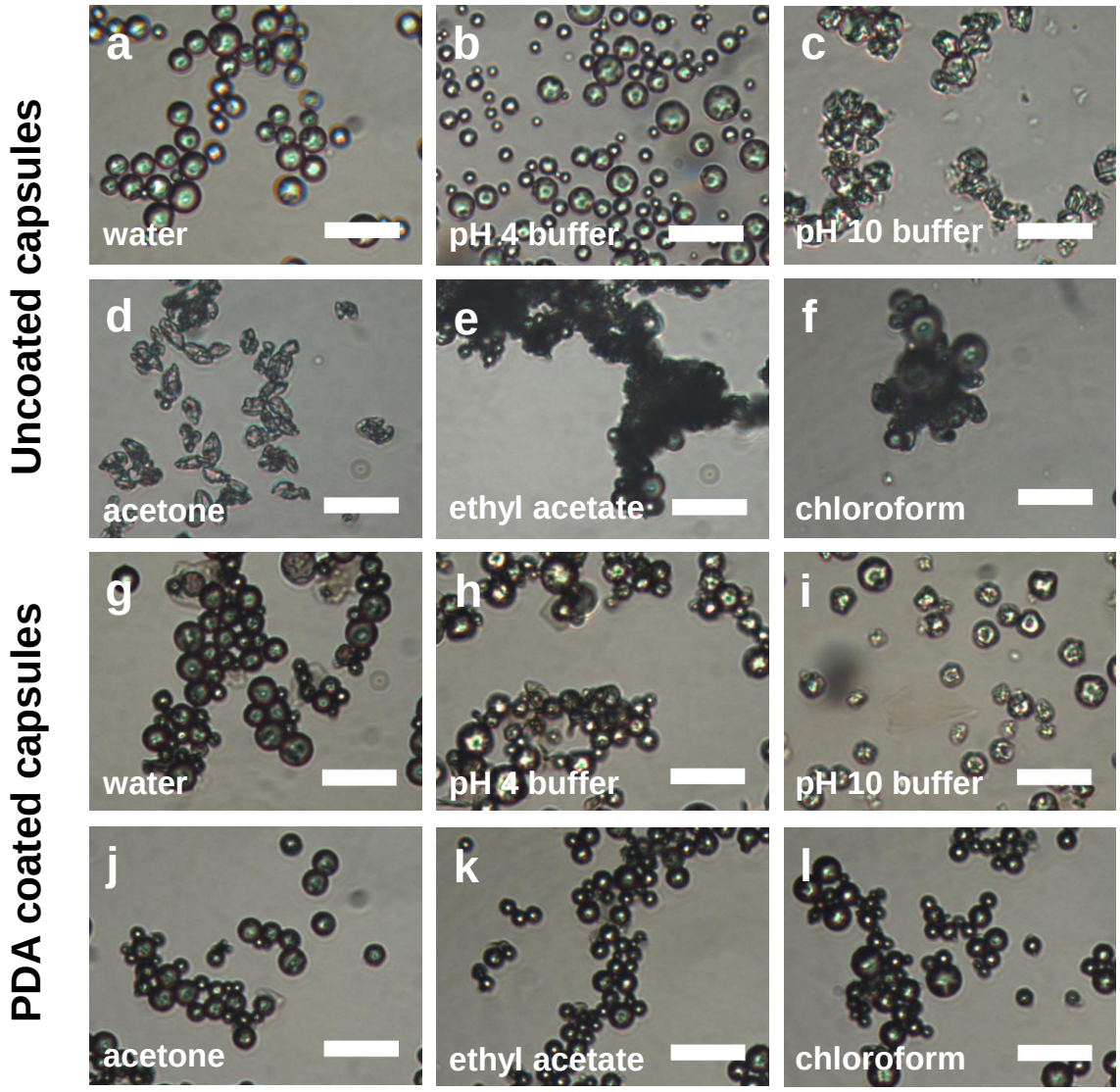


Figure 4.5. Microcapsule stability in various solvent conditions. Optical images taken after 3 days of immersion of (a-c) uncoated microcapsules and (g-i) PDA coated microcapsules in neutral (pH 7.0), acidic (pH 4.0), and basic (pH 10.0) buffer solutions, (d-f) uncoated microcapsules and (j-l) PDA coated microcapsules immersed in different solvents. The scale bar is 20 μm for all images.

The percent of core release from the microcapsules in different solvents after 3 days of immersion was quantified by ^{1}H-NMR (**Figure 4.6**). PDA coated capsules retained over 90 % of

the *o*-DCB core in acetone, ethyl acetate, and chloroform, while the uncoated capsules lost from 40 to 90 % of core content depending on the solvent.

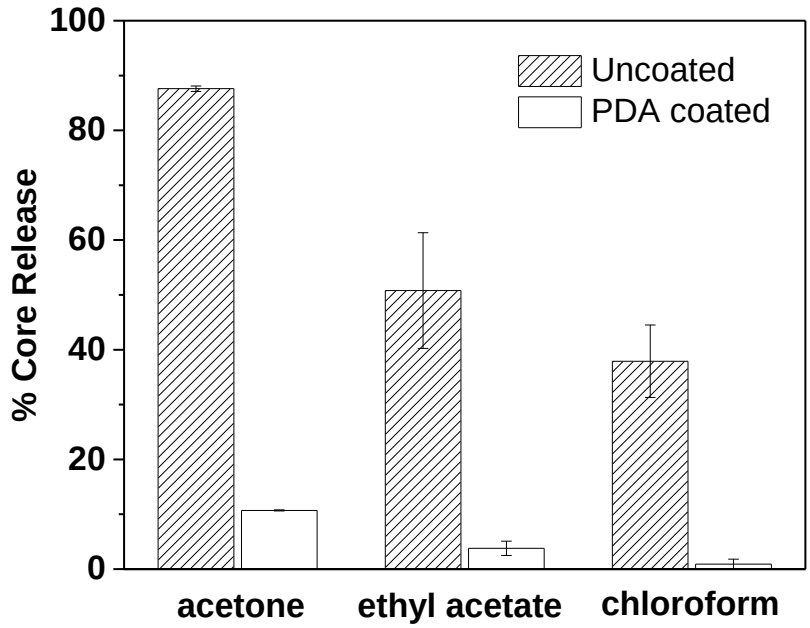


Figure 4.6. Weight percent of *o*-DCB release from microcapsules after 3 days of immersion in organic solvents measured by ^{1}H-NMR.

The percent of core release in battery electrolyte was also quantified using ^{1}H-NMR. The time release profile of microcapsule core was shown in **Figure 4.7**. For *o*-DCB microcapsules, the uncoated *o*-DCB microcapsules showed 12 % core release after 60 days of immersion in electrolyte. In great contrast, no core release was observed on the capsules with the PDA protective layer, showing superior stability in electrolyte. The uncoated capsules containing FCB suspensions (20 wt% FCB in *o*-DCB) showed much more core release (40 %) than the uncoated *o*-DCB microcapsules. During encapsulation, the movement of FCB particles interfered with the growth of capsule shell wall, resulting in decreased capsule shell wall quality. After PDA coating, the core release of FCB capsules decreased from 40 % to 12 % after 60 days, suggesting good stability in battery electrolyte environment.

The release profile showed a burst release of *o*-DCB within the initial several hours followed by a slow release over 60 days without reaching 100 % core release. This release behavior is different from traditional microencapsulated drug release (reaching 100 % core release over time) and cannot be explained by zero-order (constant release rate) or first-order (release rate proportional to the concentration) kinetics. Further investigation is needed to understand this multicomponent system.

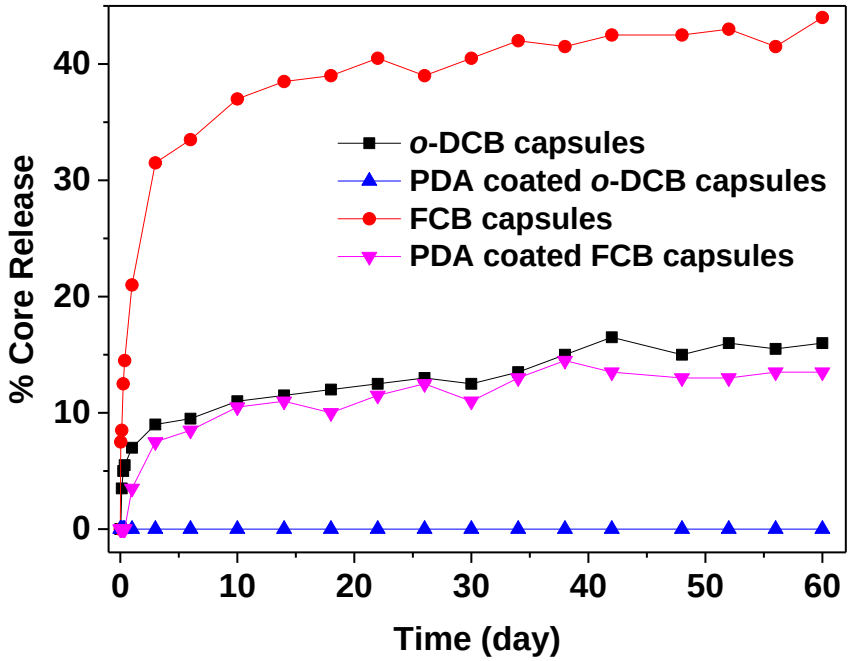


Figure 4.7. Weight percent of *o*-DCB release from microcapsules in battery electrolyte (1 M $LiClO_4$ in ethylene carbonate/dimethyl carbonate, 1:3 in volume) measured by ^{1}H-NMR. Two types of capsules were studied: *o*-DCB microcapsules and FCB suspension (20 wt% FCB in *o*-DCB) filled microcapsules.

4.4 Conclusions

Microcapsules with superior thermal and solvent stability were prepared by coating core-shell microcapsules with PDA polymer film. The PDA coating effectively limited the diffusion of core liquid through microcapsule shell wall at elevated temperature (180 ^{o}C). Reduced permeability of capsule shell wall was also observed in common organic solvents as well as in

basic aqueous solution. The PDA protective coating serves as an effective barrier for *o*-DCB core diffusion. The superior thermal and solvent stability of the PDA coated microcapsules make them promising candidates for self-healing battery application, and also for a variety of other applications where exceptional capsule stability is required.

4.5 References

[1] B. J. Blaiszik, S. L. B. Kramer, S. C. Olugebefola, J. S. Moore, N. R. Sottos, S. R. White, *Annual Review of Materials Research*, **2010**, *40*, 179.

[2] S. R. White, N. R. Sottos, P. H. Geubelle, J. S. Moore, M. R. Kessler, S. R. Sriram, E. N. Brown, S. Viswanathan, *Nature*, **2001**, *409*, 794.

[3] A. P. Esser-Kahn, S. A. Odom, N. R. Sottos, S. R. White, J. S. Moore, *Macromolecules*, **2011**, *44*, 5539.

[4] A. R. Jones, B. J. Blaiszik, S. R. White, N. R. Sottos, *Composites Science and Technology*, **2013**, *79*, 1.

[5] S. H. Cho, S. R. White, P. V. Braun, *Advanced Materials*, **2009**, *21*, 645.

[6] A. J. Patel, N. R. Sottos, E. D. Wetzel, S. R. White, *Composites Part A: Applied Science and Manufacturing*, **2010**, *41*, 360.

[7] H. Jin, C. L. Mangun, D. S. Stradley, J. S. Moore, N. R. Sottos, S. R. White, *Polymer*, **2012**, *53*, 581.

[8] H. Jin, C. L. Mangun, A. S. Griffin, J. S. Moore, N. R. Sottos, S. R. White, *Advanced Materials*, **2014**, *26*, 282.

[9] L. Yuan, A. Gu, G. Liang, *Materials Chemistry and Physics*, **2008**, *110*, 417.

[10] G. Li, Y. Feng, P. Gao, X. Li, *Polymer Bulletin*, **2008**, *60*, 725.

[11] M. M. Caruso, B. J. Blaiszik, H. Jin, S. R. Schelkopf, D. S. Stradley, N. R. Sottos, S. R. White, J. S. Moore, *ACS Applied Materials & Interfaces*, **2010**, *2*, 1195.

[12] A. C. Jackson, J. A. Bartelt, K. Marczewski, N. R. Sottos, P. V. Braun, *Macromolecular Rapid Communications*, **2011**, *32*, 82.

[13] H. Lee, S. M. Dellatore, W. M. Miller, P. B. Messersmith, *Science*, **2007**, *318*, 426.

[14] M. H. Ryou, J. Kim, I. Lee, S. Kim, Y. K. Jeong, S. Hong, J. H. Ryu, T. S. Kim, J. K. Park, H. Lee, J. W. Choi, *Advanced Materials*, **2013**, *25*, 1571.

[15] D. R. Dreyer, D. J. Miller, B. D. Freeman, D. R. Paul, C. W. Bielawski, *Chemical Science*, **2013**, *4*, 3796.

[16] D. R. Dreyer, D. J. Miller, B. D. Freeman, D. R. Paul, C. W. Bielawski, *Langmuir*, **2012**, *28*, 6428.

[17] Q. Wei, F. Zhang, J. Li, B. Li, C. Zhao, *Polymer Chemistry*, **2010**, *1*, 1430.

[18] R. Luo, L. Tang, J. Wang, Y. Zhao, Q. Tu, Y. Weng, R. Shen, N. Huang, *Colloids and Surfaces B: Biointerfaces*, **2013**, *106*, 66.

[19] M. Müller, B. Keßler, *Langmuir*, **2011**, *27*, 12499.

CHAPTER 5

Si COMPOSITE Li-ION BATTERY ANODES WITH DYNAMIC IONIC BONDING

5.1 Introduction

Lithium-ion batteries (LIB) have been widely used in portable electronic devices, electric vehicles, and grid-scale energy storage due to the high energy density, high power density, and high operating voltages.[1, 2] Graphite is the active material for most commercial anodes and has a capacity of 372 mAh/g. The growing need for anode materials with higher capacity has led to the investigation of silicon due to its extremely high gravimetric capacity (4200 mAh/g) and volumetric capacity (9786 mAh/cm^3).[3] However, Si undergoes huge volume change (> 400 %) upon lithium intercalation, resulting in the destruction of the conductive network, unstable solid electrolyte interface (SEI) layer on Si particle surfaces, and rapid capacity decrease. Materials strategies to overcome the large volume change and enhance capacity retention of Si anodes include the use of (1) Si particles dispersed in a rigid carbon matrix; (2) Si thin films; (3) nanostructured Si; and (4) Si composite anodes with polymer binders.[4] In this chapter, we explore the self-healing strategies for composite Si electrodes.

Although polyvinylidene fluoride (PVDF) is one of the most common binders in graphite composite electrodes, it interacts with Si particles via weak van der Waals interactions. In contrast, polymers containing carboxyl groups, such as carboxylmethyl cellulose (CMC), poly(acrylic acid), and alginate, form strong hydrogen bonds with the native silica layer on Si particle surfaces, resulting in much better capacity retention of the Si anodes.[5-7] Bridel et al. suggest that the hydrogen bonds undergo a self-healing process that is crucial for cycling stability of Si anodes.[8] Furthermore, Cui et al. recently incorporated a hydrogen bonding based self-healing polymer

binder in a composite electrode containing Si microparticles.[9] The self-healing composite anodes showed a cycle life of 130 cycles with 70 % capacity retention at a cycle rate of 0.42 A/g, which was attributed to the dynamic hydrogen bonding.

Other types of dynamic bonds such as metal-ligand coordination bonds, π-π stacking, and ionic bonds can impart self-healing properties to polymers.[10] Ionic bonding involves two oppositely charged ions and is weaker than covalent bonding and stronger than hydrogen bonding. A stretchable and tough hydrogel was developed by Suo et al.[11] by constructing alginate-polyacrylamide matrix with covalent crosslinks and ionic bond networks. The carboxylate/Ca^{2+} ionic bond unzipped upon stretching the film and re-zipped to heal the internal damage. Similarly, Wei et al. prepared self-healing hydrogels consisting of ferric ions and crosslinked poly(acrylic acid) (PAA).[12] The migration of Fe^{3+} in the hydrogel allowed the reformation of carboxylate/Fe^{3+} ionic bond at the cut interface. A self-healing anticorrosion coating was developed by Andreeva et al. via layer-by-layer deposition of polyelectrolytes (poly(ethyleneimine) as polycation and poly(styrene sulfonate) as polyanion) on Al substrate.[13] The mobility of the polymers led to the healing of a scratch and protected the substrate from corrosion. Lyon et al. described a self-healing hydrogel film containing multilayered polyanion microgel and polycation.[14] After damage, the solvation of the film in water permitted the reformation of the ionic bonds, resulting in fast recovery for multiple cycles.

Here we report a simple yet versatile approach to incorporate dynamic ionic bonds to Si composite anodes for autonomous healing of the electrical interfaces during anode operation. Ionic bonds were incorporated in Si anodes by mixing amine functionalized Si nanoparticles with poly(acrylic acid). The formation of ionic bonds was confirmed by X-ray photoelectron

spectroscopy and Raman spectroscopy. The Si anodes with self-healing ionic bonding showed excellent cycle life and rate capability.

5.2 Experimental

5.2.1 Materials

Trimethoxymethylsilane (TMS), (3-aminopropyl)trimethoxysilane (APS), sodium carboxymethyl cellulose (CMC-Na, average M_w ca. 700,000), poly(acrylic acid) (PAA, average M_w ~1,250,000), ninhydrin, and sodium hydroxide were used as received from Sigma Aldrich. Silicon nanoparticles (99 %, 100 nm, plasma synthesized) were purchased from MTI Corporation. Battery electrolyte containing 1 M lithium hexafluorophosphate ($LiPF_6$) in a mixture of ethylene carbonate (EC) and dimethyl carbonate (DMC) (1:1 by volume) was purchased from BASF. Carbon black (Regal 400R) was obtained from Cabot Corporation. Fluoroethylene carbonate (FEC) and lithium metal (0.75 mm in thickness) were purchased from Alfa Aesar. The battery separator film was a trilayer polypropylene-polyethylene-polypropylene membrane made by Celgard and was purchased from MTI Corporation.

5.2.2 Surface Functionalization of Si Particles and Quantification of Amine Functionalities

The silicon nanoparticles (1.0 g) were pre-dispersed in ethanol (60 mL). An appropriate amount of APS was then added into the stirring suspension. After 2 days, the amine functionalized silicon particles were centrifuged, rinsed with ethanol for 3 times, and vacuum dried. Silica nanoparticles were also functionalized with amine following the same procedure for Raman and XPS characterization. Trimethoxymethylsilane was used to make methyl functionalized Si particles for control samples.

The coverage of amino groups on the surface of Si nanoparticles was quantified by a ninhydrin titration method.[15] Ninhydrin is known to react with amine to produce a purple color complex. The concentration of the complex (equal to the concentration of amino groups) is determined by measuring the UV-vis absorbance (@ 588 nm) of the reaction solution. The amine functionalized Si (0.02 g), denoted as Si-NH_2, was dispersed in ethanol (2.8 mL) and sonicated for 20 min. A ninhydrin solution (0.35 w/v % ninhydrin in ethanol, 1.0 mL) was then added to the suspension. After 10 min of sonication, the mixture was heated at 80 ^oC for 20 min. Upon cooling down, the mixture was centrifuged and the supernatant was collected for UV-vis (UV-2401 PC, Shimadzu, Japan) measurement. A linear calibration curve was created by measuring the UV-vis absorbance (@ 588 nm) of reaction solution of hexylmethylenediamine and ninhydrin with five known concentrations. The concentration of amino groups on Si-NH_2 was determined from the calibration curve.

5.2.3 Preparation of Si Anodes and Structural Characterization of Ionic Bonds

Si anodes were prepared with a weight ratio of 60:20:20 of Si nanoparticles, polymer binder, and carbon black. Two different binders were investigated: PAA and CMC-Na. The binder (30 mg) was dissolved in deionized water (3.0 g), and then Si (90 mg) and carbon black (30 mg) particles were added to the solution subsequently. The mixture was homogenized (OMNI GLH-01) for 1 h and magnetically stirred for 2 days. The slurry was cast on Cu foil (thickness ~ 8 μm) with a doctor blade and air dried.

X-ray Photoelectron Spectroscopy (XPS, Kratos Axis ULTRA) and Raman Spectroscopy (Horiba LabRAM HR 3D) were used to characterize ionic bond formation in Si anodes. Films with different compositions were made by casting the particle or particle/polymer suspensions onto plastic substrate followed by air drying.

5.2.4 Electrochemical Characterization of Si Anodes

The Si anodes were dried at 80 ^{o}C in argon atmosphere for 8 h and assembled into 2032 type stainless steel coin cells with Li metal as counter electrodes in Ar-filled glove box. The electrolyte contains 1 M $LiPF_6$ in EC/DMC with 10 wt% FEC.

The cells were electrochemically cycled between 0.01 and 1.0 V vs. Li/Li^+ at C/24 rate for the first formation cycle and different rates for the subsequent cycles using a battery test station (Arbin BT2000). Impedance was measured on a potentiostat system (Bio-Logic VSP) with a frequency range of 200 kHz to 0.1 Hz at 1 V with 10 mV amplitude. The cells were discharged at 1 V for 6 h prior to impedance measurement.

5.2.5 Characterization of Si Anodes

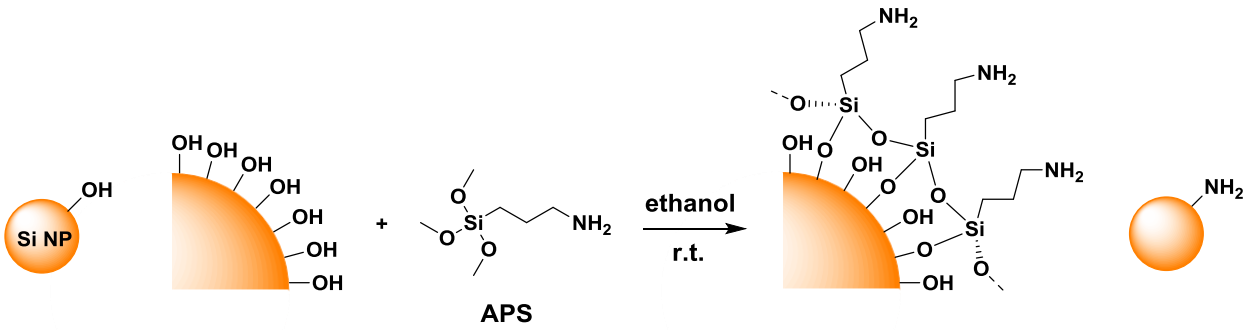
SEM (Hitachi 4800) and XPS were used to characterize the morphological and structural change of Si anodes upon cycling. The cycled coin cell was disassembled in argon atmosphere. The cycled anode was rinsed with DMC three times to remove residual electrolyte and dried in argon atmosphere prior to SEM and XPS characterization.

5.3 Results and Discussion

5.3.1 Surface Characterization of Si Nanoparticles and Composite Anodes

Functionalization of Si materials with amine groups has been widely reported.[16, 17] Si nanoparticles possess a thin native SiO_2 layer, which contains active hydroxyl groups that can react with (3-aminopropyl)trimethoxysilane (APS) to covalently bond the amino groups onto Si particle surface (**Scheme 5.1**). Different amounts of APS were added to the functionalization solution to systematically vary the amine coverage on Si particles. The resulting surface amine coverage is summarized in **Figure 5.1** for 5 different APS/Si weight ratios. Increasing the amount of APS from 1:100 to 1:10 tripled the amine coverage from ca. 0.016 mmol/g Si to ca. 0.05 mmol/g Si. Further

increase in the APS/Si ratio had no effect on the coverage. We hypothesized that at 1:10 APS/Si weight ratio, the Si surface was saturated with amino groups due to the steric effect which limited further growth of APS onto Si surfaces.



Scheme 5.1. Synthetic route for amine functionalized Si particles. APS was first hydrolyzed to produce silanol (Si-OH) groups, and then silanol groups condense with the hydroxyl groups on Si particles to form covalent Si-O-Si bonds by releasing H_2O molecules.

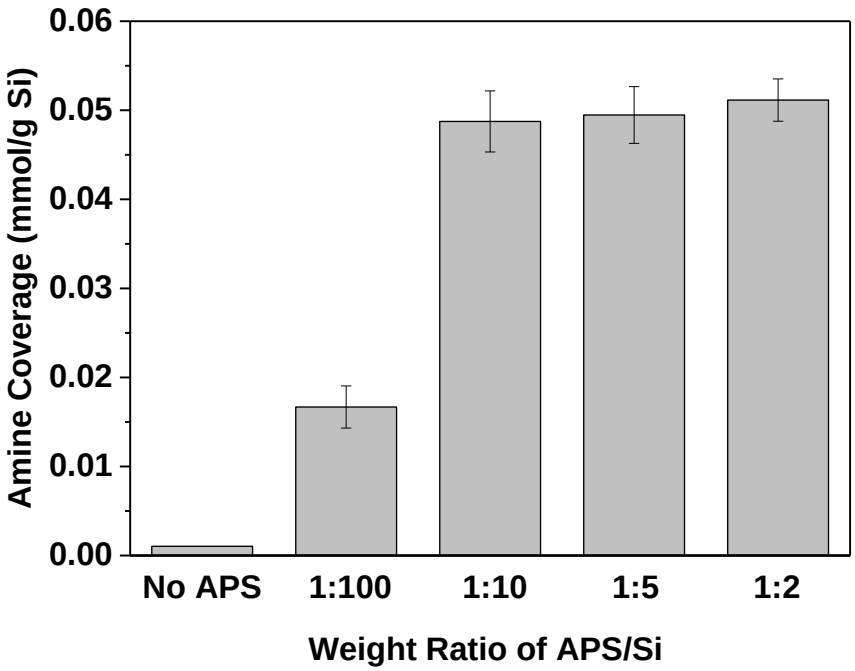


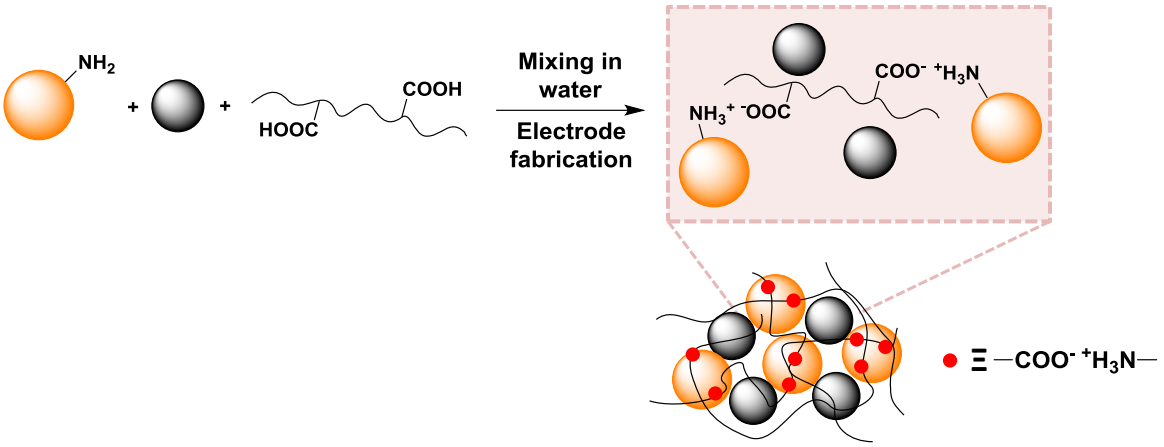
Figure 5.1. Effect of increasing the APS/Si weight ratio on the amino coverage of Si-NH_2 nanoparticles.

The amine functionalized Si (denoted as Si-NH_2), conductive filler particles (carbon black), and PAA were mixed in water and dried to form the electrode. During the mixing process, the

amine from Si-NH_2 deprotonated the carboxylic acid from the PAA polymer and formed the ionic ammonium carboxylate salt at the Si particle/PAA polymer binder interface (**Scheme 5.2**). The formation of ionic bonds was confirmed by XPS and Raman spectroscopy using amino functionalized silica (denoted as SiO_2-NH_2). Silica particles were used instead of Si-NH_2 to provide the transparency needed to detect the Raman signal of PAA. PAA signal could not be detected using Si-NH_2/PAA composite film due to the strong light scattering by Si particles.

Figure 5.2 compares the N1s core-level XPS spectra of SiO_2-NH_2 and SiO_2-NH_2/PAA composite film. Two characteristic peaks corresponding to free amine (-NH_2, 399.6 eV) and hydrogen bonded amine (401.8 eV) were observed in SiO_2-NH_2.[18] After blending with PAA, the free amine peak at 399.6 eV was greatly reduced. A new peak at 401.9 eV appeared which is attributed to protonated amine (ammonium, -NH_3^+), suggesting the formation of the cationic species of the ionic bonds.

The formation of the anionic species (carboxylate, -COO^-) was confirmed by Raman spectroscopy, as shown in **Figure 5.3**. The composition of particle/PAA (3:1 by weight) composite film was the same as Si anode. Characteristic Raman peaks of PAA (indicated by the black dashed lines) were observed at 1690 cm^{-1}, 1457 cm^{-1}, 850 cm^{-1}, that are attributed to C=O stretching, CH_2 deformation, and C-COOH stretching, respectively.[19] When PAA was partially neutralized (80 % degree of neutralization, **Figure 5.3**b), new peaks (indicated by the red dashed lines) appeared at 1710 cm^{-1}, 1417 cm^{-1}, 903 cm^{-1} (C=O stretching, CH_2 deformation, and C-COONa stretching, respectively) due to the formation of carboxylate.[20] These three new peaks were present in the spectrum of SiO_2-NH_2/PAA but not in the spectrum of SiO_2/PAA, confirming the existence of carboxylate in SiO_2-NH_2/PAA.



Scheme 5.2. Formation of interfacial ionic bonds between Si nanoparticles and PAA binder in Si composite anodes. The yellow spheres, black spheres, and polymer chains represent Si-NH_2, carbon black, and PAA binder, respectively.

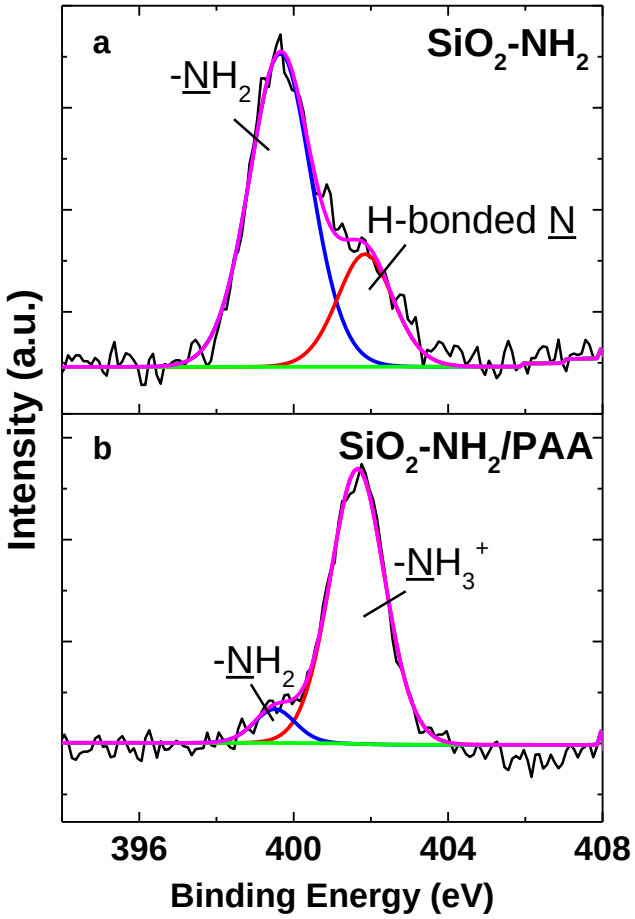


Figure 5.2. XPS core-level N 1s spectra of (a) SiO_2-NH_2 and (b) SiO_2-NH_2/PAA composite film.

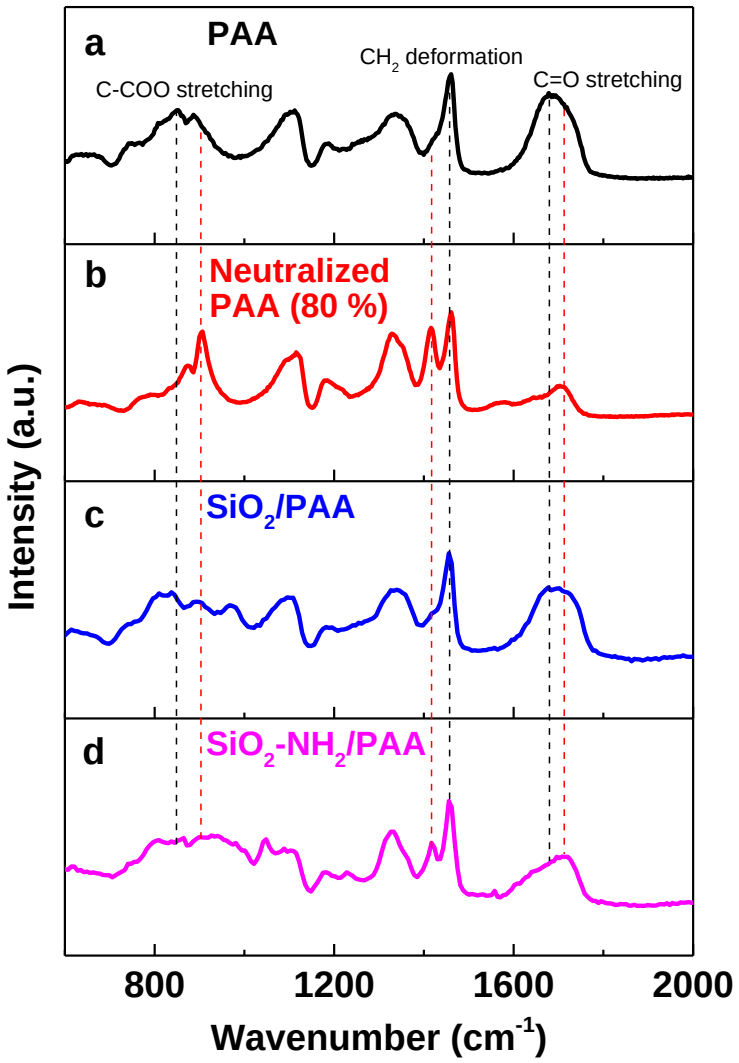


Figure 5.3. Raman spectra of (a) PAA film, (b) partially neutralized PAA (80 % degree of neutralization) film, (c) SiO_2/PAA composite film, and (d) SiO_2-NH_2/PAA composite film.

5.3.2 Cycling Performance of Si Composite Anodes

The Si composite anodes were assembled into coin cells with Li counter electrodes to evaluate their electrochemical properties. The anode composition was 60 wt% Si particles, 20 wt% polymer binder, and 20 wt% conductive filler particles for all the tests. Both PAA and CMC-Na binders were investigated. 10 wt% fluoroethylene carbonate (FEC) was used as additive in battery electrolyte (1 M $LiPF_6$ in ethylene carbonate/dimethyl carbonate, EC/DMC, 1:1 by volume) to promote the formation of stable SEI layer on Si particles.[21] The charge/discharge process was

performed between 1-0.01V vs. Li/Li^+. **Figure 5.4**a shows the voltage profile of different Si composite anodes during the initial charge/discharge cycle at a current density of 175 mAh/g. For all the anodes, lithiation and delithiation occurred at 0.1 V and 0.25 V, respectively, consistent with the previous reports for Si composite anodes.[22] The specific discharge capacity for all anodes ranged from 2300 to 2700 mAh/g. The initial columbic efficiency (ICE, charge capacity/discharge capacity ×100%) for Si anodes with ionic bonding (Si-NH_2/PAA) was 75 %. With CMC-Na and PAA binders, plain Si nanoparticles formed hydrogen bonding with the binders, and the ICE values were 76 % for CMC-Na containing anode and 70 % for PAA containing anode. The irreversible capacity loss from SEI formation (the decomposition of electrolyte on Si particle surfaces) primarily occurred in the first cycle. The methyl functionalized Si (denoted as Si-CH_3)/PAA anode was tested as a control. Due to the absence of ionic bonding or hydrogen bonding, the weak van der Waals interactions between Si-CH_3 and PAA resulted in vulnerable conductive network and significant SEI growth which lowered the ICE to 58 %.

The cycling stability and columbic efficiency of the Si composite anodes are summarized in **Figure 5.4**b. Anodes of conventional CMC-Na and PAA binders with no ionic bonding exhibited a significant capacity decrease of ca. 65 % after 400 cycles. For the Si-CH_3/PAA control anode, an even faster capacity fade of ca. 95 % was presented due to the weak bonding of Si-CH_3 with PAA binder. In contrast, the Si-NH_2/PAA anode with ionic bonding exhibited excellent cycling stability. The discharge capacity after 400 cycles remained 1177 mAh/g, which corresponds to 80 % capacity retention. These results suggest that the ionic bonding is more effective than hydrogen bonding in preserving the integrity of conductive network and repairing the damage in conductive network caused by the volume change during anode cycling.

An increase of capacity was consistently observed for many anodes during the initial (0-50) cycles (**Figure 5.4**b). Though similar results have been reported previously, the origin of this increase is not well understood.[23, 24] The increased capacity is likely due to the slow wetting of the electrolyte into the composite anodes during anode cycling.

To further explore the effect of ionic bonding to the cycling performance of Si anodes, we tested Si anodes with different concentrations of ionic bonding. The XPS characterization revealed that all the amino groups were converted to ammonium ions in the composite anode. Hence, the concentration of ionic bonding in the anodes was controlled by the amine coverage on Si particle surface. **Figure 5.5** shows the relation of cycling stability of Si anodes with different amine coverages on Si particles. Initially, all of the anodes showed similar capacity ranging from 2394 mAh/g to 2609 mAh/g. The capacity retention after 100 cycles, however, started to differ. Significant improvement on anode capacity retention was observed when the amine coverage increased from 0.016 mmol/g Si to 0.050 mmol/g. The increased capacity retention of Si anodes is clearly correlated with the increase of amine coverage on Si particles and the increase of ionic bonding concentration in the Si anodes.

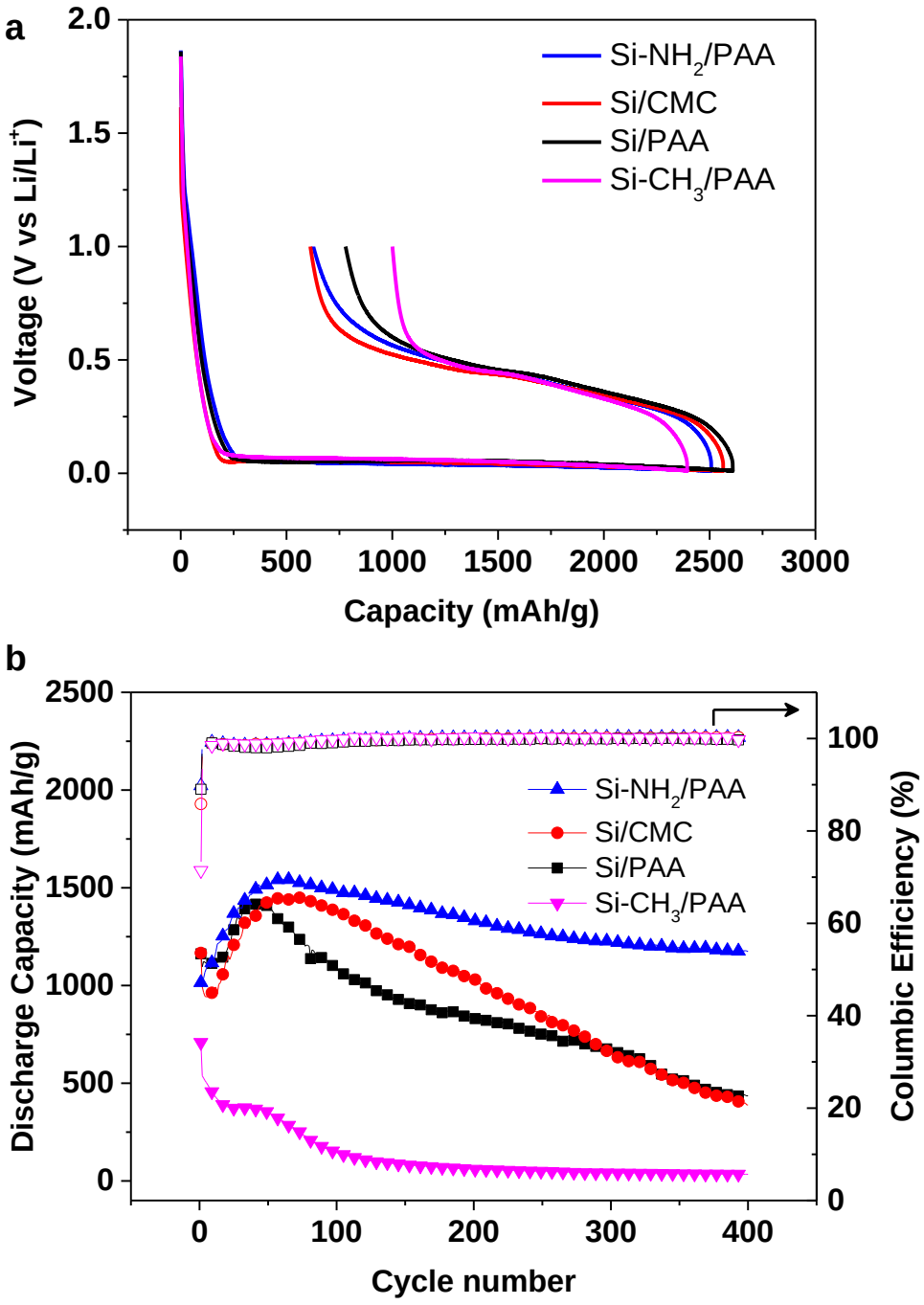


Figure 5.4. Cycling performance of Si composite electrodes. (a) Initial voltage-capacity profile of Si composite anodes at a current density of 175 mA/g between 0.01 and 1.0 V vs Li/Li^+. (b) Discharge capacity (solid symbols) and columbic efficiency (open symbols) of Si composite anodes at a current density of 2.1 A/g between 0.01 and 1.0 V vs Li/Li^+. The anodes were pre-cycled at a current density of 175 mA/g (results were not shown) for 1 cycle. All cycling experiments used 1 M $LiPF_6$ EC/DMC (1:1 by volume) electrolyte with 10 wt% FEC additive. The capacity was normalized by the weight of Si particles.

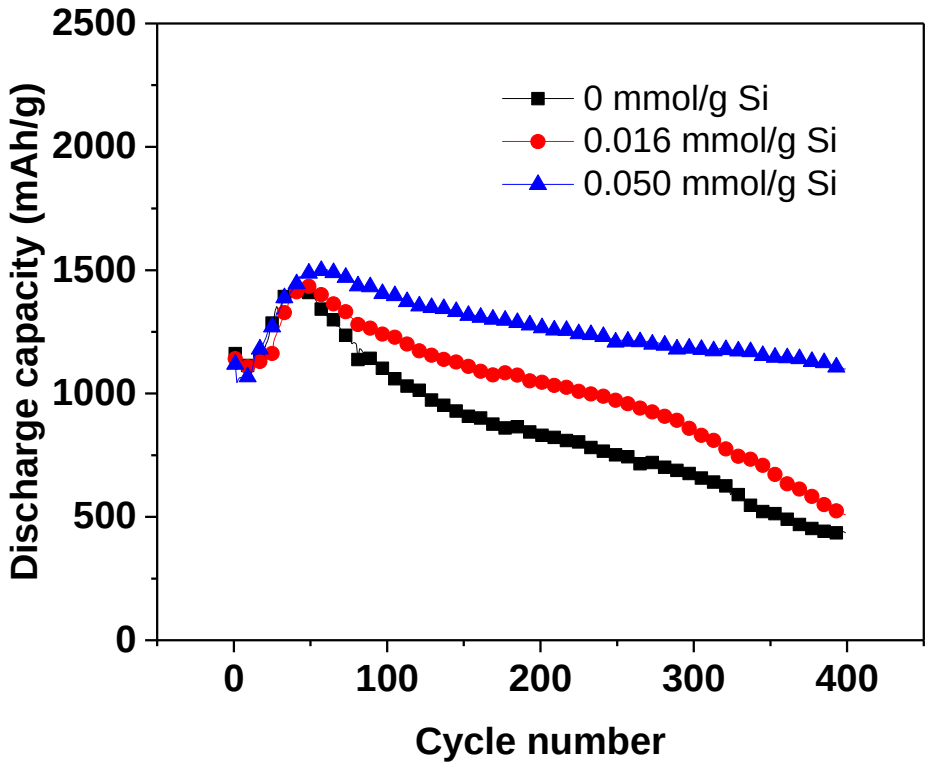


Figure 5.5. Electrochemical cycling performance of Si composite anodes with different amine coverages on Si particles. The anodes were cycled at a current density of 2.1 A/g between 0.01 and 1.0 V vs Li/Li^+. The anodes were pre-cycled at a current density of 175 mA/g (results were not shown) for 1 cycle. The capacity was normalized by the weight of Si particles.

The capacity of Si anodes with ionic bonding was also evaluated at different cycling rates. **Figure 5.6** shows the capacity change and columbic efficiency with respect to different cycling rates. The current density increased from 0.21 A/g (C/20) to 4.2 A/g (1C) with 5 different cycling rates, and then moved back to 0.21 A/g. After the initial 10 cycles at 0.21 A/g, the reversible capacity remained above 2000 mAh/g. The initial gradual increase of capacity is consistent with the cycling results in **Figure 5.4**b and **Figure 5.5**. As expected, a decrease of capacity was observed with increasing current density.[25] At the highest current density of 4.2 A/g, the anode still retained a high capacity of ~ 1150 mAh/g. When the current density was brought back to 0.21

A/g, the capacity was fully recovered to ca. 2100 mAh/g, suggesting no damage of anode structure during the entire cycling test.

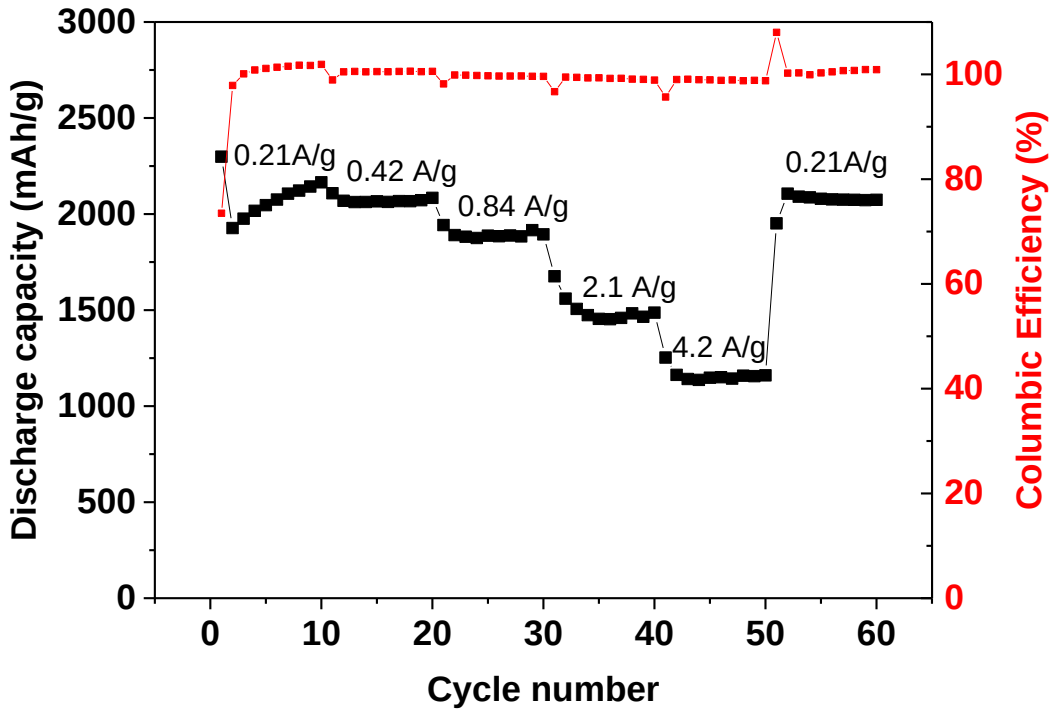


Figure 5.6. Discharge capacity and columbic efficiency of Si-NH_2/PAA composite anode at various current densities between 0.01 and 1.0 V vs Li/Li^+. The capacity was normalized by the weight of Si particles.

The resistance change of the Si composite anodes with ionic bonding was characterized by Electrochemical Impedance Spectroscopy (EIS). The measurements were performed at the fully delithiated state of the anodes by holding the voltage at 1 V vs. Li/Li^+ for 6 h after the charging process at different cycle numbers. The Nyquist plots of the Si-NH_2/PAA anodes are shown in **Figure 5.7**. The response resembles a semicircle in the high-frequency range followed by a line in the low-frequency range within each plot. The diameter of the semicircle represents the charge transfer resistance of the cell. In the first 10 cycles, the charge transfer resistance decreased possibly due to the slow wetting of electrolyte into the anode structure and increase of Si particle conductivity after Li^+ doping.[23] After the initial 10 cycles, the charge transfer resistance remained

the same throughout the remainder of the test, indicating the anode maintained a robust conductive network with stable SEI layer. Moreover, the stable resistance over 300 cycles also explained the superior capacity retention (**Figure 5.4**b) of the Si anodes.

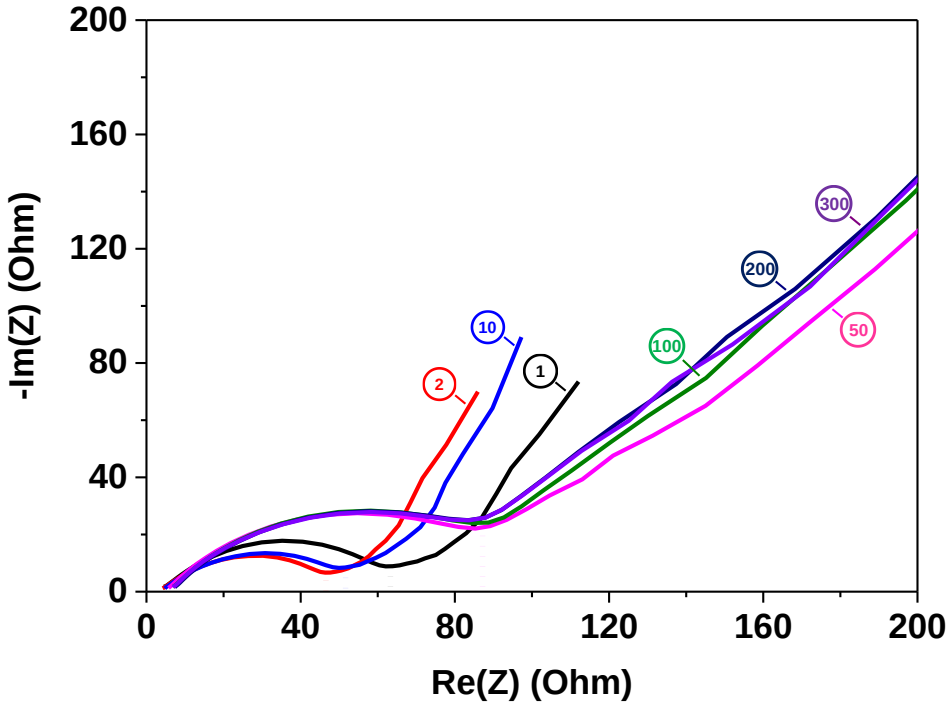


Figure 5.7. Impedance test of Si-NH_2/PAA composite anode. The anode was cycled at a current density of 2.1 Ah/g between 0.01 and 1.0 V vs Li/Li^+. The circled number refers to the cycle number of galvanostatic cycling and impedance was measured after completion of the entire discharge/charge cycle.

5.3.3 Structural Change of Si Composite Anodes

The morphology change of Si-NH_2/PAA anodes upon cycling was characterized using SEM, as shown in **Figure 5.8** (cross-sectional images). Prior to cycling, discrete Si particles and carbon black particles were observed in the composite anode with uniform distribution. Upon cycling, the anode surface became smooth due to the formation of SEI layer on both Si and carbon black particle surface.

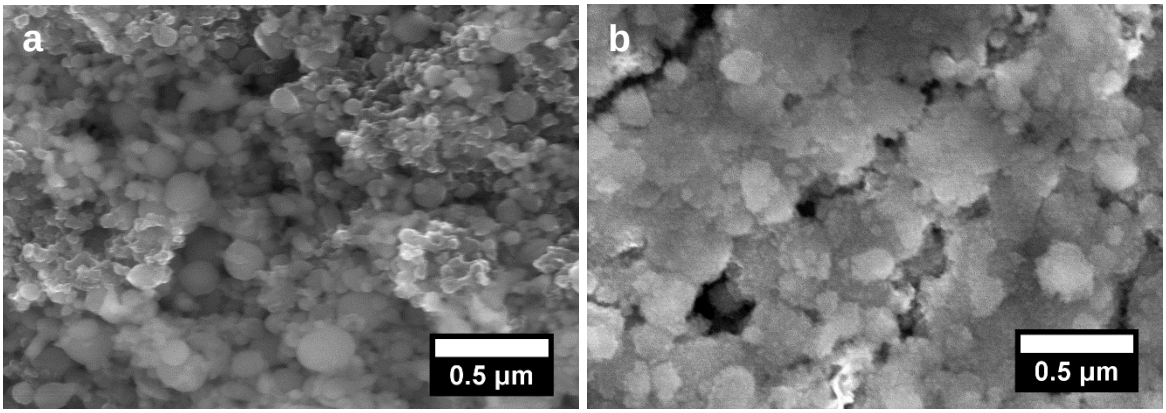


Figure 5.8. Cross-sectional SEM images of Si-NH_2/PAA composite anode before and after cycling. The anode was cycled at a current density of 2.1 Ah/g between 0.01 and 1.0 V vs Li/Li^+ for 400 cycles.

The composition of the SEI layer was further studied by XPS and the results are summarized in **Figure 5.9**. The N1s core-level XPS spectra of pristine and cycled anodes are shown in **Figure 5.9**a. The formation of ionic bonds was confirmed by the presence of protonated amine ($-NH_3^+$) in pristine anode. After 400 cycles, no N1s signal was detected, suggesting the formation of SEI layer on the Si particle surface. Similarly, in **Figure 5.9**c, the C1s signals from carbon black and PAA disappeared after cycling, further demonstrating the formation of SEI layers on carbon black surface and on PAA binder. Hence, we propose that the formation of SEI does not interfere with the ionic bonds at the Si-NH_2/PAA interfaces.

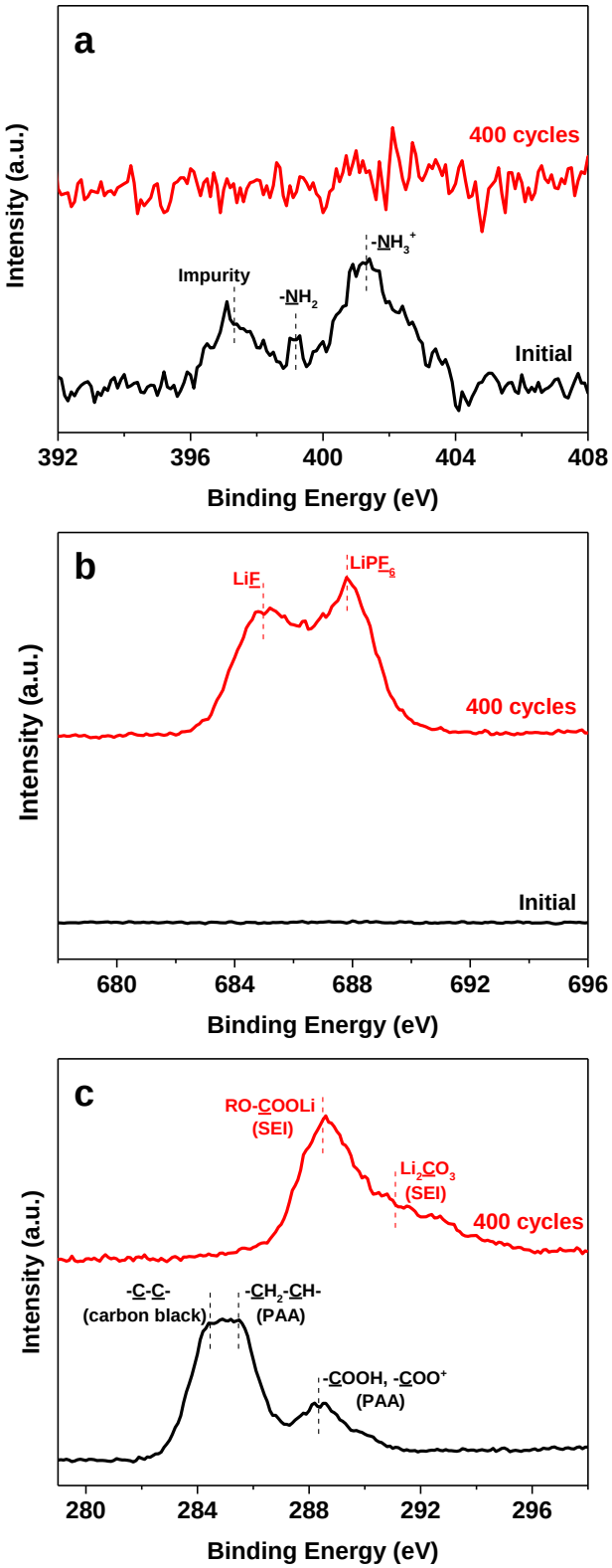


Figure 5.9. XPS spectra of Si anode surface before (black curves) and after 400 cycles (red curves). (a) N1s; (b) F1s; (c) C1s. The anode was cycled at a current density of 2.1 Ah/g between 0.01 and 1.0 V vs Li/Li^+.

5.4 Conclusions

A novel dynamic bonding approach was developed to increase the cycle lifetimes and reliability of Si composite anodes through the restoration of the electrical interfaces. Si composite anodes with increased capacity retention were achieved through dynamic ionic bonding at the interface between Si nanoparticles and the polymeric binder. Amine groups were covalently attached to Si nanoparticle surface. During anode fabrication, the ionic bonds were readily formed between the amine groups on Si particle surfaces and the carboxyl groups on poly(acrylic acid) binder, as confirmed by X-ray photoelectron and Raman spectroscopy. The dynamic ionic bonds effectively mitigated the large volume change of Si anodes during lithium intercalation. We achieved Si composite anodes with a cycle life of 400 cycles and 80 % capacity retention at a current density of 2.1 mA/g (C/2). The Si composite anodes with ionic bonding also demonstrated good rate capability with a high capacity of 1150 mAh/g at 4.2 mA/g (1C).

5.5 References

[1] M. Armand, J. M. Tarascon, *Nature*, **2008**, *451*, 652.

[2] J. M. Tarascon, M. Armand, *Nature*, **2001**, *414*, 359.

[3] H. Wu, Y. Cui, *Nano Today*, **2012**, *7*, 414.

[4] U. Kasavajjula, C. Wang, A. J. Appleby, *Journal of Power Sources*, **2007**, *163*, 1003.

[5] I. Kovalenko, B. Zdyrko, A. Magasinski, B. Hertzberg, Z. Milicev, R. Burtovyy, I. Luzinov, G. Yushin, *Science*, **2011**, *334*, 75.

[6] J. Li, R. B. Lewis, J. R. Dahn, *Electrochemical and Solid-State Letters*, **2007**, *10*, A17.

[7] Z. J. Han, N. Yabuuchi, K. Shimomura, M. Murase, H. Yui, S. Komaba, *Energy & Environmental Science*, **2012**, *5*, 9014.

[8] J. S. Bridel, T. Azaïs, M. Morcrette, J. M. Tarascon, D. Larcher, *Chemistry of Materials*, **2009**, *22*, 1229.

[9] C. Wang, H. Wu, Z. Chen, M. T. McDowell, Y. Cui, Z. Bao, *Nature Chemistry*, **2013**, *5*, 1042.

[10] R. J. Wojtecki, M. A. Meador, S. J. Rowan, *Nature Materials*, **2011**, *10*, 14.

[11] J. Y. Sun, X. Zhao, W. R. K. Illeperuma, O. Chaudhuri, K. H. Oh, D. J. Mooney, J. J. Vlassak, Z. Suo, *Nature*, **2012**, *489*, 133.

[12] Z. Wei, J. He, T. Liang, H. Oh, J. Athas, Z. Tong, C. Wang, Z. Nie, *Polymer Chemistry*, **2013**, *4*, 4601.

[13] D. V. Andreeva, D. Fix, H. Möhwald, D. G. Shchukin, *Advanced Materials*, **2008**, *20*, 2789.

[14] A. B. South, L. A. Lyon, *Angewandte Chemie International Edition*, **2010**, *49*, 767.

[15] E. Soto-Cantu, R. Cueto, J. Koch, P. S. Russo, *Langmuir*, **2012**, *28*, 5562.

[16] T. Bayer, K. J. Eichhorn, K. Grundke, H. J. Jacobasch, *Macromolecular Chemistry and Physics*, **1999**, *200*, 852.

[17] X. Song, J. Zhai, Y. Wang, L. Jiang, *Journal of Colloid and Interface Science*, **2006**, *298*, 267.

[18] B. Lindberg, R. Maripuu, K. Siegbahn, R. Larsson, C. G. Gölander, J. C. Eriksson, *Journal of Colloid and Interface Science*, **1983**, *95*, 308.

[19] J. Dong, Y. Ozaki, K. Nakashima, *Journal of Polymer Science Part B: Polymer Physics*, **1997**, *35*, 507.

[20] S. Koda, H. Nomura, M. Nagasawa, *Biophysical Chemistry*, **1983**, *18*, 361.

[21] J. Song, M. Zhou, R. Yi, T. Xu, M. L. Gordin, D. Tang, Z. Yu, M. Regula, D. Wang, *Advanced Functional Materials*, **2014**, *24*, 5904.

[22] B. Koo, H. Kim, Y. Cho, K. T. Lee, N. S. Choi, J. Cho, *Angewandte Chemie International Edition*, **2012**, *51*, 8762.

[23] H. Wu, G. Yu, L. Pan, N. Liu, M. T. McDowell, Z. Bao, Y. Cui, *Nature Communications*, **2013**, *4*.

[24] M. H. Ryou, J. Kim, I. Lee, S. Kim, Y. K. Jeong, S. Hong, J. H. Ryu, T. S. Kim, J. K. Park, H. Lee, J. W. Choi, *Advanced Materials*, **2013**, *25*, 1571.

[25] C. K. Chan, H. Peng, G. Liu, K. McIlwrath, X. F. Zhang, R. A. Huggins, Y. Cui, *Nature Nanotechnology*, **2008**, *3*, 31.

CHAPTER 6

SUMMARY AND FUTURE WORK

6.1 Summary

Restoration of electrical conductivity upon damage was demonstrated in a simple electrical circuit and composite battery anode via two distinct approaches. The first approach relied on the incorporation of microcapsules containing conductive particle suspensions into a circuit or electrode. In the second approach, dynamic ionic bonds were created at the interface of polymer binder and Si nanoparticles in a composite electrode.

Microcapsules were prepared with carbon black suspensions high in solid loading (up to 0.2 g/mL). Oxidized carbon black was rendered more hydrophobic through surface functionalization with octadecylamine to covalently bond octadecyl chains on carbon black surfaces. Functionalization significantly improved dispersability and suspension stability of carbon black in hydrophobic solvents such as *o*-DCB. Upon crushing, microcapsules containing FCB suspensions exhibited significant particle release relative to microcapsules filled with unfunctionalized regular carbon black. Release of FCB particles was further enhanced by the addition of two types of core thickeners, epoxy resin or P3HT in the capsule liquid core.

Two experimental protocols were developed to examine the e*x situ* conductivity restoration of composite battery electrodes and a simple electric circuit using FCB filled microcapsules. Consistent line cracks (ca. 10 μm in width) were introduced to Si anodes by pulling out an embedded glass fiber. The deposition and rupture of FCB microcapsules on the cracked region led to a full recovery of the anode conductivity. Similarly, a four-point bend test specimen was optimized to introduce a crack (ca. 3 μm in width) on Au film which was sandwiched into a multi-

layered structure. Upon the release of FCB particles onto the crack region, partial conductivity restoration of the Au film was achieved.

A PDA coating was applied to the microcapsule surfaces to increase capsule stability in the battery environment. The dense and uniform PDA barrier layer effectively limited the diffusion of liquid core through capsule shell wall to the electrolyte and protected the microcapsules from solvent and thermal damage. The PDA coated capsules showed superior thermal stability at elevated temperature (180 ^{o}C) and minimal core loss in battery electrolyte, demonstrating strong potential for *in-situ* restoration of conductivity in batteries.

Intrinsic restoration of the battery electrode was achieved by incorporating dynamic ionic bonding at the particle/binder interface in Si composite anodes. Si nanoparticles were successfully functionalized with amino groups. A network of Si particles with interfacial ionic bonds was achieved by combining the particles with a PAA binder. The formation of ionic bonds between amino groups on Si particles and carboxylic acid groups on PAA binders was characterized by XPS and Raman spectroscopy. During cycling, the damage of particle/binder interface caused by anode volume change led to the dissociation of the ionic bonds. As the bonds are reversible, immediate healing occurred at the interface due to the reformation of the ionic bonds. The self-healing Si composite anodes demonstrated long term cycling stability and good rate capability. Dynamic bonds can be incorporated in other types of battery electrodes to improve the cycling performance.

6.2 Future Work

6.2.1 In-situ Self-healing Battery Electrodes using FCB Microcapsules

In this dissertation, *ex-situ* conductivity restoration of Si anodes and electric circuits was achieved using carbon black filled microcapsules (Chapter 3). The next task is to extend this strategy to *in-situ* conductivity restoration of Si composite anodes in the battery environment. During cycling, the volume change of Si anodes results in the loss of electrical pathways and generates isolated Si particles. When the microcapsules are present in the composite anode, the large volume change can potentially trigger the rupture of microcapsules and release of conductive carbon black particles to the damaged electrical interfaces, restoring the electrical pathways of the isolated Si particles and recovering the anode capacity. The self-healing mechanism is illustrated in **Figure 6.1**.

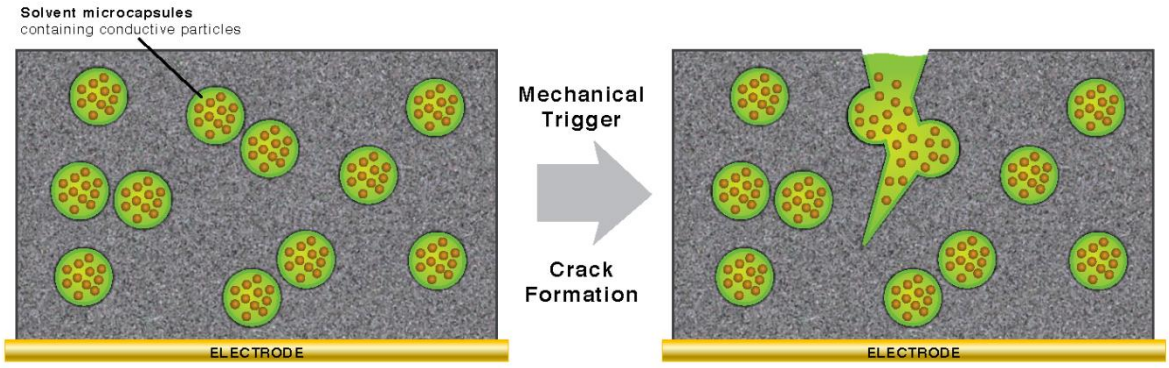


Figure 6.1. Schematic illustration of conductivity restoration of Si composite anode via the release of carbon black particles from ruptured microcapsules.

In-situ restoration of conductivity is much more complicated in the battery environment. Two key challenges need to be addressed in order to achieve *in-situ* electrode healing. First, the capsules must remain stable in the battery and only triggered rupture by the localized damage of Si anodes during cycling. As the first step, capsules can be embedded into composite anodes by mixing the capsules into a slurry of active particles, binder, and carbon black followed by casting

onto Cu foil and air drying. Capsule survivability could be examined using the ^{1}H-NMR method (described in Chapter 4) to provide quantitative information of liquid core release to electrolyte. The capsule shape and morphology can also be monitored by SEM (and/or optical microscopy).

The second challenge requires sufficient delivery of carbon black suspensions to the damage region of the anode in the presence of electrolyte. In capsule based self-healing polymers and composites, the flow of liquid healing agent is dominated by the capillary forces in the crack zone. When the capsules are ruptured in a solvent environment where the solvent is compatible with the core liquid, transport of the core liquid is less predictable. Since the battery electrolyte (EC/DMC mixture) is miscible with the capsule liquid core *o*-DCB, the released FCB particles in *o*-DCB can potentially go into the solution of electrolyte rather than being delivered to the damaged region of Si anodes. When designing the capsule core, P3HT is not only used as core thickener to stabilize FCB particles in the suspensions but also considered as polymer binder for FCB particles. We hypothesize that P3HT can precipitate in battery electrolyte and trap the FCB particles in the damaged region. Other types of electrolyte insoluble polymers could also be studied as alternative additives in capsule core to optimize the FCB release and healing performance. Once capsules are incorporated in the battery electrode, EIS can be used to test the impedance change of Si anodes. This test provides the most straightforward evidence of conductivity restoration.

6.2.2 Self-healing Battery Electrodes Based on Dynamic Chemical Bonding

Beyond ionic bonding, the wide variety of dynamic chemical bonds, such as hydrogen bonding, metal-ligand complex, and π-π stacking, allows further developments of self-healing battery electrodes, not only limited to Si anodes. With careful design of the synthetic routes, various dynamic bonds can be incorporated into electrode structure by functionalizing the active particles and polymer binders with dynamic bonding moieties. **Figure 6.2** shows an example of

hydrogen bonding based Si composite anode with quadruple hydrogen bonding array covalently incorporated into the anode structure (including the synthesis routes).

Among all types of hydrogen bonds, the quadruple hydrogen bond array formed by the dimerization of 2-ureido-4[1H]-pyrimidinones (UPy) has high binding strength and can greatly enhance the mechanical properties of solid-state polymer when attached to the polymer chain and is widely used in supramolecular polymers.[1] The large association constant of UPy dimers makes self-healing possible.[2, 3] UPy can be covalently bonded to the polymer binder (i.e. CMC) and Si particle surface separately. Upon mixing in water, quadruple hydrogen bonding array should be formed at the particle/binder interface.

In preliminary studies, UPy containing carbonyldiimidazole was synthesized as the first step to achieve UPy containing amine (UPy-NH_2). A mixture of methylisocytosine (2.0 g) and carbodiimidazole (4.14 g) in dried DMSO (20 mL) was heated and stirred at 100 ^oC under an argon atmosphere for 2 h. The resulting solid was filtered and washed with dry hexane to obtain UPy-carbonyldiimidazole. Then the UPy-carbonyldiimidazole (0.9 g) was mixed with hexyethylene diamine (0.54 g) in tetrahydrofuran (THF, 15 mL) and let the reaction proceed at room temperature under an argon atmosphere for 72 h. The UPy-NH_2 product precipitated out from the THF solution and was collected by filter drying and rinsed with ethanol.

An UPy containing CMC binder (UPy-CMC) was synthesized by dissolving CMC (0.1) g and appropriate amount of UPy-NH_2 and 4-(4,6-dimethoxy-1,3,5-triazin-2-yl)-4-methylmorpholinium chloride (DMTMM) in deionized water (10 mL). The NH_2 group from UPy-NH_2 formed amide bond with the COONa group from CMC with the assistance of DMTMM. After reacting at room temperature for 48 h, the final solution was dialyzed for 7 days to remove the residual DMTMM and byproduct. Freeze drying was used to obtain solid UPy-CMC.

UPy containing Si (UPy-Si) was synthesized via a two step process. Methylisocytosine (0.300 g) and 3-(triethoxysilyl)propyl isocyanate (0.594 g) were dissolved in DMSO (10 mL) and heated to 100 ^{o}C for 8 h under argon atmosphere to obtain UPy containing silane (UPy-silane). Then appropriate amount of UPy-silane/DMSO solution was added to Si particle (1.0 g) suspension in toluene (40 mL). After 48 h at room temperature, the solid was separated by centrifuging and rinsed with ethanol 3 times to obtain UPy-Si.

The preliminary UPy-CMC and UPy-Si were characterized by FT-IR, as summarized in **Figure 6.3**. Different amounts of UPy were covalently attached to CMC (**Figure 6.3**a). The number in the legend refers to the percent of COONa in CMC that reacts with UPy-NH_2 to form amide linkage. Characteristic peaks of UPy groups were observed at 1698 cm^{-1}, 1662 cm^{-1}, 1577 cm^{-1}, and 1519 cm^{-1}.[4] The UPy peak intensity increased by increasing the percent of UPy that was incorporated into the CMC backbone. Similarly, UPy-Si also showed the characteristic peaks of UPy, confirming the successful functionalization of Si with UPy groups.

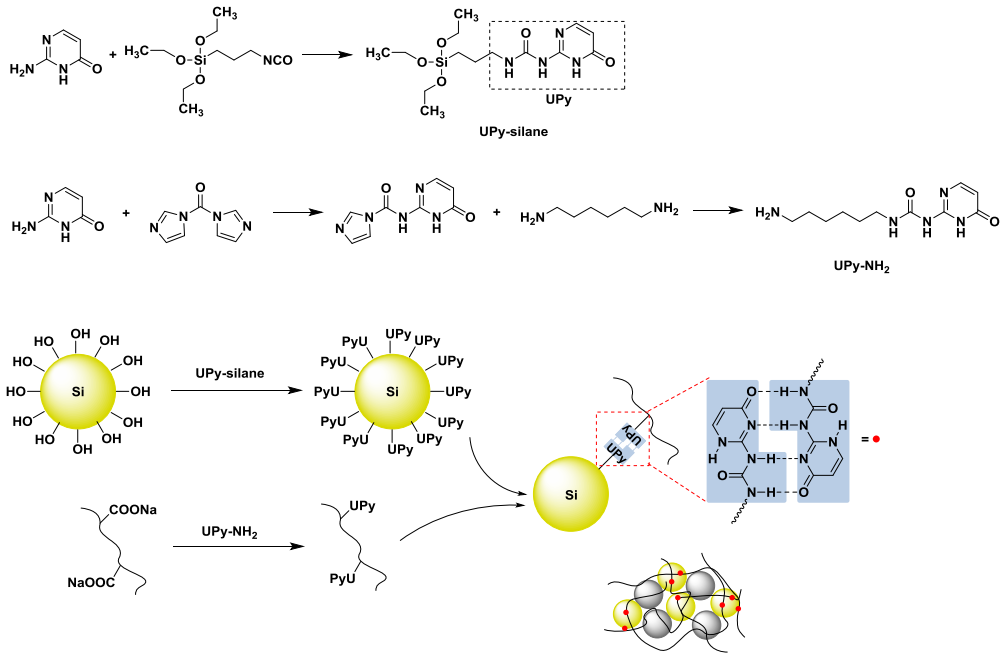


Figure 6.2. The synthetic routes for Upy-silane and Upy-NH_2, and the components of Si composite anodes with quadruple hydrogen bonding array.

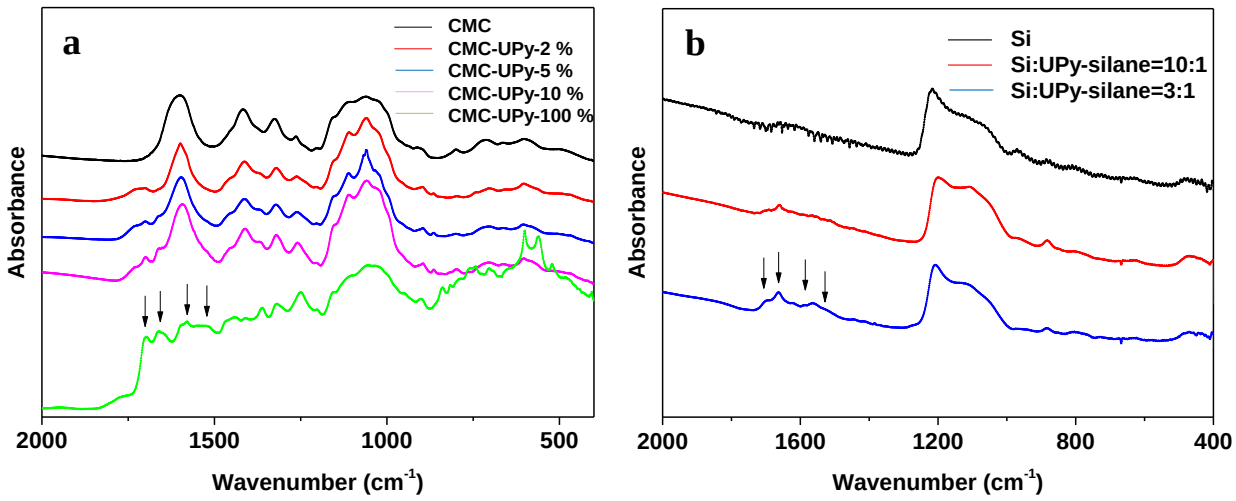


Figure 6.3. FTIR spectra of UPy-CMC (a) and UPy-Si (b).

Following the procedure described in Chapter 5, the UPy-CMC and UPy-Si were fabricated into Si composite anodes and assembled into coin cells with Li counter electrodes to evaluate their electrochemical properties. The electrolyte was 1 M $LiClO_4$ in EC/DMC (1:3 by volume). The charge/discharge process was performed at a current density of 0.42 mA/g between 2-0.005 V vs. Li/Li^+. **Figure 6.4** shows the cycling stability of Si composite anodes with different UPy contents in the CMC binder. Unfortunately, the cycling performance was not improved by the incorporation of quadruple hydrogen bonding array.

Two mechanisms are proposed for the inferior cycling stability of Si anodes with UPy moieties. The first one is related to the chain conformation of the UPy-CMC binder in electrode slurry, where water serves as the dispersant in this study. An extended polymer chain conformation is favorable to the formation of efficient bridging to Si and carbon black particles during electrode fabrication.[5] However, the UPy groups in CMC binder tend to form intramolecular hydrogen bonding and lead to coil conformation of the polymer chain. As a result, the number of binding sites between CMC binder and Si particles is greatly reduced. Second, as

the quadruple hydrogen bond is self-complementary and is much stronger than single hydrogen bond, it is rather difficult to break the UPy dimers within UPy-CMC binder and form new hydrogen bonds between UPy-CMC and UPy-Si. The combined effect may lead to the insufficient binding between Si particles and CMC binder and poor capacity retention of the anodes. In future, quadruple hydrogen bonding with hetero-complementary structure[6] could be used in Si composite anodes to eliminate the inter- and intramolecular UPy dimerization within UPy-CMC polymer chains.

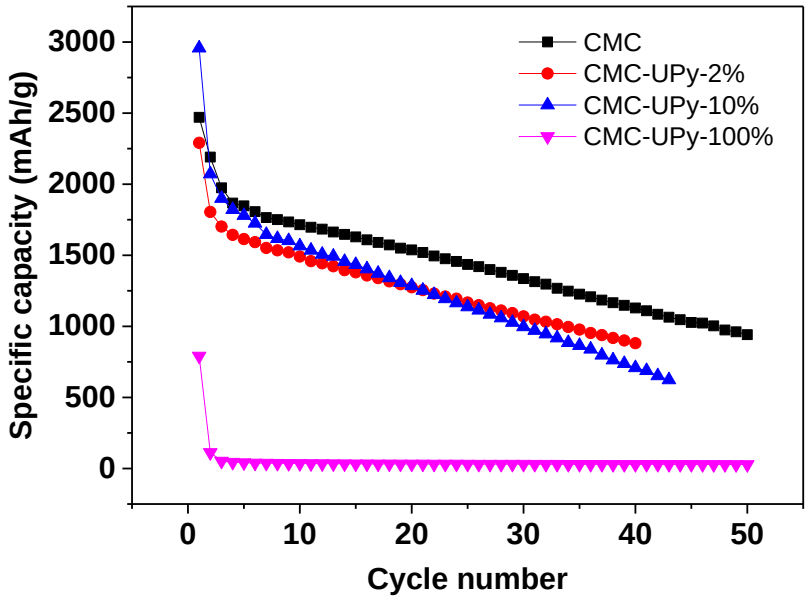


Figure 6.4. Electrochemical cycling performance of Si composite anodes at a current density of 0.42 A/g between 0.01 and 1.0 V vs Li/Li^+. The electrode composition was 60 wt% Si particles, 20 wt% binder, and 20 wt% conductive filler particles. All cycling experiments used 1 M $LiClO_4$ EC/DMC (1:3 by volume) electrolyte. The discharge capacity was normalized by the weight of Si particles.

Other than the quadruple hydrogen bonding strategy, many classes of dynamic bonding (**Figure 6.5**) could be incorporated into battery electrodes for self-healing application.

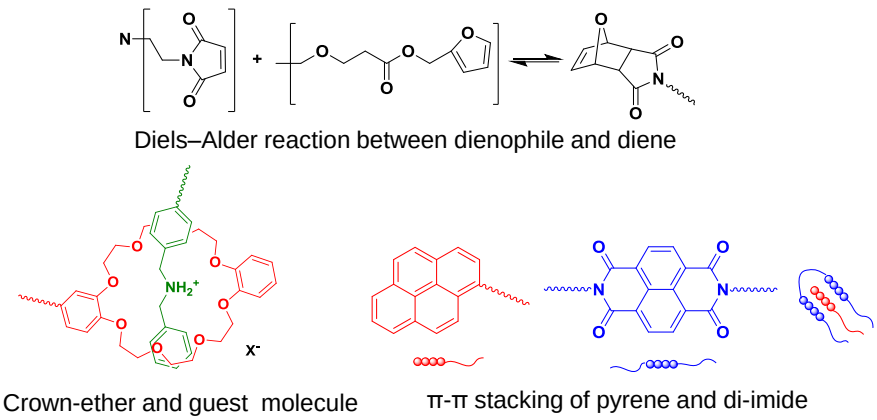


Figure 6.5. Examples of various covalent and non-covalent dynamic bonds.

The destruction of conductive pathways is one cause of capacity fade for Si composite anodes. Another contributing factor is the deterioration of the anode/current collector interface that ultimately results in debonding of anode from current collector.[7] Early on, research focused on increasing the adhesion of Si thin film anodes by increasing the surface roughness of Cu current collector.[8, 9] Recently, Ryou et al. addressed this problem by incorporating adhesive catechol functional groups into PAA binders in Si composite anodes to enhance the adhesion of anode to Cu current collector and demonstrated improved capacity and cycling stability.[10] Inspired by the self-healing of Si composite anodes using dynamic ionic bonding, we can envision incorporating dynamic bonding at the interface of electrode and current collector (**Figure 6.6**) to help preserve the bonding between the anode and current collector and maintain stable capacity of the electrode during cycling.

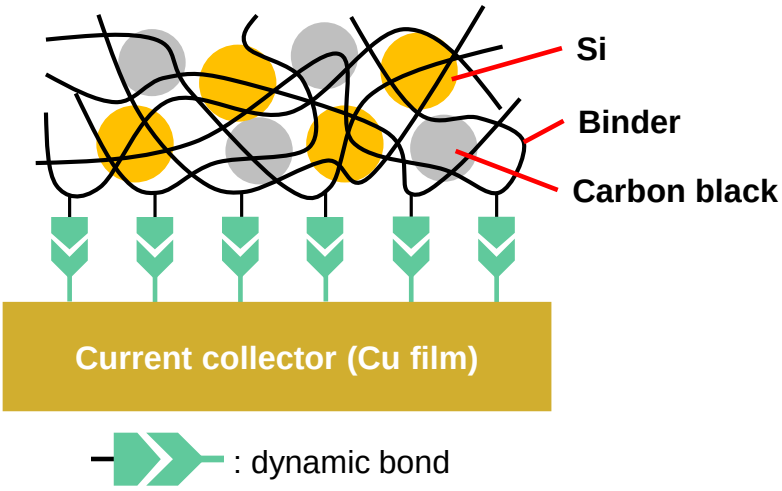


Figure 6.6. Schematic illustration of battery composite electrode bonded to current collector via dynamic bonding.

6.3 References

[1] R. J. Wojtecki, M. A. Meador, S. J. Rowan, *Nature Materials*, **2011**, *10*, 14.

[2] F. H. Beijer, R. P. Sijbesma, H. Kooijman, A. L. Spek, E. W. Meijer, *Journal of the American Chemical Society*, **1998**, *120*, 6761.

[3] S. H. M. Söntjens, R. P. Sijbesma, M. H. P. van Genderen, E. W. Meijer, *Journal of the American Chemical Society*, **2000**, *122*, 7487.

[4] P. Y. W. Dankers, E. N. M. van Leeuwen, G. M. L. van Gemert, A. J. H. Spiering, M. C. Harmsen, L. A. Brouwer, H. M. Janssen, A. W. Bosman, M. J. A. van Luyn, E. W. Meijer, *Biomaterials*, **2006**, *27*, 5490.

[5] B. Lestriez, S. Bahri, I. Sandu, L. Roué, D. Guyomard, *Electrochemistry Communications*, **2007**, *9*, 2801.

[6] C. A. Anderson, A. R. Jones, E. M. Briggs, E. J. Novitsky, D. W. Kuykendall, N. R. Sottos, S. C. Zimmerman, *Journal of the American Chemical Society*, **2013**, *135*, 7288.

[7] Z. J. Han, N. Yabuuchi, K. Shimomura, M. Murase, H. Yui, S. Komaba, *Energy & Environmental Science*, **2012**, *5*, 9014.

[8] K. L. Lee, J. Y. Jung, S. W. Lee, H. S. Moon, J. W. Park, *Journal of Power Sources*, **2004**, *129*, 270.

[9] M. Uehara, J. Suzuki, K. Tamura, K. Sekine, T. Takamura, *Journal of Power Sources*, **2005**, *146*, 441.

[10] M. H. Ryou, J. Kim, I. Lee, S. Kim, Y. K. Jeong, S. Hong, J. H. Ryu, T. S. Kim, J. K. Park, H. Lee, J. W. Choi, *Advanced Materials*, **2013**, *25*, 1571.